INTERACTION AND PASSAGE OF SUPERPARAMAGNETIC IRON OXIDE NANOPARTICLES IN AN *in vitro* BLOOD-BRAIN BARRIER MODEL

Dissertation
zur Erlangung des akademischen Grades

doctor rerum naturalium (Dr. rer. nat.)

vorgelegt dem Rat der Medizinischen Fakultät der
Friedrich-Schiller-Universität Jena

von M.Sc. Christine Gräfe, geb. Gey
geboren am 03.11.1987 in Reichenbach im Vogtland

Gutachter

1. Prof. Dr. Andreas Hochhaus (Universitätsklinikum Jena, Jena)
2. Prof. Dr. Ferdinand von Eggeling (Universitätsklinikum Jena, Jena)
3. Prof. Ph.D. Urs Häfeli (University of British Columbia, Vancouver)

Tag der öffentlichen Verteidigung: 18. Dezember 2018

»Das Schönste, was wir entdecken können, ist das Geheimnisvolle. «

Albert Einstein (1879-1955)

Contents

Nomenclature **IX**

List of Figures **XI**

List of Tables **XIII**

Abstract **1**

Zusammenfassung **2**

1 Introduction **3**

1.1 Nanomedicine 5
  1.1.1 Superparamagnetic Iron Oxide Nanoparticles 7
  1.1.2 Uptake Mechanisms for Nanoparticles 9
  1.1.3 Biologic and Cytotoxic Effects of Nanoparticles 11
  1.1.4 Biodegradation and Excretion of Nanoparticles 13
  1.1.5 Protein Corona 14
1.2 Blood-Brain Barrier 16
  1.2.1 General Structure 16
  1.2.2 Ways across the Blood-Brain Barrier 18
  1.2.3 Model Systems Representing the Blood-Brain Barrier . . . 21
1.3 Aims of the Study 23

2 Methods and Materials **25**

2.1 SPION- and Protein Corona Characterization 25
  2.1.1 SDS-PAGE and Silver Staining 26
  2.1.2 Physical SPION Characterization 27
2.2 Cell Culture 27
  2.2.1 Cell Lines 27
  2.2.2 Cell Cultivation 28

2.2.3 Transwell-Based Generation of *in vitro* Blood-Brain Barrier Model . . . 28
2.2.4 Preparation of Astrocyte-Conditioned Medium . . . 29
2.2.5 Differentiation of Progenitor Cells . . . 29
2.3 Cell Viability Assays . . . 30
2.3.1 PrestoBlue™ Assay . . . 30
2.3.2 SYTOX® Red Dead Cell Staining . . . 31
2.3.3 Real-Time Cell Analysis . . . 31
2.4 Analysis of the Cell Layer Integrity . . . 32
2.4.1 Transendothelial Electrical Resistance Measurements . . . 32
2.4.2 Molecular Permeability Assay . . . 33
2.4.3 Histological Analysis of Cross Sections . . . 34
2.5 Cellular Staining . . . 35
2.5.1 Prussian Blue Staining . . . 35
2.5.2 Pappenheim Staining . . . 36
2.6 Fluorescent Staining for Confocal Laser Scanning Microscopy . . . 37
2.6.1 Phalloidin Staining . . . 37
2.6.2 Immunofluorescence Staining of *zonula occludens*-1 . . . 38
2.7 Flow Cytometry . . . 39
2.7.1 Flow Cytometry-Based Particle-Cell Interaction . . . 40
2.7.2 Surface Marker Expression of Differentiated Cells . . . 40
2.8 Detection and Quantification of SPIONs . . . 41
2.8.1 Magnetic Particle Spectroscopy . . . 42
2.8.2 Atomic Absorption Spectroscopy . . . 43
2.9 Transmigration through Blood-Brain Barrier Model . . . 44
2.10 Statistical Analyses . . . 45

3 Results **47**
3.1 Interaction of SPIONs with HBMEC . . . 48
3.1.1 SPION-associated Effect on Cell Viability . . . 48
3.1.2 Binding of SPIONs to Cells and Particle Uptake . . . 48
3.1.3 Protein Corona-associated Effects on Cytotoxicity and SPION Interaction with Cells . . . 51
3.2 Establishing and Optimizing the Blood-Brain Barrier Model . . . 59
3.2.1 Testing of Transwell System and Cell Seeding Density . . . 59

3.2.2 Influence of Cell Media Supplements on HBMEC Layer Integrity 59
3.3 Interaction of SPIONs with the Blood-Brain Barrier Model 63
3.3.1 SPION-associated Effects on Barrier Integrity 63
3.3.2 Passage of SPIONs through *in vitro* Blood-Brain Barrier Model 64
3.4 SPION-induced Passage of Immune Cells trough Blood-Brain Barrier Model 70
3.4.1 SPION-mediated Transmigration of neutrophil-like HL-60 across Blood-Brain Barrier Model 70
3.4.2 SPION-mediated Transmigration of monocytic THP-1 across Blood-Brain Barrier Model 71

4 Discussion **75**
4.1 General Biological Effects of SPIONs and Impact of the Protein Corona 77
4.2 SPIONs and the Blood-Brain Barrier Model 84
4.3 SPIONs and Barrier-penetrating Cells 92

5 Conclusion & Outlook **97**

A Materials **101**

B Supplement **107**
B.1 Incubation Conditions Influence the SPION-associated Protein Corona Formation 107
B.2 SPION-associated Cytotoxicity Depends on Proliferative State . . 108
B.3 Cationic SPIONs barely Pass Transwell Membranes 109
B.4 Endocytosis Inhibitors Affect Barrier Integrity 109
B.5 SPION-induced Passage of Immune Cells trough Blood-Brain Barrier Model 110

References **115**

Acknowledgements

Ehrenwörtliche Erklärung

Nomenclature

AAS	atomic absorption spectroscopy
ABC	ATP-binding cassette
ACM	astrocyte-conditioned medium
APC	allophycocyanin
aqua bidest.	*aqua bidestillata*; twice distilled water
AU	arbitrary unit
BBB	blood-brain barrier
BMEC	brain microvascular endothelial cells
BSA	bovine serum albumin
CNS	central nervous system
D-PBS	Dulbecco's phosphate-buffered saline
DEAE	diethylamine ethyl
DMSO	dimethyl sulfoxide
EDTA	ethylenediaminetetraacetic acid
EGF	epidermal growth factor
EMA	European Medicines Agency
EPR	enhanced permeability and retention
F-actin	filamentous actin
FCS	fetal calf serum; also denoted as fetal bovine serum (FBS)
FDA	Food and Drug Administration
FGF	fibroblast growth factor
FITC	fluorescein isothiocyanate
fMLP	*N*-Formylmethionyl-leucyl-phenylalanine
GDNF	glial cell-derived neurotrophic factor
HBMEC	human brain microvascular endothelial cells
HUVEC	human umbilical vein endothelial cells

IL	interleukin
MAGUK	membrane-associated guanylate kinase
MCP-1	monocyte chemoattractant protein-1; also known as CC-chemokine ligand 2 (CCL2)
MPS	magnetic particle spectroscopy
MRI	magnetic resonance imaging
MRP	multidrug resistance-associated protein
NaFl	sodium fluorescein
P-gp	P-glycoprotein
PAM	polyacrylat-co-maleat
PdI	polydispersion index
PE	phycoerythrin
PE (buffer)	D-PBS supplemented with EDTA (2 mM)
PEG	polyethylene glycol
PEI	polyethylenimine
PET	polyethylene terephthalate
PMA	phorbol 12-myristate 13-acetate; also known as 12-O-tetradecanoylphorbol-13-acetate (TPA)
PTFE	polytetrafluoroethylene
RES	reticuloendothelial system
RFU	relative fluorescence units
RPMI	Roswell Park Memorial Institute; cell culture medium
RT	room temperature (19–23 °C)
SDS-PAGE	sodium dodecyl sulfate polyacrylamide gel electrophoresis
SPARC	secreted protein acidic and rich in cysteine
SPION	superparamagnetic iron oxide nanoparticle
SSC	side scatter
TGF	transforming growth factor
ZO-1	*zonula occludens-1*; tight junction-associated protein
ZONAB	ZO-1-associated nucleic-acid binding protein

List of Figures

1.1 Diversity of nanoparticle design. 4
1.2 Endocytotic pathways ingesting nanoparticle into mammalian cells. 10
1.3 Structure and effects of the protein corona on nanoparticles. . . . 15
1.4 Cellular components and structure of the neurovascular unit forming the blood-brain barrier (BBB). 17

3.1 PrestoBlue™ cell viability assays of HBMEC exposed to diverse types of SPIONs. 49
3.2 Cellular interaction of diverse types of SPIONs with HBMEC. . . 50
3.3 Cellular uptake mechanisms of SPIONs analyzed by confocal laser scanning microscopy. 52
3.4 Acute and long-term cell viability studies of HBMEC exposed to SPIONs with varying levels of protein corona. 53
3.5 Cellular interaction of SPIONs and cell viability of HBMEC upon exposure, analyzed by flow cytometry. 56
3.6 Protein corona-associated uptake of SPIONs into HBMEC analyzed by confocal laser scanning microscopy. 57
3.7 Effect of the protein corona on cellular SPION uptake mechanisms analyzed by flow cytometry and confocal laser scanning microscopy. 58
3.8 *In vitro* blood-brain barrier models formed by HBMEC cultivated on PET or PTFE membrane inserts. 60
3.9 Influence of cell culture media and media supplements on barrier integrity parameters. 62
3.10 SPION-associated effects on barrier integrity parameters of HBMEC layers. 65
3.11 SPION distribution of distinct compartments of the *in vitro* blood-brain barrier model analyzed by magnetic particle spectroscopy (MPS). 68

3.12 SPION distribution of distinct compartments of the *in vitro* blood-brain barrier model analyzed by atomic absorption spectroscopy (AAS). 69
3.13 Transmigration of differentiated, SPION-loaded HL-60 cells across the *in vitro* blood brain barrier model. 73
3.14 Transmigration of differentiated, SPION-loaded THP-1 cells across the *in vitro* blood brain barrier model. 74

B.1 Gel electrophoretic analysis of protein corona formation on SPIONs. 107
B.2 Zeta potential measurements of SPIONs with diverse protein coronas. 108
B.3 Real-time cell analysis of HBMEC exposed to SPIONs. 108
B.4 Analysis of membrane passage of cationic SPIONs by magnetic particle spectroscopy (MPS). 109
B.5 Analysis of cell layer integrity under the influence of endocytosis inhibitors. 109
B.6 Analysis of differentiation of HL-60 and THP-1 by flow cytometry and microscopic investigation. 110
B.7 Cellular interaction of diverse types of SPIONs with HBMEC and differentiated HL-60 and THP-1. 111
B.8 PrestoBlue™ cell viability assays of HBMEC and differentiated HL-60 and THP-1 exposed to diverse types of SPIONs. 111
B.9 Analysis of cell layer integrity under the influence of inflammatory cytokines. 112
B.10 Barrier integrity of cell layers and iron content of lower acceptor compartments after passage of differentiated HL-60 and THP-1 . 113

List of Tables

2.1 Characteristics of experimentally used SPIONs. 26
2.2 Dehydration steps performed by the automatic tissue processor. . 34
2.3 Paraffin removal and hydration or dehydration steps performed during staining of histological cross sections. 35
2.4 Composition of the secondary antibody solution for immunofluorescence ZO-1 staining. 39
2.5 Composition of the antibody mixture for characterizing monocytic or neutrophilic surface markers. 41

A.1 List of used chemicals. 101
A.2 List of used reagents and media. 102
A.3 List of used fluorescent dyes and antibodies. 103
A.4 List of used Consumables. 104
A.5 List of used technical devices and instruments. 105

Abstract

Superparamagnetic iron oxide nanoparticles (SPIONs) represent a highly promising class of nanoscale formulations offering great potential for various biomedical applications. While the large degree of freedom in SPION synthesis allows their tailor-made preparation, the resulting particle multitude demands an adequate risk and impact assessment for every individual formulation. Moreover, SPIONs' unique physicochemical properties often interfere with established examination methods. Hence, appropriate *in vitro* models combined with convenient analysis methods are crucially needed. Biological barriers influence cellular exposure and thus, intrinsic reactions to SPIONs upon entry into the body. The effects of SPIONs on the barrier integrity are of vital importance for the whole organism, too, whereby the blood-brain barrier (BBB) is an indispensable example. Hence, in scope of this study a standardized *in vitro* model representing the human BBB is established for the detailed evaluation of SPIONs' interactions.

For this purpose a transwell system based on human brain microvascular endothelial cells (HBMEC) is established, whereby barrier integrity is evaluated by transendothelial electrical resistance, molecular permeability assays, and microscopical analyses. SPIONs of diverse surface coating and charge are tested. The application of magnetic particle spectroscopy for the direct and highly sensitive SPION detection is successfully demonstrated in context of such biological models for the first time. For investigating the cell-mediated SPION delivery across the BBB, HL-60 and THP-1 differentiated into neutrophilic and monocytic cells are utilized.

Data indicate that starch-coated SPIONs traverse the barrier in a time-dependent manner, which can be explained by clathrin-induced transcytosis. At the same time barrier integrity remains unaffected apparently based on slow cellular accumulation of these neutral particles. In contrast, anionic SEON^{BSA} intensively accumulates within the barrier-forming cells and affects the model in a barrier-disrupting manner. Addressing cell-mediated SPION delivery across the BBB by neutrophils and monocytes, results clearly show that the engulfment of anionic SEON^{PAM} by both cell types massively enhances cellular barrier penetration. It is further augmented upon stimulation by a magnetic field. This migration-inducing effect of SPIONs emphasizes its particular consideration during the treatment of patients suffering from neuroinflammatory diseases. Moreover, data on neutrophil-like HL-60 imply that they can deliver SPIONs across this *in vitro* model, which can be exploited for targeted SPION delivery.

Taken together, the here presented thesis demonstrates a versatile and reliable *in vitro* test system for the comprehensive analysis of SPIONs' interactions at the BBB. Hence, it offers a powerful platform for the detailed assessment of diverse SPIONs, which aids to implement sophisticated and novel SPION-based biomedical applications to overcome current medical problems.

Zusammenfassung

Die Vielfältigkeit in der Gestaltung superparamagnetischer Eisenoxid-Nanopartikel (SPIONs) erlaubt einerseits deren maßgeschneiderte Präparation, welche ein enormes Potential für zahlreiche biomedizinische Anwendungen bietet. Andererseits bedingt dies eine adäquate Risiko- und Folgenabschätzung für jede einzelne Partikelkomposition. Weiterhin limitieren physikochemische Eigenschaften der SPIONs die Funktionsweise bisher etablierter Untersuchungsmethoden. Besonders im Hinblick auf die Analyse der Interaktion von SPIONs mit biologischen Barrieren sind daher geeignete *in vitro* Modelle sowie angemessene Analysemethoden zwingend erforderlich. Hierbei kommt der Blut-Hirn-Schranke (BBB) und der Wirkung von SPIONs auf diese hinsichtlich Partikelexposition und Barriereintegrität eine besondere Bedeutung zu. Im Rahmen dieser Dissertation wurde ein standardisiertes *in vitro* Modell etabliert, welches die humane BBB repräsentiert und die eingehende Untersuchungen SPION-assoziierter Interaktionen erlaubt.

Zu diesem Zweck wurde ein Transwell-System basierend auf *human brain microvascular endothelial cells* (HBMEC) implementiert. Der Einflusses von SPIONs unterschiedlicher Oberflächenbeschichtung und -ladung auf die Barriereintegrität erfolgte mittels transendothelialem elektrischem Widerstand, molekularen Permeabilitätstests und mikroskopischen Analysen. Erstmals wurde Magnetpartikelspektroskopie zur hoch sensitiven SPION-Detektion im Kontext biologischer Barrieremodelle erfolgreich angewendet. Zur Erforschung des Zell-vermittelten SPION-Transports über die BBB wurden HL-60 bzw. THP-1 zu Neutrophilen bzw. monozytären Zellen differenziert.

Die Ergebnisse zeigen, dass stärkebeschichte SPIONs die Barriere zeitabhängig durchdringen, was vermutlich über Clathrin-vermittelte Transzytose erfolgt. Dabei bleibt die Barriereintegrität weitgehend unbeeinträchtigt und ist auf die verlangsamte zelluläre Anlagerung dieser neutralen Partikel zurückzuführen. Im Gegensatz dazu akkumulieren anionische SEON$^{\text{BSA}}$ verstärkt an und in barriereformenden Zellen und stören damit die Barriereintegrität. Außerdem zeigt sich, dass die Beladung von Neutrophilen und Monozyten mit anionischen SEON$^{\text{PAM}}$ deren Barrieredurchdringung immens verstärkt, was durch magnetische Stimulation zusätzlich gesteigert wird. Diese migrationsinduzierende Wirkung der SPIONs muss daher zwingend bei der Therapierung neuro-inflammatorischer Erkrankungen, berücksichtigt werden. Andererseits kann die Tatsache, dass neutrophile HL-60 Zellen SPIONs durch das hier etablierte *in vitro* Barrieremodell schleusen, zur gezielten Partikelauslieferung genutzt werden.

Zusammenfassend wird in dieser Arbeit ein vielseitiges und stabiles *in vitro* Testsystem für die eingehende Untersuchung von Wechselmechanismen zwischen SPIONs und der BBB vorgestellt. Damit trägt diese Plattform letztlich dazu bei, fortschrittliche und neue SPION-basierte biomedizinische Anwendungen zu implementieren und aktuelle Problemstellungen der Medizin zu überwinden.

CHAPTER 1

Introduction

Whereas nanotechnology is considered a young scientific field, first arisen in the late 20^{th} century, the production and utilization of nanoscale objects for special demands has been carried out for over a thousand years, however most likely unsuspectingly. The most prominent and oldest preserved example is the Lycurgus Cup embodying a dichroic Roman glass cage cup from the 4^{th} century [1]. The probably accidental contamination of the glass with nano-sized gold colloids along with silver nanoparticles during its production causes an impressive effect: depending on the conditions of illumination the antique cup appears red under transmitted light, while light shining from the outside turns the cup green. In the course of time such coloring properties mediated by metallic nanoparticles were utilized for staining glass for church windows during the Medieval [2] and creating dyes decorating ceramics during the Renaissance period [3, 4]. In 2006, high-resolution transmission electron microscopy revealed carbon nanotubes and cementite nanowires in Damascus steel, which most likely cause the characteristic banding and exceptional sharp-cutting edges of blades crafted from this steel more than 400 years ago [5]. Highlighted by these examples, based on the large fraction of surface atoms and resulting high surface energy, nano-scaled objects present extraordinary chemical, physical, and mechanical properties, usually completely different from those of respective bulk materials [6, 7]. This is why, modern nanotechnology is an interdisciplinary field combining the natural sciences of physics, chemistry, biology, and medicine as well as information technology and electrical engineering, which has already resulted in numerous diverse commercial applications [8–10]. Technically, the term "nanoparticle" is often limited to objects with sizes of 1–100 nm in at least one dimension [11]. However, a strongly enhanced surface-to-volume-ratio of larger nano-scaled objects compared to bulk material, still confers unique properties and causes the extension of the definition of nanoparticles to several hundreds of nanometers [10, 12–14]. The occurrence of nanoparticles spreads from natural sources including volcanic ashes, wind erosion, and cosmic dust [15], to man-induced generation of byproducts such as road-tire interaction or emissions from power plants and air crafts [16], and engineered nanoparticle formulations. Today, we meet engineered nanoparticles present in consumer products everywhere: silver and gold nanoparticles providing antibacterial and antimicrobial effects in tooth paste and food packaging as well as in clothes [17]; titanium oxide and zinc oxide nanoparticles in sunscreens absorbing UV light while making the lotion transparent [18]; carbon-nanotubes in bicycles and rackets making them both stronger and lighter [19]; silicon nanowires in ever smaller batteries for electronic devices [20]; and many more.

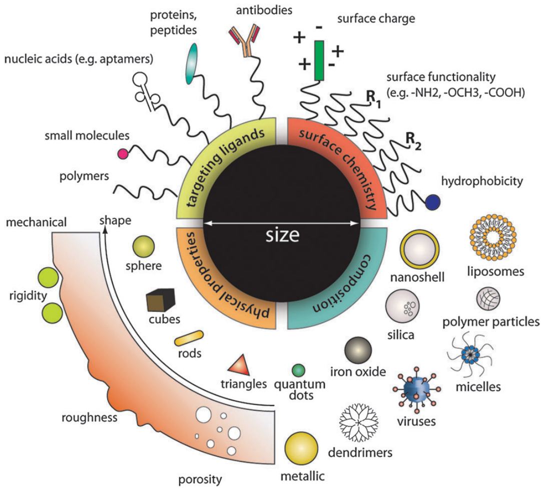

Figure 1.1: Diversity of nanoparticle design. Nanoparticles can be designed modularly. Features such as material composition, physical properties, surface chemistry, and ligand functionalization can be tailored according to their application. Figure taken with permission from [21].

The vast diversity of nanoparticles as depicted in figure 1.1 can be accredited to the various possibilities in particle design as parameters including core material, shape, size, surface charge, and additional functionalization can be tailored according to the implementation [21]. Nevertheless, due to this plethora and omnipresence of engineered nanoscale objects, the exposure of humans and environment to these materials steadily increases and investigations regarding biological consequences are lacking but more and more relevant.

1.1 Nanomedicine

A broad and highly promising branch of nanotechnology is covered by nanomedicine—the field of health and medicine involving the development and application of nanoscale objects for diagnostic and therapeutic purposes as well as monitoring and preventing diseases. Thus, it is expected that nanomedicine will improve early diagnosis and treatment of a wide range of diseases by the development of better devices, highly specific and efficient drugs, and innovative therapies [10]. More precisely, the utilization of nanoparticle formulations and nanodrugs can help to overcome obstacles like the appearance of in parts severe side effects, instability of drugs, drug delivery to difficult-to-reach sites, and bioavailability, while at the same time increasing therapeutic efficiencies [22]. Passive drug targeting usually is achieved by enhanced permeability and retention (EPR) effects often prevailing in fenestrated tissues and leaky vessels of tumors combined with low lymphatic drainage [23]. By specific conjugation of nanoparticles with ligands directed towards cellular surface or environmental markers, particles can be targeted actively to sites of interest such as tumors, metastases, or inflammation [24]. A horizontal scan published in 2015 by Noorlander and co-workers identified 43 and 71 clearly assigned nanomedicinal products already approved for clinical use by the European Medicines Agency (EMA) and Food and Drug Administration (FDA), respectively, [25]. The authors identified most of the products being designated to therapeutic applications, especially cancer treatment, whereas nanomedicinal objects directed towards diagnosis and vaccines constitute a small percentage only. For instance, human serum albumin nanoparticles loaded with paclitaxel show enhanced efficacies compared to conventional taxane-based therapies in the treatment of early stage and metastatic breast cancer patients and also indicate to be beneficial for treatment of non-small cell lung cancer and pancreas carcinoma [26]. Currently in clinical testing is a strategy to increase the efficacy of imaging technologies for direct focal ablation of prostate tissue, where gold-coated silica nanoparticles are used for directing laser irradiation in neoplasms of the prostate [27]. Another promising application is based on the antibacterial effects of nanoparticles, which can help to treat life-threatening bacterial infections to overcome antibiotic resistance [28].

In terms of medical diagnosis of diseases including cancer and genetic mutations, nanoparticles can be utilized for both laboratory-based testing and *in vivo* imaging methods. By using nanoscaled objects, unique biological markers within patient samples can be screened or very small amounts of biological samples can be investigated by lab-on-the-chip tools performing a whole range of laboratory tasks and even single cell analysis [29, 30]. For instance, mutational analysis can be realized highly sensitively and rapidly using nanotechnology as shown by Vanden Bon and colleagues [31]. They demonstrated that phenylketonuria-associated mutations in DNA fragments of the *phenylalanine hydroxylase*-encoding gene alter the heat-transfer resistance of denaturing DNA fragments immobilized on carboxyl-functionalized nanocristalline diamond sensor electrodes. With regard to *in vivo* imaging, the visualization of structures inside the human body presents a valuable resource for clinicians to identify diseased tissues at an early stage and decide further treatment strategies. In this context, computer tomography (CT), magnetic resonance imaging (MRI), positron emission tomography (PET), single-photon emission computed tomography (SPECT) and optical coherence tomography (OCT) are applications, where the use of nanoparticles as contrast agents considerably improves the three-dimensional view of sites of interest [7, 10]. Licensed by the EMA are nanoparticle formulations based on human serum albumin and radio-labeled technetium-99m, which are used for lymphoscintigraphy and intravenous administration for bone marrow scintigraphy or visualization of inflammatory processes in areas other than the abdomen [32].

The highlights of nanomedicinal applications mentioned above, emphasize the enormous potential of nanoparticles for a wide range of purposes to solve medical problems and improve clinical outcomes. However, despite the considerable number of described and experimentally tested formulation, only few nanoparticle formulations have been introduced into clinics [33]. As proposed by Pelaz *et al.* a major scientific challenge is the lacking knowledge about the behavior of nanoparticles inside living organisms [10]. In order to bridge the gap between laboratory and clinics an intensive and multidisciplinary cooperation between physicists, chemists, biologists, pharmacists, and physicians is of vital importance.

1.1.1 Superparamagnetic Iron Oxide Nanoparticles

A special class of nanoparticles is constituted by superparamagnetic iron oxide nanoparticles (SPIONs), whose magnetization appears to be zero in the absence of an external magnetic field, whereas they behave similarly to a paramagnet under the influence of an external magnetic field [34]. Cores of such particles are made of the two main forms, magnetite (Fe_3O_4) or its oxidized product maghemite (γ-Fe_2O_3), and usually comprise multiple domains with single magnetic domain sizes below 12–15 nm in order to achieve the superparamagnetic character [35,36]. While its saturation magnetization is moderate only [37], in contrast to other hard nanoparticles including cobalt and nickel the essential element iron is naturally occurring in the human body and therefore not associated with any intrinsic risk [38]. The daily uptake of iron via dietary products is estimated to 1-2 mg, whereby upon its metabolization it is used as essential cofactor of several enzymes and proteins [39]. However, not only iron deficiency constitutes a general problem in human health, but also iron excess and accumulation within cells and organelles can result in pathological disorders [40]. Usually, SPIONs are equipped with an additional coating surrounding the iron oxide core in order to maintain colloidal stability especially in aqueous solutions and to protect the iron core from further oxidation. Such coatings are adopted according to the application and are also important for particles' biocompatibility and biodegradability. Additionally, they open the possibility of ligand conjugation for further functionalization [41, 42]. For instance, polymers such as polysaccharides and polyethylene glycol (PEG) are frequently used materials showing good biocompatibility [43], while silica coatings allow low loss rates of transmitted light and therefore are widely used for bio-imaging and bio-sensing purposes [44].

The superparamagnetic property of SPIONs opens up new and highly attractive applications especially in the biomedical field. Thus, they can be utilized for site-specific drug delivery during magnetic drug targeting, as contrast agents for magnetic-based imaging techniques, as heat inducers in hyperthermia anticancer therapy, in magnetic tissue engineering, and for cell labeling and *in vivo* cell tracking [10, 41, 42, 45]. As the first nanomedicinal product, ferumoxil (also known as Lumirem®)—a siloxane-coated SPION of 300 nm—was approved by the EMA as an MRI contrast agent in 1994 and since then four more SPION products have been introduced into clinics until today [25]. The shortening effect of SPIONs on especially transverse relaxation time T2 induces a signal loss during MRI, which results in a negative (*i.e.*, dark) contrast image [46]. In addition, approaches utilizing aminosilan-coated SPIONs together with application cycles of alternating magnetic fields are approved for efficient hyperthermia treatment of tumor entities such as glioblastoma and other entities [47]. Thus, clinical trials revealed an improvement of median survival time from 6.2 months to 13.4 months without any complications compared to conventional therapy of glioblastoma [7]. Further studies indicate that hyperthermia treatment prior to radiotherapy induces a radiosensitizing effect on glioma cells [46].

A currently arising new nanomedical sector is formed by the fusion of diagnostic and therapeutic applications, called "theranostics" [48]. Particularly, theranostics allows both monitoring of pharmacokinetics via methods such as imaging and therapeutic treatment of diseases including cancer. Thereby, multi-step procedures are eliminated, which in turn accelerate disease treatment, and pave the way for individualized medicine. Especially SPIONs are highly predestined candidates for theranostic implementations as their multifunctional potential easily allows the combination of contrast-enhancing features in MRI with magnetic drug targeting and hyperthermia-based cancer therapy [41]. Impressively, pre-clinical investigations performed by Hayashi *et al.* using SPIONs hetero-functionalized with PEG and folic acid, demonstrated efficient particle accumulation in myeloma cancer tissues of mice resulting in enhanced contrast during MRI [49]. At the same time, the application of an external alternating magnetic field specifically induced local hyperthermia, promoted tumor shrinkage and significantly prolonged overall survival of diseased animals.

Despite the various beneficial and promising functions of SPIONs in biomedicine, there are still several obstacles limiting their unconditional use. A major aspect comprises the fact that studies have revealed that only a small proportion of actively targeted SPIONs actually reach target tissue [24]. To overcome this problem by magnetic drug targeting, magnetic field configurations allowing elevated penetration depths are critical as the magnetic field strength shrinks cubically with growing distance. Furthermore, premature burst of drug cargoes, especially at instillation time points, impair delivery efficiencies to target sites and may evoke cytotoxic side effects [50]. The so-called protein corona comprising an adsorptive layer of ambient proteins on the particles' surface immediately after contact with the environmental medium, can critically influence biological effects of SPIONs and thus, hamper intended purposes [51]. This phenomenon also impedes the comparability of data obtained from both *in vitro* and *in vivo* studies using similar particle formulations and might induce their premature immunologic clearance from the blood stream caused by the reticuloendothelial system (RES). Finally, in several cases the fate of internalized SPIONs into cells and its biodistribution are not clear, whereas for a safe and effective clinical application such information is of vital importance. Hence, more standardized studies related to these issues are imperatively needed [41].

1.1.2 Uptake Mechanisms for Nanoparticles

Uptake mechanisms for nanoparticles into the human body are versatile as they can enter via different routes such as the lungs after inhalation, the skin by dermal application or by enteral resorption upon ingestion [52]. In terms of biomedical applications, direct intravenous administration is widely used—especially in case of cancer nanotherapeutics [53]. The nanoparticles' biodistribution upon this systemic administration modality is determined according to particle size, shape, surface charge and other surface properties [54]. However, nanoparticle dissemination is predominantly confined to the vascular system and organs of fenestrated endothelium such as liver, spleen, and kidneys as well as tumors and other sites of inflammation as they are characterized by leaky vessels and fenestrated endothelium, too [54]. While for passive targeting, advantage is taken of the EPR effect (see section 1.1), active targeting by grafting distinctive ligands, markers, or functional groups onto particles' surface can considerably affect their accumulation and elevate local concentrations at specific target sites. Similarly, magnetic drug targeting in case of SPIONs and other magnetic nanoparticles displays another relevant option for actively directing particle distribution. As a consequence of their size in a typical range of subcellular components and biological molecules [55], nanoparticles can show intensive cellular interactions and be taken up into cells via distinct endogenous uptake mechanisms. Usually, nanoparticles are taken up into cells by active endocytotic pathways, though the cellular entry via passive diffusion has been described as well, especially in case of cationic particle formulations [56, 57].

While large particles with exceeding sizes of 500 nm can only be engulfed by specialized cells including macrophages and neutrophils via phagocytosis, the ingestion of smaller particles via pinocytotic vesicles can be actioned by virtually all types of eukaryotic cells [58–60]. The binding affinity mediated by hydrophobic or electrostatic interactions and receptor-ligand binding to cellular surfaces plays a crucial role for the first step of particle internalization. In this context, diverse studies revealed that cationic surface charges of nanoparticles show intensive interactions with anionic phospholipids or protein domains originating from the glycocalyx (*e.g.* sialic acids) of cellular plasma membranes [62], whereas neutral and anionic nanoparticles show less-pronounced membrane adsorption and subsequent particle internalization [57]. Additionally, the elevated abundance of negatively charged phosphatidylserine in the cytosolic leaflets of the plasma membrane, endosomes and lysosomes is thought to strengthen the entry of cationic proteins to endocytotic pathways [63]. As indicated by figure 1.2, subsequent endocytotic ingestion is distinguished into macropinocytosis, caveolin-dependent endocytosis, clathrin-mediated endocytosis, and pathways independent from both clathrin and caveolin with further sub-classifications [64, 65]. Most studies focus on clathrin-mediated endocytosis when investigating uptake mechanisms for particles below 200 nm [61, 66], though other processes and even an interplay of several pathways might occur [67]. Regardless of whether particle internalization is induced via plasma membrane invaginations at clathrin-coated pits (*i.e.*, clathrin-mediated endocytosis), cholesterol-rich domains (*i.e.*, caveolin-dependent endocytosis), or other

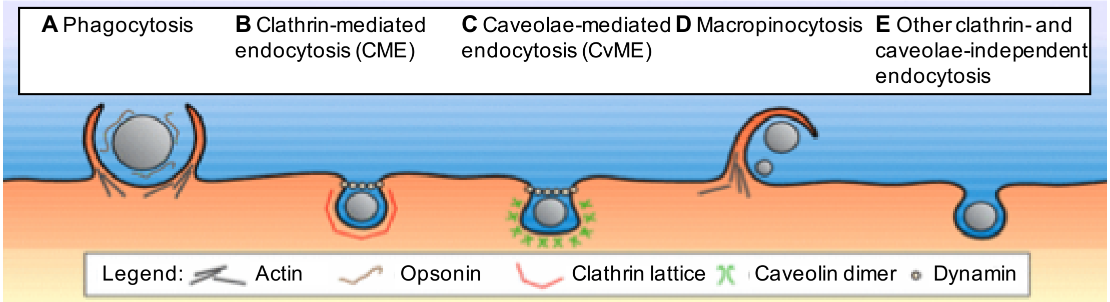

Figure 1.2: Endocytotic pathways ingesting nanoparticle into mammalian cells. Phagocytosis (**A**) primarily occurs in professional phagocytes. Clathrin-mediated endocytosis (**B**) depends on the GTPase dynamin, while calveolae-mediated endocytosis (**C**) at caveolin-coated pits does not necessarily require dynamin. Non-selective particle engulfment can also happen via macropinocytosis (**D**) or other endocytotic pathways independent from clathrin and caveolin. Figure taken with permission from [61].

active processes, membrane-budded vesicles transfer the nanoparticle cargo into early endosomes first [60]. Within these compartments, which possess a mild acidified milieu, receptors can be recycled and digestion off the received material by hydrolysis is initiated as well as its sorting into delivery to specific intracellular compartments or transcytotic pathways [68]. Next, the cargo is directed to acidic late endosomes with increasing proteolytic activity before it finally enters lysosomes. For nanoparticle cargoes directed to distinct subcellular targets, pathways avoiding the lysosomal destination of the nanoscaled vehicle are indispensable for successful implementations. Indeed, endosomal escape has been shown for some nanoparticle formulations [41, 69, 70]. Especially a strongly cationic particle surface charge seems to promote the escape from endosomes to reach the cytoplasm via destabilization of endosomal membranes by mechanisms including ion-pair formation with anionic lipids and endosomal/lysosomal buffering, swelling, and rupture (*i.e.*, the "proton sponge effect") [71]. Besides the resulting cytosolic delivery, targeting of distinct cellular compartments such as nucleus, mitochondria and Golgi have also been pursued [53].

As mentioned earlier, besides surface chemistry, the level of nanoparticle interaction with cells is significantly influenced by particles' properties including size and shape as well as the cellular type itself and the microenvironment as it can induce the protein corona formation, which in turn provides the particle with a new biological identity [41, 56]. In terms of particle size, gathered data emphasize that, in general, smaller particles are internalized more intensively, although a minimum size seems beneficial for efficient induction of particle uptake probably due to sufficient cross linking of membrane receptors [56,59,66,72]. In this regard, Win and co-workers observed that polystyrene nanoparticles of 100 nm show most pronounced particle internalization into adenocarcinomal cells, while the uptake of larger (200–1000 nm) particles is gradually decreased and lowest for 50 nm [73].

1.1.3 Biologic and Cytotoxic Effects of Nanoparticles

As the variety of biomedicinal nanoparticles is huge, so are their biological effects. According to the particle type, they can influence cell physiology in many different ways. Obviously, particles characterized by an intensive cellular interaction bring along a great capability for influencing both vitality and physiology of cells. The particle's ability to penetrate biological barriers and their resulting biodistribution are crucial factors determining nanoparticle-induced outcomes on the systemic level. Apart from particle size, shape, dose, incubation duration, and type of exposed cells, especially surface coating and functionalization play a substantial role in determining biological effects [41, 74]. While on the one hand they can enhance particle uptake increasing intracellular nanoparticle concentrations, on the other hand they can promote intracellular trafficking and endosomal escape as implied in section 1.1.2. Thus, many studies have identified a cationic surface charge of nanoparticle formulations as decisive factor mediating cytotoxicity via various mechanisms [38, 74–76] including the induction of nanoscale holes within plasma membranes, which promotes substantial membrane damage resulting in cell death [77]. Fischer *et al.* demonstrated that besides the cationic surface net charge, the charge density and flexibility of the three dimensional structure of the coating molecules also essentially determine biological effects [75]. Endosomal escape of cationic nanoparticle formulations explicitly results in the presence of bare particles within the cytosol, which in turn can induce direct interaction of particles with cellular organelles and proteins including the actin cytoskeleton inducing destabilization and cell cycle arrest [38]. Apart from cationic surface charges, anionic nanoparticles are associated with cytotoxic effects, too, whereas neutral particles are largely non-toxic [57, 76, 78]. A reasonable cause for this is provided by respective studies which show the low adherence of particles coated by dextran, starch or other neutral materials at the polar plasma membrane, whereas anionic nanoparticles can still cluster at the sparse membrane areas constituting positive charges [57, 79]. Based on the fact, that the hydrodynamic size of nanoparticles (and particle agglomerates) affects particles reactivity—whereby large surface-to-volume ratios render elevated surface energies—small particles tend to be more toxic compared to larger ones [70, 76, 80]. Finally, the formation of a protein corona can also influence biological effects of distinct nanoparticles as described in section 1.1.5.

After depletion of coating material, cells are exposed to the particle's often inorganic core, which in the case of SPIONs is *per se* considered as biocompatible in contrast to silver, cadmium or other metals [38, 56]. However, during further degradation, increasing contents of free iron ions can cross mitochondrial membranes reacting with hydrogen peroxide and oxygen during the Fenton reaction giving rise to highly reactive hydroxyl radicals [38, 56]. The resulting oxidative stress can provoke radical damage of DNA and other components including the cytoskeleton, which brings on inflammatory processes and cytotoxic events [76]. Aside from reactions directly affecting viability, sustainable impacts on cell physiology promoted by altered signal transduction profiles are also critical. An enhanced expression of cell signaling proteins integrating extracellular signaling from the membrane to the nucleus has been revealed by Berry *et al.* [81]. Interestingly, another comprehensive study performed by Mahmoudi and colleagues observed a particle charge-dependent effect on gene expression levels in different cell lines [74]. Based on their experimental results, the exposure of the cationic SPIONs strongly provoke oxidative stress, cell growth inhibition, and finally can induce apoptosis.

1.1.4 Biodegradation and Excretion of Nanoparticles

The ideal and safe nanomedical product for *in vivo* applications does not cause any off-target effects on the biological system after cargo delivery or related implementation. Especially when using them as diagnostic agents this requirement seems even more reasonable as the nanomedicinal products might also be applied to healthy individuals and in repetitive modes, too. Hence, vehicles should rapidly and completely be eliminated from the human body preventing non-specific nanoparticle accumulation in the long term. Actually, after intravenous administration of nano-scaled objects with sizes below 10 nm a clearance via kidneys has been observed [54], whereas non-continuous fenestrated hepatic endothelium accounts for a substantial retention of particles measuring 50-100 nm [82]. Splenic filtration quickly eliminates nanoparticles between 200 nm and 500 nm from the blood stream and particles in the micrometer range predominantly accumulate in capillaries of the lungs [83]. In addition to this size-dependent endothelial permeability or barrier-rising effect of indicated organs, the RES with resident macrophages in liver, spleen, lymphs, and lungs contributes to considerable particle uptake which is additionally fostered upon protein corona formation [54,84]. Thus, the risk of only a small proportion reaching targeted tissues other than the ones just mentioned, is high. Furthermore, surface charge and coating material influence blood circulation half life, too. During *in vivo* studies in rodent-based experiments it has been observed that cationic as well as anionic particles show shorter circulation times and increased liver uptake compared to neutral dextran-coated ones [83, 85, 86]. Upon particle accumulation within liver or kidneys, excretion from the body happens via bile and feces or via urine [42, 87]. However several studies have identified nanoparticle deposits present in liver and other tissues several months after application [87–89]. Options for diminishing cellularly accumulated nanoparticles range from cellular proliferation as described by Prapainop *et al.* [90] to exocytosis and lysosomal degradation [42]. With regard to SPIONs, iron cores are metabolized after degradation of the particles' coatings. Released iron is incorporated into the body's iron pool and can be stored within liver, spleen, or bone marrow as ferritin upon complexing with the iron-binding protein apoferritin [87]. Via the transferrin complex, iron is mobilized and carried to other tissues where it can be destined to erythropoiesis where it constitutes the key element of hemoglobin [39]. However, as the long-term toxicity of metal-containing nanoparticles still remains unclear, the transition of such inorganic formulations from the laboratory into clinics relies on their clearance from the human body [10].

1.1.5 Protein Corona

The protein corona constitutes a decisive factor affecting the cellular interaction and internalization rates, thus, dedicating biological effects of nanoscaled objects [41, 53, 56]. Immediately upon contact with biological media, particularly proteins residing on the nanoparticle, are adsorbed to the particle's surface depending on both protein abundance and adsorption affinity [91]. As schemed in figure 1.3, this effect results in the formation of a hard layer of highly affine proteins and a soft protein corona comprising loosely bound protein structures extending total hydrodynamic diameters by 3–15 nm [92, 93]. According to Walkey and Chan, 125 different proteins including lipid transporters, blood coagulation and complement proteins, have been observed to be involved in the protein corona generation. They also point out that the composition of such coronas is unique to each nanomaterial [94]. With a superior blood plasma abundance between 85-90% albumin, this transport protein has been identified within the majority of protein coronas of diverse particle types [95–97], where nanoparticles with hydrophobic and charged surfaces tend to adsorb proteins more extensively compared to particles with neutral and hydrophilic surfaces [10, 84, 92, 98]. However, analyses by Tenzer *et al.* revealed that the

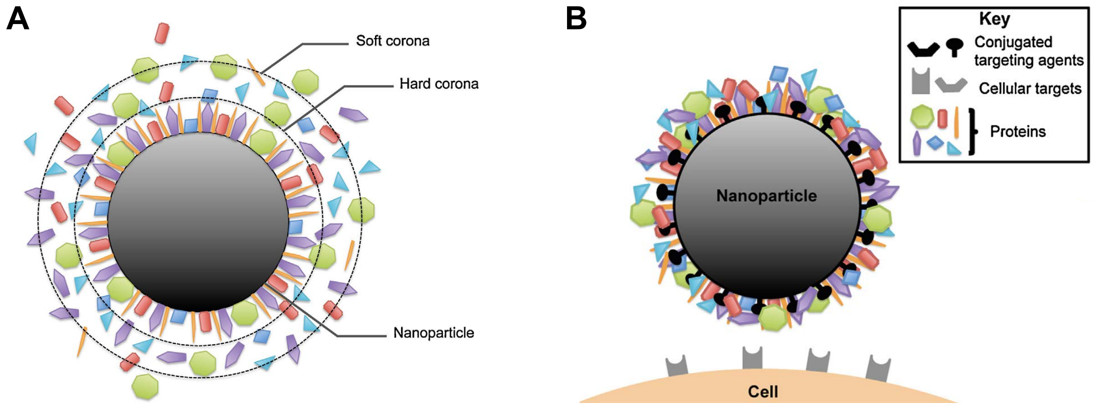

Figure 1.3: Structure and effects of the protein corona on nanoparticles. The protein corona covering the particle surface is composed of a hard and soft layer of proteins (**A**). In turn, protein coating can mask cell-specific targeting ligands linked to nanoparticle surfaces (**B**) Figure modified with permission from [92].

protein corona composition not simply reflects their relative abundance within blood plasma but comprises enrichments of lipoproteins and proteins involved in coagulation and complement pathways [96]. Comprehensive studies on the effects of particle size and charge on protein adsorption were performed by Mahmoudi and co-workers [95]. Upon the fetal calf serum (FCS)-based induction of a protein corona on anionic, cationic, or neutral SPIONs they could show that proteins of elevated molecular weights preferably adsorb to larger particles. Furthermore, the authors emphasized the role of particle surface charge, whereby large proteins are predominantly present in coronas of charged particles and coronas of cationic SPIONs constitute a bigger diversity in general. A pronounced opsonization of nanomaterials with a protein corona, on the one hand confers a rapid clearance of nanoparticles from the blood stream by the RES and on the other hand masks targeting ligands impairing delivery efficiency (see figure 1.3). Hypersensitivity reactions of patients upon a corona-triggered massive activation of the complement system are critical complications, too [38,53]. Hence, particle coatings with hydrophilic biocompatible polymers, including PEG, polyacrylic acid, and dextran, are frequently utilized to induce a so-called stealth effect [41,53]. The latter is characterized by supplying steric repulsion towards most adsorption proteins while switching to lipoproteins such as clusterin and apolipoprotein A-1, which in turn sufficiently reduce particle internalization by macrophages [53, 99]. In addition to clearance by the RES, the presence and distinct composition of a protein corona might also affect intracellular trafficking and toxicity [53]. With respect to the latter, decreasing cytotoxic effects based on the protein corona formation are particularly observed for cationic and bare inorganic particles, whereas enhancing cytotoxicity is associated with protein corona formation with conformational changes of protein contents uncovering epitopes [97,100].

1.2 Blood-Brain Barrier

As the center of the central nervous system (CNS), the brain constitutes a highly complex organ controlling all other body parts and functions. Despite its mass with only 2% relative to the total body mass, its demand for 20% of the body's nutrients is considerably high [101]. For its sufficient supply on the one hand and its protection from harmful stimuli on the other hand, the blood-brain barrier (BBB) forms a selective physiologic barrier between the peripheral circulatory system and the CNS. Thus, the maintenance of homeostatic concentrations of ions, such as Na^+, K^+, and Ca^{2+}, are considered as essential prerequisite for proper neuronal functions [102]. Furthermore, the well-controlled leukocyte migration directed across the BBB is a critical factor playing a key role in the physiologic immune surveillance, acute self-limiting inflammation, and antigen recognition [103].

1.2.1 General Structure

The BBB is maintained by a complex interplay between several components of the so-called "neurovascular unit" as depicted in figure 1.4. The central element of this unit is embodied by the endothelial cells of cerebral microvessels, also referred to as brain microvascular endothelial cells (BMEC). Compared to peripheral endothelial cells, BMECs are featured by tight cell-cell junctions lacking fenestration, increased contents in mitochondria, and minimal pinocytotic activity [102,105]. In addition to ubiquitously abundant adherence junctions, the presence of tight junctions sealing intercellular clefts between adjacent cells is characteristic for BMECs. According to figure 1.4, the formation of such tight junctions is accomplished on the one hand by transmembrane molecules such as junctional adhesion molecule (JAM)-1, occludin, and claudin, and on the other hand by membrane-associated guanylate kinase (MAGUK)

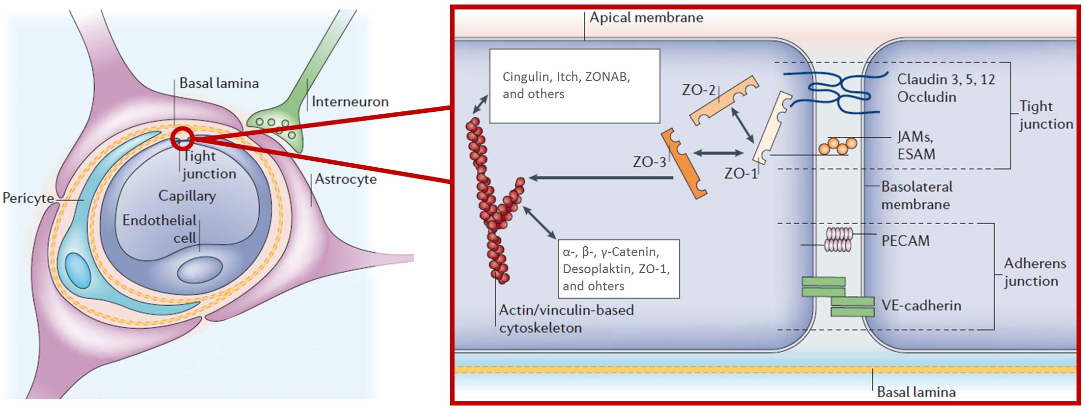

Figure 1.4: Cellular components and structure of the neurovascular unit forming the blood-brain barrier (BBB). The neurovascular unit is formed by endothelial cells surrounded by pericytes, basal membrane, and astrocytic perivascular end feet. A characteristic element of the BBB constitute tight junctions sealing intercellular clefts between adjacent endothelial cells. Transmembrane proteins occludin, claudin and junctional adhesion molecule (JAM)-1 connect junctions extracellularly, whereas *zonula occludens* (ZO)-1–3 link tight junctions to the actin cytoskeleton intracellularly. Figure modified with permission from [104]. ESAM - endothelial selective adhesion molecule; PECAM - platelet-endothelial cell adhesion molecule; VE - vascular endothelial; ZONAB - ZO-1-associated nucleic acid binding protein.

proteins, which coordinate cytoplasmic protein-protein interactions via multiple protein binding domains [102]. MAGUK proteins comprise *zonula occludens* (ZO) constructs with three subforms (ZO-1–3) joining transmembrane tight junction units with the actin cytoskeleton. The first of these proteins positively linked to tight junction was ZO-1, as its dissociation from the junctional complex has been associated with enhanced BBB permeability, although it is broadly distributed in non-epithelial cells, too [106]. Aside from BBB-strengthening juxtamembrane localization, ZO-1 can also co-localize with the nuclear transcription factor ZO-1-associated nucleic acid binding protein (ZONAB). There it co-regulates expression levels of diverse genes including ERBB2, which contributes to epithelial cell differentiation and maturation [106]. Furthermore, disruptions of BBB tight junctions by extracellular depletion of Ca^{2+} and increased intracellular Ca^{2+} levels is characterized by a loss of ZO-1, ZO-2, and occludin from cellular membranes, probably by interference of protein-protein interactions upon activation of kinase signaling cascades such as NF-κb, c-fos, and cAMP response element-binding protein. As tight junctions are located in apical cellular segments, they not only restrict paracellular permeability to molecules of a few nanometers only [70, 107] and induce strongly elevated transendothelial electrical resistance (TEER; *i.e.*, measurement of electrical resistance across cellular layer [108]), but also allow cell polarity and asymmetric distribution of membrane constituents [102]. Caused by this asymmetric and site-specific expression of receptors, transporters, and enzymes facing luminal (*i.e.*, apical membrane) or abluminal (*i.e.*, basolateral membrane) sides, the BBB additionally presents a metabolic barrier modulating the activity of toxic and neuroactive compounds. With regards to TEER, the dense abundance of tight junctions in BMECs mediates resistances of more than 1,000 $\Omega\cdot\text{cm}^2$ *in vivo* compared to 2–20 $\Omega\cdot\text{cm}^2$ in peripheral capillaries [109, 110]. As indicated in figure 1.4, apart from endothelial cells (*i.e.*, BMECs) further cell types are involved in the formation of the neurovascular unit. In this way, granular and filamentous pericytes irregularly cover abluminal membranes of BMECs forming the closest association with the endothelium. As pericytes possess contractile proteins, they are believed to be involved in the regulation of capillary blood flow [102]. Additionally, pericyte-derived angiopoetin has been shown to induce endothelial expression of occludin enhancing BBB tightness [111]. The 30–40 nm thick basal lamina encloses both pericytes and BMECs [112]. The composition of this lamina is covered by collagen type IV, heparin sulfate, proteoglycans, laminin, fibronectin, and other components of the extracellular matrix, and affects BMECs' intracellular signaling pathways and tight junction expressions via interactions with endothelial integrins [112]. Finally, astrocyte end feet connected to the basal lamina support the BBB and provide the cellular link to neurons. There is strong evidence that astrocytes influence BBB formation by regulating endothelial expression of tight junction proteins, distinct transporters, and specialized enzyme systems via secreted factors including transforming growth factor (TGF)-β, glial cell-derived neurotrophic factor (GDNF), and basic fibroblast growth factor (bFGF) [103, 104].

1.2.2 Ways across the Blood-Brain Barrier

For a sufficient supply of the brain with nutrients and the efficient efflux of metabolic waste products on the one hand, and its protection from harmful compounds on the other hand, the BBB constitutes not only a physical barrier but also a metabolic- and transport barrier, too. Small gaseous molecules such as O_2 and CO_2 can freely pass lipid membranes of the BBB as well as small lipophilic agents including alcohol, cocaine base, and barbiturates. For the transport of small hydrophilic compounds across the BBB specific transport systems on luminal and abluminal endothelial surfaces are available. The two major superfamilies of such transporters cover ATP-binding cassette (ABC) transporters and solute carriers (SLCs). Both facilitate the active transport of molecules against electrochemical gradients, whereby the first depends on ATP, while the latter couples molecule transport to another ion or molecule down its concentration gradient [113]. GLUT1 glucose carriers, several organic anion or cation transporters such as L-type amino acid transporter (LAT)-1, transporters for nucleosides and nucleobases, and many others are typical examples [114]. Whereas various of such transport systems operate bidirectional (*e.g.*, GLUT1, LAT1), some are distinctly located at luminal or abluminal endothelial surfaces only, such as for instance abluminal Na^+-dependent glutamate transporters being responsible for glutamate efflux from the brain [104]. In contrast, luminal ABC transporters comprising P-glycoprotein (P-gp) and multidrug resistance-associated proteins (MRPs) are efficient efflux pumps for waste products, environmental toxicants, and xenobiotics as well as therapeutic drugs [115]. In contrast to the transporter-mediated passage, hydrophilic molecules larger than 400-500 Da such as peptides and proteins, usually are excluded from transcellular trafficking, unless they specifically undergo receptor- or adsorptive-mediated transcytosis [46, 114]. Adsorption-mediated transcytosis relies on non-specific interactions of ligands with surface moieties expressed on luminal membrane sides of endothelial cells. It is predominantly mediated by caveolae- and clathrin-mediated endocytotic processes as well as endocytotic processes independent from clathrin and caveolin as described in section 1.1.2. The specific binding of ligands to BMECs' surface receptors such as insulin receptors, transferrin receptors, and low density lipoprotein (LDL) receptor-related proteins (LPR), are mandatory for receptor-mediated transcytosis. In this way, the brain is efficiently supplied with insulin, transferrin-bound iron, LDL, lactoferrin, and many more.

The tight regulation of transport systems across the BBB often constitutes a considerable obstacle for efficient delivery of therapeutic drugs into the brain. This holds true even when barrier impairments already pre-exist, which can arise from inflammatory and pathological conditions including stroke, meningitis, multiple sclerosis, diabetes, Alzheimer's disease, and brain tumors [116]. Therefore, specific strategies for overcoming this hurdle have been developed. The injection of hyperosmolar solutions of mannitol, lactamide, saline, or others into the brain-supplying carotid artery has been shown to transiently disrupt cerebral tight junctions by shrinking endothelial cells, which in turn improves the delivery of chemotherapeutic drugs into the CNS of patients with various types of brain tumors [117]. Similarly, chemical destabilization of the BBB by alkylglycerols efficiently limits BBB opening to 3–15 min [118]. Another strategy to temporarily access the brain, comprises acoustic cavitation of polymer- or lipid-shelled microbubbles by focused ultrasound [119]. Resulting oscillations of microbubbles induce localized disintegration of tight junctions conveying brain entry for co-applied drugs. Despite indicated conventional approaches facilitating paracellular drug transport, strategies enhancing transcellular carrying have also been developed. These include drug modification towards a more lipophilic character as well as the use of prodrugs, such as L-3,4-dihydroxyphenylalanine (L-DOPA), capable for crossing the BBB via transport systems and being converted into active forms upon entry [120]. Recently emerged approaches use nanoparticle carriers for enhanced drug delivery into the CNS [41, 70, 89, 114]. For instance, doxorubicin-loaded liposomes functionalized with cationic surface peptides have been shown to efficiently cross the BBB via adsorption-mediated transcytosis in brain tumor-bearing rats [121]. For metallic nanoparticles including SPIONs, passive diffusion, clathrin-mediated transcytosis, and trans-synaptic transport have been demonstrated as mechanisms for overcoming the BBB, whereby the additional application of an external magnetic field enhances SPION accumulation in cerebral perivascular zones within mice [118]. The conjugation of nanoparticle formulations with targeting moieties such as monoclonal antibodies, peptides, and specific plasma proteins, encourage transcellular passage through BBB-forming endothelial cells, too. Coupling of transferrin or transferrin-binding antibodies to particle surfaces are typical candidates for promoting receptor-mediated transcytosis [122]. Similarly, insulin, lactoferrin, folate, heparin-binding epidermal growth factor, and integrin $\alpha_v\beta_3$ have been utilized as ligands for CNS-directed delivery [41, 89, 118, 122]. Another common attempt includes particle coating with polysorbate 80. This non-ionic surfactant is expected to adsorb apolipoproteins A-I, B-100, and E, mimicking LDL particles, which interact with LDL receptors leading to receptor-mediated transcytosis through BBB-forming endothelial cells [123]. With respect to brain tumor-specific targeting, lactoferrin, neutrophilin-1, epidermal growth factor (EGF), antibodies directed towards vascular endothelial growth factor (VEGF) or EGF receptors including mutant EGF receptor variant III, and many others have been suggested as tumor-directed ligands conjugated to nanoparticles' surface [46]. Finally, hijacking immune and stem cells as carriers of therapeutic drugs displays a novel promising approach in hurdling the BBB [53,118]. Exploiting the tumor-trophic and inflammation-mediated barrier penetration of monocytes/macrophages, neutrophils, neural- and mesenchymal stem cells, therapeutics including genes, cytokines, enzymes, and even nanoparticles can be delivered into the CNS [118, 124]. Hence, experimental studies using neural stem cells demonstrated the transduction of soluble tumor necrosis factor-related apoptosis-inducing ligand (TRAIL) to invasive metastatic tumor deposits in the brain of mice modeling breast-to-brain metastasis [125]. Nevertheless, cell-mediated delivery of therapeutic drugs meets a number of challenges. Among others, cytotoxic effects of the cargo on the cell carrier itself and the time and location-dependent release of the therapeutic agent are major obstacles. Recent concepts combining the use of cell-mediated delivery together with nanoparticles might provide a solution to these problems, as they offer a platform for shielding carrier cells from toxic drugs while allowing controlled drug release [118].

1.2.3 Model Systems Representing the Blood-Brain Barrier

As described in section 1.2.1, the BBB constitutes a complex network of several collaborating components making a plain isolation for functional analyses complicated. In order to experimentally study different aspects with regards to BBB cell biology and screening for CNS drug permeability, diverse models have been developed. Especially high-throughput drug-screening draws on parallel artificial membrane permeability assays (PAMPA) as non-cell-based surrogate models composed of filters with lipid membranes [105]. In context of functional studies, on the one hand, *in vivo* models include animal testing usually using mice and rats as well as guinea pigs, rabbits, dogs, and monkeys [126]. Due to profound differences in anatomy, physiology, and genetics obtained results can not be directly extrapolated to the human organism [7]. Though, approaches using freshly isolated capillaries from brain tissues have been utilized for *ex vivo* studies for several decades [127,128]. As the constant availability of required human tissues is limited and animal testing should be minimized, several cell culture-based *in vitro* models representing the BBB have been developed for multifunctional analyses. The deliberate isolation of primary BMECs from porcine, bovine, murine, or ratty sources and their implementation in transwell-based studies have contributed to valuable insights into physiologic and pathophysiologic processes regarding the BBB [127, 129, 130]. Thereby, especially porcine and bovine models form tight endothelial monolayers reaching particularly high TEER values (*i.e.*, up to 2,500 $\Omega\cdot$ cm^2) accompanied by low molecular permeabilities as well as appropriate functional efflux transporter activity and tight junction expression [127, 131]. The range of experimental settings covers transwell-membrane-based mono-cultured BMECs, their co-cultivation with astrocytes or pericytes in direct contact or contact-free manner, as well as the triple culture of BMECs, astrocytes, and pericytes. Experimental data show, that elevated culturing techniques using more than one cell type, often result in the generation of tighter cellular barriers but conflicting results have also been observed [105, 127, 131]. With regards to setups representing the human BBB, only few models are available. These are either based on stem cell-derived endothelial cells or immortalized human BMEC cell lines [127]. For the latter case, the lentiviral-immortalized cell line hCMEC/D3 is most widely spread and well characterized. Whereas mono-cultured cell layers of hCMEC/D3 gain TEER values of 30–50 $\Omega\cdot$cm^2, co-culture with astrocytes raise TEERs to 60 $\Omega\cdot$cm^2 [127, 131]. Anyway, a comparative study by Eigenmann and colleagues comprising hCMEC/D3, human brain microvascular endothelial cells (HBMECs) and two other cell lines revealed that, while all four endothelial cell lines specifically expressed the adherence junction protein VE-cadherin, tight junction protein ZO-1 was only confirmed in hCMEC/D3 and HBMEC [131]. Focusing on TEER and molecular paracellular permeability, the mono-culture of HBMEC attained cell layers of highest tightness in this study. Advanced approaches applying shear stress to endothelial cells by the integration of flow conditions to the apical and/or basolateral side superiorly mimic the *in vivo* situation of the BBB. As a consequence, endothelial cells respond by structural and functional remodeling, differentiation, and result in higher TEER values as compared to static transwell models [105,132]. However, no model exactly mimics the full expression pattern of enzymes, transporters, receptors, and other structural proteins of an *in vivo* BBB [103, 127] and no gold standard *in vitro* model exists. Hence, appropriate models have to be chosen carefully according to the scientific question.

1.3 Aims of the Study

The steadily-increasing diversity of superparamagnetic iron oxide nanoparticles (SPIONs) opens up the possibility for advanced, personalized, and highly-targeted biomedical applications, though represents a serious challenge for assessing and predicting biological consequences for the organism. Critical issues for a successful particle implementation are biodistribution, tissue penetration, uptake, metabolism and storage of nanoparticles, as well as particle degradation and elimination. As all of these aspects are substantially driven by particles' interaction with biological barriers, a reliable and controllable barrier test system can help to systematically identify crucial factors involved.

That is why this study aimed to evaluate the following work packages:

1. Analysis of interaction of differently charged SPIONs with blood-brain barrier (BBB)-forming cells especially in context of protein corona-associated effects on SPIONs' biological activity.
2. Establishment of an appropriate *in vitro* model representing the human BBB based on a transwell system using human brain microvascular endothelial cells.
3. Investigation of the SPION-associated effects on the integrity of the *in vitro* model with selection of SPIONs appropriate for further analyses regarding particle passage through the barrier.
4. Analysis of the kinetics and quantity of SPION passage through the BBB-representing model using direct detection methods.
5. Evaluation of SPION transport across the *in vitro* barrier model by barrier-penetrating immune cells as well as the SPION-induced barrier penetration of immune cells.

Insights obtained from this study can thus contribute to a deep and functional understanding of particle interaction with and passage across barriers and consequences for barrier integrity. In turn, the experimental setup can be utilized for further screening of nanoparticles and particle types in a systematic manner. Finally, the gained knowledge may allow an efficient and safe implementation of tailored nanoparticles in biomedicine.

CHAPTER 2

Methods and Materials

This chapter includes a detailed description of all performed methods. Utilized materials are indicated here or as a detailed list in the appendix (A).

2.1 SPION- and Protein Corona Characterization

Nanoparticles used in scope of this study are core-shell particles made of an iron oxide (magnetite or maghemite) cores being coated by polymers or organic acids. Both non-labeled fluidMAG and fluorescence-labeled nano-screenMAG-G particles were purchased from chemicell AG, Berlin, Germany, whereby the lipophilic fluorescent dye was located between the iron oxide core and the polymer coating. In contrast, both SEON particles were friendly provided by Prof. Dr. med. Christoph Alexiou from the Universitätsklinikum Erlangen, Germany. Their synthesis was carried out as described previously [133–135].

As nanoparticles' physicochemical properties decisively influence their reactivity and interaction with biological structures, a detailed characterization was performed on all particles used in this study. To this end, both particle size and surface charge were determined by means of dynamic light scattering and zeta size measurements, whereas vibrating sample magnetometry was used for analyzing magnetic properties regarding concentration determinations (see section 2.1.2). Detailed information on all used SPIONs is shown in table 2.1. In order to analyze the protein corona formation on particle surfaces in more detail gel electrophoresis-based protein separation was performed on corona-comprising particles (see section 2.1.1). Thereby the formation of a protein corona was experimentally induced through incubation of 15 mg magnetic particles within 2.0 ml FCS—if necessary diluted with RPMI 1640 medium—at 37 °C

Table 2.1: Characteristics of experimentally used SPIONs. BSA - bovine serum albumin; DEAE - diethylamine ethyl; PAM - polyacrylat-co-maleat; PEI - polyethylenimine; PdI - polydispersion index.

Name	**Coating**	**Hydrodyn. Size (PdI)**	**ζ-potential**
fluidMAG-D	starch	141 nm (0.108)	-11±7 mV
nano-screenMAG-G/D	starch, fluorochrom (476/490 nm)	139 nm (0.171)	-10±4 mV
fluidMAG-DEAE	strach/ DEAE	132 nm (0.098)	+36±7 mV
fluidMAG-PEI	PEI, 750 kDa	157 nm (0.113)	+47±7 mV
nano-screenMAG-G/PEI	PEI, 750 kDa, fluorochrom (476/490 nm)	135 nm (0.139)	+54±9 mV
SEON$^{\mathrm{BSA}}$	lauric acid/ BSA	157 nm (0.241)	-19±4 mV
SEON$^{\mathrm{PAM}}$	PAM	151 nm (0.297)	-54±1 mV

for 10 min. Upon magnetic separation SPIONs were washed once with 1.0 ml *aqua bidest.* and magnetically separated again before they were resuspended within 1.0 ml *aqua bidest.*. Particles were stored at 4 °C until usage.

2.1.1 SDS-PAGE and Silver Staining

The qualitative and semi-quantitative analyses of the protein corona were evaluated by means of sodium dodecyl sulfate polyacrylamide gel electrophoresis (SDS-PAGE) as described earlier [136]. In short, secondary and tertiary structure of proteins were reduced by applying reducing agent and cracked by heating up to 95 °C for 5 min, followed by a separation of the denatured proteins by molecular weight with PAGE. As references, a molecular weight standard protein collection Kaleidoscope marker (Bio-Rad Laboratories, Hercules USA) and analogously treated FCS solutions were carried along. Next, protein bands were stained by highly sensitive silver staining with SilverXpress Silver Staining Kit (Thermo Fisher Scientific, Waltham, USA) and gray-scale gel images were analyzed for optical densities using the ImageJ 1.50e software (Wayne Rasband, National Institutes of Health, USA). The transfer of gray-scaled imaged into alternative color maps was performed utilizing the MATLAB® R2013a software (MathWorks, Natick, USA).

2.1.2 Physical SPION Characterization

To determine the hydrodynamic diameter of SPIONs, dynamic light scattering was applied using the Zetasizer nano series ZS (Malvern Instruments, Herrenberg, Germany). Scattered He-Ne laser light (633 nm) detected at 173° during three independent measurements with twelve replicates each was used to determine intensity-weighted hydrodynamic diameters. Additionally, zeta potentials were measured using the same instrument but based on laser Doppler velocimetry. By measuring the magnetic properties of the prepared samples by means of vibrating sample magnetometry particle concentrations were determined. This was realized by using the PMC MicroMag 3900 VSM (Lakeshore Cytotronics Inc., Westerville, USA) in the vibrating sample magnetometry mode.

2.2 Cell Culture

Cell culture preparations and respective solutions were handled under laminar flow hoods. Equipment was autoclaved, sterilized by rapidly-acting ethanol-based wipe disinfection or filtration by using 0.2 µm pore size membrane filters. If not stated otherwise all cells were cultured at 37°C in a water-saturated atmosphere supplemented with 5% CO_2.

2.2.1 Cell Lines

As a representative *in vitro* model an established cell line of human brain microvascular endothelial cells (HBMEC) was used. This adherent blood-brain barrier-representing cell line originally isolated from cortical capillaries has been immortalized by introduction of the SV40 large T antigen [137]. HBMEC were kindly provided by Prof. Dr. rer. nat. Werner Reichardt from the Ernst-Abbe-Hochschule Jena.

Likewise adherent, MCF-7 (DSMZ no. ACC 115) cells constitute an epithelial cell line derived from the pleural effusion of a female patient with a mammary gland adenocarcinoma. Monocytic THP-1 (DSMZ no. ACC 16) and promyeloblastic HL-60 (DSMZ no. ACC 3) are suspension cell lines both derived from peripheral blood of patients affected with acute monocytic or acute myeloid leukemia, respectively. THP-1, HL-60 as well as MCF-7 cell lines were purchased from the Leibniz Institute DSMZ - German Collection of Microorganisms and Cell Cultures, Braunschweig, Germany.

2.2.2 Cell Cultivation

HBMEC, THP-1, and HL-60 were cultivated using RPMI 1640 cell culture medium supplemented with 10% (v/v) FCS whereas for MCF-7 cells DMEM medium provided with 10% (v/v) FCS was used. Every three to four days subconfluent HBMEC and MCF-7 were trypsinized using 0.05% trypsin-EDTA and subcultured at a ratio between 1:5 and 1:12 with fresh cell culture medium. Every three to four days the suspension cells THP-1 and HL-60 were passaged at a ratio of 1:3 with fresh cell culture medium. In regular intervals cell cultures were tested regarding mycoplasmic contaminations using the commercial PCR-based Venor™ Gem mycoplasma detection kit (Sigma-Aldrich Chemie GmbH, Steinheim, Germany).

2.2.3 Transwell-Based Generation of *in vitro* Blood-Brain Barrier Model

In order to generate the *in vitro* BBB model sub-confluent HBMEC were harvested and resuspended in seeding medium being composed of RPMI 1640 supplied with 10% (v/v) FCS, 100 U/ml penicillin, and 0.1 mg/ml streptomycin. After 30-minute equilibration of 24-well transwell inserts within seeding medium, equilibration medium was removed and per insert 100 µl containing 240,000 cells were added into the insert (= apical membrane site/donor compartment). Subsequently, the cell-equipped transwell inserts were carefully placed into 24-well companion plates filled with 600 µl/well seeding medium (= basolateral site/acceptor compartment). When the effect of different cell culture media and media supplements was investigated, 24 h after seeding the seeding medium was replaced by respective cell culture medium. Depleted cell culture medium was renewed every other day. Cellular growth and cell layer integrity were verified regularly by means of transendothelial electrical resistance (TEER) measurements (see section 2.4.1).

For transmigration experiments of SPION-loaded THP-1 or HL-60 cells through the BBB model, 240,000 cells HBMEC were seeded analogously on 24-well FluoroBlok transwell inserts, whereas apical seeding medium volumes and basolateral volumes were adjusted to 300 µl and 1000 µl, respectively.

2.2.4 Preparation of Astrocyte-Conditioned Medium

In a monoculture-based BBB-representing cell culture system astrocyte conditioned medium (ACM) might be favorable in order to enhance the integrity of the biological barrier [132]. In order to evaluate its effect in the here presented transwell system ACM was obtained from primary astrocytes isolated from the spinal cord of mouse E13 embryos. Cultivated on 24 well plates using DMEM/Ham's F-12 medium supplemented with 10% (v/v) FCS, 100 U/ml penicillin, and 0.1 mg/ml streptomycin medium was collected every four days. Before use it was centrifuged (10 min at 1,000 rcf), sterile filtered (0.2 µm pore size), and stored at 4 °C.

2.2.5 Differentiation of Progenitor Cells

For the analysis of SPION-induced migration of immune cells across the HBMEC-based *in vitro* BBB model, established progenitor cell lines were chemically stimulated to induce differentiation. As described earlier, 1.4% (v/v) DMSO dissolved in RPMI 1640 cell culture medium containing 10% (v/v) FCS was used to stimulate the differentiation of HL-60 to neutrophilic-like cells [138–140]. Every other day 1/3 of medium was replaced by fresh medium supplemented with 1.4% (v/v) DMSO. Analogously, as stated by Park *et al.* [141] monocytic differentiation of THP-1 was induced by incubation with 5 ng/ml PMA dissolved in RPMI 1640 cell culture medium with 10% (v/v) FCS for five days. Every other day 1/3 of medium was replaced by fresh PMA-containing medium. Differentiated cells were either characterized by flow cytometric analysis upon immunological staining (see section 2.7.2) or Pappenheim staining (see section 2.5.2). Moreover, the adherent fraction of differentiated THP-1 and the suspended fraction of HL-60 cells were subjected to transmigration assays (see section 2.9).

2.3 Cell Viability Assays

Different assays were used in order to verify cellular viability of HBMEC after exposure to diverse types of SPIONs. While acute cytotoxicity for SPION incubations of up to 24 h was investigated using biochemical and flow cytometry-based assays (see sections 2.3.1 and 2.3.2), SPION-associated long-term effects on cell viability were analyzed by means of real-time cell analysis using the xCELLigence system (see section 2.3.3).

2.3.1 PrestoBlue™ Assay

The PrestoBlue™ assay is a biochemical test designed to determine the amount of viable cells based on their metabolic activity. Thereby the PrestoBlue™ reagent resembles non-fluorescent resazurin which in the presence of the reducing environment present within living cells is reduced to the highly fluorescent resofurin. As this dye conversion is proportional to the number of metabolically active cells it can be utilized for cell viability quantification.

In order to test the SPION-specific cytotoxic effect on HBMEC, per well of a 96-well black-walled µ-Clear® plate 15,000 cells resuspended within RPMI 1640 cell culture medium supplied with 10% (v/v) FCS —and if necessary 100 U/ml penicillin and 0.1 mg/ml streptomycin—were seeded in triplicates. Upon cultivation over night, SPIONs dispersed within 18 µl *aqua bidest.* were added resulting in final concentrations of 5–100 µg/cm^2 (corresponding to 19–378 µg/ml) and incubated for 3 h or 24 h. For approaches analyzing the protein corona-related effect on particle cytotoxicity, cell culture medium was removed and cells were carefully washed twice by using D-PBS before fresh serum-free RPMI 1640 cell culture medium and 18 µl SPIONs were added per well. Positive and negative controls were always obtained by adding 18 µl *aqua bidest.* only or 0.1% triton X-100 to cell-seeded wells, respectively. Additionally, cell-free wells containing cell culture medium and 18 µl respective SPION formulations were carried along as background controls.

According to the manufacturer's protocol PrestoBlue™ reagent supplied as a 10× solution was added into each well and incubated at 37 °C for 30–60 min before emitted fluorescence at 600 nm (10–40 nm bandwidth) upon excitation with 545 nm (20 nm bandwidth) was detected using the CLARIOstar microplate reader (BMG LABTECH GmbH, Orthenberg, Germany).

2.3.2 SYTOX® Red Dead Cell Staining

The principle of the SYTOX® Dead Cell Staining is based on the inability of a high affinity, nucleic acid-intercalating fluorescent dye to pass intact cell membranes whereas cells with compromised plasma membranes are easily penetrated. Thus, damaged and dead cells can be identified by bright fluorescence signals and can be distinguished from non-stained vital cells.

Samples were prepared as specified in section 2.7.1. Pelleted cells were resuspended within 500 µl of 2.5 nM SYTOX® Red (diluted in PE buffer) and incubated at 4 °C for 15 min. Pure SPION solutions were stained analogously in order to verify both non-specific interactions between particles and dye and the spectral overlap of fluorescent-labeled SPIONs into the SYTOX® Red channel. Additionally, these only-SPION-containing samples were utilized for setting up gates excluding free particles from data acquisition during flow cytometric analysis. Without washing, at least 10,000 cellular events/sample were analyzed by the use of FACS CALIBUR (BD Bioscience, Singapore) with SYTOX® Red staining detected with a 661/16 nm bandpass filter upon excitation with 633 nm and fluorescent-labeled SPIONs detected with a 585/42 nm bandpass filter upon excitation with 488 nm.

2.3.3 Real-Time Cell Analysis

The real-time cell analysis via the xCELLigence DP (Omni Life Science GmbH & Co. KG, Bremen, Germany) presents a non-invasive approach for monitoring cellular proliferation, size, morphology, and attachment. The principle of this method is based on impedance measurements, where adherent cells seeded on gold electrodes integrated into the bottom of multiwell plates act as insulators in response to an applied voltage of about 20 mV. As the measured impedance in each well is influenced by electrode geometry, ion concentration, and attachment of cells onto the surface, increasing numbers of vital, adhering cells are accompanied with elevated impedance measurements. *Vice versa*, decreasing impedance values indicate cell shrinkage and cellular detachment from the surface and are associated with cytotoxic events. Thus, this method was used in order to analyze the dynamic effects of SPIONs on cell proliferation and viability especially for long-term incubations. at

HBMEC resuspended within RPMI 1640 medium supplied with 2% or 10% (v/v) FCS—and if necessary 100 U/ml penicillin and 0.1 mg/ml streptomycin—were seeded into 16-well E plates in duplicates. The real-time cell analysis was started and following 24 h (log phase with exponential cell growth) or 48 h (stationary phase with equilibrium of proliferation- and death rate) cultivation SPIONs dispersed within 10 µl *aqua bisdest.* were added resulting in final concentrations of 25–100 µg/cm^2 (corresponding to 25–100 µg/ml). Alternatively, negative control cells were incubated with 10 µl *aqua bidest.* only whereas cell-free wells containing cell culture medium were treated with respective SPION solutions as background controls. Cell index progression was monitored for further 72 h.

2.4 Analysis of the Cell Layer Integrity

The cell layer integrity of HBMEC seeded on transwell membranes resembles a critical aspect in verifying the *in vitro* BBB model's condition and quality. While repetitive TEER measurements were used in order to monitor the progression of this tightness parameter in vital cell cultures, end-point determinations such as molecular permeability assays or microscopic analysis of fixed cells with subsequent fluorescent staining (see section 2.6) or histological cross sections (see section 2.4.3) were used to get a more complete insight into the cell layer functionality and composition.

2.4.1 Transendothelial Electrical Resistance Measurements

For continuously verifying the tightness of a cellular barrier measuring the transendothelial electrical resistance (TEER) is a well-established method and vitally important for the evaluation of *in vitro* BBB models [129]. As permeability barriers restrict the movement of ions through the cell layer, an increased TEER indicates an *in vitro* barrier of elevated tightness.

By using chopstick electrodes connected to an epithelial voltohmmeter, the TEER of HBMEC layers cultivated as described in section 2.2.3 were determined. Thus, per insert the mean of three TEER measurements determined at three different positions was aligned to the effective membrane area (*i.e.*, 0.33 cm^2 membrane area including pores). Further, reference TEER measurements of cell-free membrane inserts with respective cell culture media served as background resistances and were subtracted from sample values.

2.4.2 Molecular Permeability Assay

The determination of paracellular permeability of cellular barriers was performed using sodium fluorescein (NaFl, 376 Da). As NaFl is small, freely diffusible, and non-toxic this fluorescent molecule is frequently utilized as a highly sensitive paracellular tracer for both *in vitro* and *in vivo* studies [129,142].

HBMEC-cultivated inserts as specified in section 2.2.3 were incubated with 100 µl of 2.5 µM NaFl diluted within phenol red-free RPMI 1640 medium, 10% (v/v) FCS, 100 U/ml penicillin, and 0.1 mg/ml streptomycin at the apical site, whereas companion plates at the basolateral site were filled with 600 µl phenol red-free RPMI 1640 medium supplied with 10% (v/v) FCS, 100 U/ml penicillin, and 0.1 mg/ml streptomycin. The NaFl-exposed inserts were incubated at 37 °C under orbital shaking (90 rpm, 30 mm amplitude) for 10–60 min whereby at defined time points, inserts including incubation medium were transfered to a new well containing 600 µl of fresh phenol red-free RPMI 1640 medium with 10% (v/v) FCS, 100 U/ml penicillin, and 0.1 mg/ml streptomycin and incubation was continued as stated above. Fluorescence intensities of samples obtained from basolateral medium upon 10-, 30-, and 60-minute incubation were transferred into black-walled 96-well µ-Clear® plates in triplicates and measured by using the CLARIOstar microplate reader (λ_{ex} = 460/9 nm, λ_{em} = 515/20 nm). NaFl permeability coefficients P_{NaFl} were calculated from applied and detected concentrations (c in nM) and volumes (V in cm^3) as described by Audus and Borchardt [143] according to the following equation:

$$P_{NaFl} = \frac{c_{acceptor} \cdot V_{acceptor}}{t \cdot A \cdot c_{donor}}$$

with t and A defining the incubation time (s) and the effective diffusion area (cm^2), respectively. Alternatively, NaFl restraints were calculated from NaFl permeability coefficients as ratio of cell-free and cell-grown inserts membranes.

Table 2.2: Dehydration steps performed by the automatic tissue processor. RT - room temperature.

No. of cycles	Reagent	Reaction conditions
2	70% ethanol	1 h, RT
2	96% ethanol	1 h, RT
3	100% ethanol	1 h, RT
1	100% ethanol : 100% xylene (1:1)	1 h, RT
2	100% xylene	1 h, RT
2	paraffin	1 h, 70 °C

2.4.3 Histological Analysis of Cross Sections

In order to gain an insight into the structural integrity and condition of the transwell-grown HBMEC layers (see section 2.2.3) inserts were washed twice using D-PBS before they were fixed with 10% formalin solution at room temperature (RT) for 15 min. Membranes were carefully cut out of the insert and embedded perpendicularly into a 1% agarose solution (dissolved in D-PBS) within a truncated 1.5 ml tube. Upon agarose hardening at 4 °C for 10–20 min, the membrane-containing agarose block was removed from the 1.5 ml tube, transferred to embedding cassettes, and stored within 10% formalin solution at RT for 1–2 days. Upon removal of formalin and four *aqua bidest.* washing steps for 15 min each, samples were dehydrated and transferred into paraffin as listed in table 2.2 by using the automatic tissue processor Leica TP1020 (Leica Biosystems Nussloch GmbH, Nussloch, Germany).

Subsequently, paraffined samples were embedded into paraffin using a Leica EG1160 embedding center (Leica Biosystems) before sections of 15 µm were generated from pre-cooled sample-paraffin blocks by means of the Leica RM 2165 automated rotary microtome (Leica Biosystems). Microtomic cross sections were spread with the help of a 5-minute incubation within a 40 °C-water bath. Next, they were applied to microscopic slides and dried over night at 37 °C.

For microscopic analysis the cross sections were de-paraffined and hydrated by incubating the samples in xylene followed by a decreasing alcoholic series as summarized in table 2.3. In order to visualize SPIONs within the samples a

Table 2.3: Paraffin removal and hydration or dehydration steps performed during staining of histological cross sections by descending and ascending alcoholic series, respectively.

Descending alcoholic series		**Ascending alcoholic series**	
Condition	Reagent	Condition	Reagent
2x10 min	100% xylene	1x30 s	50% ethanol
2x5 min	100% ethanol	1x30 s	70% ethanol
1x2 min	96% ethanol	1x30 s	96% ethanol
1x2 min	70% ethanol	1x30 s	100% ethanol
1x2 min	50% ethanol	1x120 s	100% xylene

Prussian blue staining using a 2% (w/v) potassium ferrocyanide solution was performed as described in section 2.5.1. Next, samples were rinsed twice with *aqua bidest.* and cell nuclei counterstained by a 10-minute incubation with Nuclear Fast Red solution at 37 °C. Excessive staining solution was removed and samples were rinsed using running tab water for 1 min before undertaking a dehydrating, ascending alcoholic series followed by an incubation within xylene (see table 2.3) and embedding with water-free mounting medium.

2.5 Cellular Staining

In order to evaluate cellular conditions such as morphology, viability, integrity, differentiation, and subcellular localization of specific proteins or SPIONs, diverse cellular staining procedures were applied followed by microscopic analysis. Thus, Prussian blue staining was used to visualize the interaction of non-labeled SPIONs with cells by light microscopy, whereas fluorescence staining of cells and specific subcellular structures was made use of for analyzing localizations of fluorescence-labeled SPIONs during fluorescence microscopy. Additionally, by means of confocal laser scanning microscopy a detailed insight into the spatial distribution of the labeled objects within the cell was achieved.

2.5.1 Prussian Blue Staining

Prussian blue resembles a dark blue pigment generated by the iron chelating reaction of ferrocyanides. Thus, the staining is commonly used to visualize ferric iron within biological samples, such as iron-based nanoparticles within cellular environments.

In order to stain SPIONs in cellular samples a protocol adapted from Schlorf *et al.* [144] was used. In detail, samples fixed by incubation with 10% formalin solution for 15 min were permeabilized by a 10-minute incubation in 0.1% triton X-100 (dissolved in D-PBS) and washed twice with D-PBS. Next, a freshly prepared solution of 2% (w/v) potassium ferrocyanide dissolved in 1 M hydrochloric acid was applied and incubated at 37 °C for 10 min before two washing steps using D-PBS were carried out. Unless otherwise stated, cells were counterstained by sample incubation with the eosin Y-containing DiffQuick II solution for 30 s. As the resulting cytoplasmic red staining was not stable, microscopic images were acquired immediately. Alternatively, cells were counterstained using Nuclear Fast Red solution and subtracted to a dehydrating alcoholic series as described in section 2.4.3 in order to achieve a stable dyeing.

2.5.2 Pappenheim Staining

The Pappenheim staining combines both May-Grünwald- and Giemsa staining and resembles the method of choice for panoptic staining of blood smears in hematology.

In this context, the Pappenheim staining was applied for evaluating the differentiation of both THP-1 and HL-60 cells to monocytic and neutrophilic appearance, respectively. Initially, smear preparations of THP-1 and HL-60 cells differentiated as described in section 2.2.5 and resuspended within FCS (approx. 500.000 cells/30 µl) were generated and air-dried for 30–60 min. The Pappenheim staining was performed with the automatic stainer SP-10 (Sysmex Deutschland GmbH, Norderstedt, Germany). Briefly, samples were treated with May-Grünwald solution (1:2 diluted with D-PBS) for 4 min. Upon a D-PBS-based rinsing, Giemsa solution (1:6 diluted with D-PBS, filtered upon dilution) was added and incubated for 15 min. Again, samples were washed using *aqua bidest.* and air-dried without mounting with coverslips before they were viewed microscopically.

2.6 Fluorescent Staining for Confocal Laser Scanning Microscopy

Confocal laser scanning microscopy upon (immuno-)fluorescence staining offers the possibility to specifically view distinct cellular structures and their three-dimensional distribution. The spatial pinhole allows the acquisition of signals from the confocal plain only, thus eliminating out-of-focus light. On the one hand cytoskeletal staining was used for the sake of studying both the cell integrity and the cellular uptake of fluorescence labeled SPIONs. On the other hand the expression and distribution of the tight junction protein ZO-1 upon immunofluorescence staining was additionally used in order to assess the tightness of transwell-cultured HBMEC layers (see section 2.4). Furthermore, transmigration of THP-1 or HL-60 cells through HBMEC layers was also verified by laser scanning microscopy (see section 2.9). For all approaches the confocal laser scanning microscope LSM 510 META and the appendant software ZEN 2009 6.0 SP2 (both Carl Zeiss Microscopy GmbH, Jena, Germany) were used.

2.6.1 Phalloidin Staining

Phalloidin is a bicyclic heptapeptide strongly binding filamentous actin (F-actin) preventing its depolymerization. Labeled with a fluorescent tag this molecular dye is prevalently used for the visualization of F-actin *in vitro*.

For the investigation of the uptake mechanism of SPIONs into HBMEC, 200,000 cells resuspended in RPMI 1640 cell culture medium with 10% (v/v) FCS were seeded on glass cover slips which had been flamed and placed into 24-well plates. Upon cell cultivation over night, endocytosis inhibitors were added as indicated and pre-incubated for 60 min before 50 µg/cm^2 (corresponding to 100 µg/ml) nano-screenMAG-G/D were applied and incubated for 3 h. Samples were washed three times with D-PBS before they were fixed at RT by applying a 10% formalin solution for 15 min. Next, formalin was removed by another three washing steps with D-PBS and cells were permeabilized by a 10-minute treatment with 0.1% triton X-100 (diluted with D-PBS). Samples were incubated with the D-PBS-based staining solution containing 19 ng/ml Alexa Fluor® 633 Phalloidin (Invitrogen) and either 10 ng/ml DAPI I (Abbot Laboratories) or 12 µg/ml Hoechst 33258 (Invitrogen). Afterwards, cells were washed with D-PBS again and analyzed microscopically without embedding. Cells were scanned layer by layer with a constant slice distance of 1 µm each resulting in z-stacked images of 10-18 slices. Acquired image stacks were quantitatively analyzed using MATLAB® R2013a software (MathWorks, Natick, USA) where the amount of internalized SPIONs was calculated from overlapping signals derived from the cytoskeletal F-actin and the SPION channels. Actin channels were binarized using the threshold algorithm as described by N. Otsu [145], multiplied with original SPION channels, and integrated to total SPION intensities per image slice. For comparability of multiple microscopic field views containing divergent numbers of cells, particle amounts were normalized to the cell-representing F-actin signal.

For transwell-cultured HBMEC layers which had been cultivated and incubated with fluorescence labeled SPIONs analogously as described in sections 2.2.3 and 2.8 F-actin was stained as stated above. However, as the transwell membrane interfered with the nuclear staining by DAPI, Hoechst 33258 counterstain was used in order to visualize cell nuclei in this case. Moreover, upon staining cell-layered membranes were cut out off retainers and embedded on glass slides using water-based mounting medium prior to microscopic analysis.

2.6.2 Immunofluorescence Staining of *zonula occludens*-1

As peripherally located ZO-1 functions as a scaffold of the transmembrane tight junction proteins and the F-actin cytoskeleton, it is an integral component of the tight junction complex [146]. That is why its immunostaining is prevalently used in order to verify the paracellular permeability of cellular barriers.

To this end, samples cultivated as described in section 2.2.3 were fixed and permeabilized as specified above (see section 2.6.1). Next, non-specific epitopes were blocked by incubating the samples with 5% BSA (dissolved in 0.1% triton X-100) before the primary rabbit α-ZO-1 antibody (1:200 diluted with 1% BSA dissolved in 0.1% triton X-100) was applied and incubated at 37 °C for 60 min. The samples were washed twice using D-PBS and the staining solution containing the secondary antibody (see table 2.4) was added for 60 min (37 °C). Moreover, samples stained without primary antibodies and samples not stained with primary nor secondary antibodies were carried along and served as controls for specific secondary antibody binding and autofluorescence, respectively.

Table 2.4: Composition of the secondary antibody solution for immunofluorescence *zonula occludens* (ZO-1) staining diluted in D-PBS. BSA - bovine serum albumin.

Final Concentration	Component
4 µg/ml	goat α-rabbit antibody
19 ng/ml	Alexa Fluor® 633 Phalloidin
12 µg/ml	Hoechst 33258
50 µg/ml	BSA

Upon staining samples were washed with D-PBS, membranes were cut out off retainers and embedded on glass slides using water-based mounting medium prior to microscopic analysis.

2.7 Flow Cytometry

Flow cytometry is a powerful technology facilitating the rapid analysis of thousands of cells on a single-cell level. Thereby, various physical parameters including relative size and relative granularity can be measured and analyzed simultaneously. The principle of this approach is based on a fluid stream carrying suspended cells to a laser intercept from which both incident scatter light and emitted fluorescence signals can be detected. According to cellular size and internal complexity both forward and sideward scatters are influenced, respectively. Additionally, fluorescence labels can be measured resulting in relative fluorescence intensities.

This method was used in order to analyze cell viabilities upon SYTOX® Red Dead Cell Staining as specified in section 2.3.2. Flow cytometric analysis was also used to investigate the interaction of fluorescence labeled SPIONs with HBMEC (see section 2.7.1) and the differentiation analysis of progenitor immune cells (see section 2.7.2). For all analyses the FACS CALIBUR (BD Bioscience, Singapore) was used. Per sample at least 10,000 cellular events were recorded and analyzed via the FlowJo® software (FLOWJO, LLC, Ashland, USA).

2.7.1 Flow Cytometry-Based Particle-Cell Interaction

For the purpose of investigating the interaction of fluorescence labeled SPIONs with HBMEC and its correlation to cell viability, 80,000 cells/cm^2 resuspended within RPMI 1640 cell culture medium with 10% (v/v) FCS—and if necessary 100 U/ml penicillin and 0.1 mg/ml streptomycin—were seeded into 12-well plates in duplicates. Following over-night-culture, cells were incubated with fluorescent-labeled SPIONs dispersed within 100 µl *aqua bidest.* resulting in final concentrations of 25 µg/cm^2 or 50 µg/cm^2 (corresponding to 94.5 µg/ml or 189 µg/ml) for up to 24 h. For approaches analyzing the protein corona-related effect on particle cytotoxicity, cell culture medium was removed and cells were carefully washed twice by using D-PBS before fresh serum-free RPMI 1640 cell culture medium and 100 µl SPION solution were added per well. Negative controls were treated analogously using 100 µl *aqua bidest.* only. After incubation time was completed, sample cell culture media were collected and cells harvested using HyQ®Tase™. Next, cells were spun down by a 5-minute centrifugation step at 300 rcf (4 °C), washed with ice-cold PE buffer, and centrifuged as mentioned before. For investigating the correlation between SPION interaction with cells and cytotoxicity, cell pellets were additionally treated with SYTOX® dead cell staining and directly analyzed as described in section 2.3.2. Otherwise cell pellets were fixed using 10% formalin for 15 min, washed using ice-cold PE buffer and resuspended in 500 µl PE buffer again. Finally, per samples at least 10,000 cellular events were analyzed by flow cytometry, where cellular loading with fluorescence labeled SPIONs was detected with a 585/42 nm bandpass filter upon excitation with 488 nm. Additionally, cell-free samples containing SPIONs only were utilized for setting up gates, excluding free particles from data acquisition during flow cytometric analysis.

2.7.2 Surface Marker Expression of Differentiated Cells

In order to verify the differentiation of both THP-1 and HL-60 cells to monocytic and neutrophilic phenotypes respectively, the expression of characteristic surface markers was analyzed by means of flow cytometry. To this end, cells differentiated as described in section 2.2.5 were harvested, whereby for THP-1 HyQ®Tase™ was applied. Approximately 500,000 cells were spun down by a 5-minute centrifugation step at 300 rcf, washed twice with PE buffer, and

Table 2.5: Composition of the antibody mixture for characterizing monocytic or neutrophilic surface markers. APC - allophycocyanin; CD - cluster of differentiation; FITC - fluorescein isothiocyanate; PE - phycoerythrin; PE (buffer) - D-PBS supplemented with EDTA (2 mM).

Neutrophilic phenotype (HL-60)		**Monocytic phenotype (THP-1)**	
Volume	Component	Volume	Component
10 µl	CD13-FITC	10 µl	CD34-FITC
10 µl	CD16-PE	10 µl	CD40-PE
10 µl	CD11b-APC	10 µl	CD14-APC
70 µl	PE buffer	10 µl	PE buffer

centrifuged as mentioned previously. Cell pellets were resuspended in 100 µl of respective antibody solutions (see table 2.5). After a 20-minute incubation time at RT, 3 ml PE buffer were added and cells were centrifuged again (5 min, 300 rcf). Cells were resuspended in 300 µl PE buffer and measured at the FACS CALIBUR whereby FITC- and PE labels were detected with a 530/30 nm and a 585/42 nm bandpass filter upon excitation with 488 nm. In contrast for APC labels the excitation with 633 nm was used in combination with an emission bandpass filter of 661/16 nm. Moreover, non-stained cell samples and single-stained compensation beads served as autofluorescence controls and references for compensating fluorochrome spill over to other channels, respectively.

2.8 Detection and Quantification of SPIONs

For studying the passage of SPIONs through HBMEC layers complete basolateral acceptor compartments were analyzed for the presence of SPIONs either by magnetic particle- or atomic absorption spectroscopy. Both approaches resemble highly sensitive methods of quantifying superparamagnetic or elementary iron, respectively.

For the experimental investigations HBMEC were plated out on transwell membranes as specified in section 2.2.3. After five days of cultivation, barrier tightness was confirmed by means of TEER measurements (see section 2.4.1). If indicated, one day prior to the particle incubation MCF-7 cells with a density of 350,000 cells/well were seeded into 24 well plates and cultivated over night. On the day of incubation experiment HBMEC-grown inserts were transferred to implied MCF-7-grown or cell-free 24 well companion plates each containing 600 µl RPMI 1640 medium supplemented with 10% (v/v) FCS, 100 U/ml penicillin, and 0.1 mg/ml streptomycin. Unless stated otherwise, 100 µg/cm^2 SPIONs dissolved within 165 µl (equal to 200 µg/ml) RPMI 1640 medium supplemented with 10% FCS (v/v), 100 U/ml penicillin, and 0.1 mg/ml streptomycin were added. For the first 30 min, particle incubation was carried out on top of a block magnet (210 mT at 3 mm distance, field gradient 6.8 T/m) in order to bring the particles in close proximity to the cell layer localized on the transwell membrane. Thereafter, the incubation was continued without the magnet until indicated incubation time was complete. In order to precisely quantify the amount of SPIONs in the respective compartments, samples were analyzed by magnetic particle spectroscopy and atomic absorption spectroscopy as described in sections 2.8.1 and 2.8.2. Additionally, HBMEC layer integrity upon SPION exposure was verified as specified in section 2.4 as well as by microscopic analysis upon fluorescence staining (see section 2.6).

2.8.1 Magnetic Particle Spectroscopy

Magnetic particle spectroscopy (MPS) represents a sensitive magnetic detection method that allows for the quantification of the superparamagnetic nanoparticle iron content without being affected by biological components such as cells or suspension medium [147–149]. It is based on the nonlinear magnetic susceptibility response of magnetic nanoparticles exposed to an oscillating magnetic field. Thus, odd harmonics of magnetic moments A_i of the detected time-dependent signal are Fourier transformed yielding the MPS spectrum. As the SPION-specific amplitude signal is proportional to the applied SPION amounts, MPS provides the opportunity to precisely determine SPION contents of biological samples [150].

For the quantification of SPIONs within the distinct compartments of the transwell system, samples were processed as described by Gräfe *et al.* [151]. Briefly, complete apical donor and basolateral acceptor compartment media were collected upon incubation time. By avoiding the application of any metallic materials during preparations porous membranes including cellular layers were cut off retainers and homogenized within 800 µl *aqua bidest.* by using a ceramic scalpel and the gentleMACS™ dissociator. Finally, sample volumes were reduced to 20–50 µl by centrifugal vacuum concentration using the SpeedVac™

SPD111 (Thermo Fisher Scientific Inc., Waltham, USA) at 100 g and 40 °C) before MPS spectra were measured using a commercial MPS device (Brucker Biospin, Rheinstetten, Germany) operating at an oscillating magnetic field B_{drive} of 25 mT and a frequency f_0 of 25 kHz. The third harmonic A_3 of the MPS spectrum was used for iron quantification by normalization to the corresponding $A_{3,ref}$ of a reference sample of known iron amount. In turn, reference sample's iron amount was cross-validated by photometry (510 nm) upon phenantroline staining by dissolving in hydrochloric acid, reduction by hydroxylamine, and addition of 1,10-phenantroline monohydrate. Furthermore, A_5/A_3 were recorded in order to verify the magnetic behavior including particle agglomeration. Analogous samples without the addition of SPIONs served as background controls from which the limit of detection (LOD) was calculated according to:

$$LOD = \overline{X}_{background} + 3 \cdot STDV_{background}$$

where $\overline{X}$ and $STDV$ represent mean and standard deviation of background measurements according to McNaught and Wilkinson [152].

2.8.2 Atomic Absorption Spectroscopy

In addition to the quantitative estimation of SPIONs via MPS, atomic absorption spectroscopy (AAS) was applied in order to verify the SPIONs' interaction with and passage through HBMEC layers based on the spectroanalytical detection of elementary iron. Thus, iron concentrations of analyzed samples were determined upon measuring the absorbance at the characteristic and highly sensitive wavelength of 248.3 nm.

To this end, complete media of both donor and acceptor compartments were collected and SPIONs were pelleted by centrifugation at 20,000 g for 45 min Upon discarding excessive supernatant, 25 µl of the sediment-containing solution were dissolved in 162.5 µl of 32% HCl. In contrast, MCF-7 cells seeded into bottom wells of 24-well companion plates as well as cut outs of HBMEC-containing transwell membranes were directly dissolved in 187.5 µl of 32% HCl. Samples were supplemented with 62.5 µl of 10% TCA and incubated for 5 min at RT before precipitated proteins and debris were removed by a 5-minute centrifugation at 3,600 g. Finally, supernatants were transfered into conic AAS tubes and iron contents analyzed by using the AAS-5 FL supplied by Analytik

Jena AG, Jena, Germany. The LOD was calculated as described above (see section 2.8.1).

2.9 Transmigration through Blood-Brain Barrier Model

The transmigratory kinetics of differentiated neutrophilic HL-60 and monocytic THP-1 cells (see section 2.2.5) both being labeled by a fluorescent dye were investigated by the dynamic fluorescence-based detection of transmigrated cells via a microplate reader. Additionally, migratory effects were verified by end-point fluorescence microscopy of fixed and Hoechst 33258-counterstained FluoroBlok membranes (see section 2.6.1) as well as Prussian blue staining combined with the treatment of Nuclear Fast Red (see section 2.5.1) upon spinning of acceptor compartment-obtained cells on microscopic slides by using the Cytospin Rotofix at 35 rcf for 5 min).

For the generation of a HBMEC layer on FluoroBlok inserts, HBMEC were seeded and cultivated as described in section 2.2.3 for five days. By the application of 10 µM CellTracker™ red CMTPX (diluted in RPMI 1640 cell culture medium) at 37 °C for 30 min, HBMEC were pre-stained prior to the transmigration assay. For 120 min indicated cell layers were exposed to inflammatory stimuli based on the addition of 5 ng/ml IL-1β into both the apical donor- and basolateral acceptor compartment containing RPMI 1640 medium supplied with 10% (v/v) FCS, 100 U/ml penicillin, and 0.1 mg/ml streptomycin.

In parallel to the preparation of HBMEC layers differentiated HL-60 and THP-1 cells were harvested and pre-labeled by a 30-minute staining with 10 µM CellTracker™ Green BODIPY® diluted within RPMI 1640 cell culture medium at 37 °C. Upon a 5-minute centrifugation at 300 rcf cells were resuspended in RPMI 1640 medium supplied with 10% (v/v) FCS and 1.4% DMSO or 5 ng/ml PMA in case of HL-60 or THP-1 cells, respectively, and plated into 6- or 12-well plates according to a cell density of approx. 680,000 cells/cm^2. Cells were allowed to settle for 30 min before they were incubated with 50 µg/cm^2 (corresponding to 189 µg/ml) SPIONs for 120 min. Next, suspension HL-60 cells were centrifugation with 200 rcf for 5 min. In contrast, adherent THP-1 cells incubation medium was removed by aspiration and cells were harvested as described above. Next, pelleted HL-60 and THP-1 cells were resuspended in RPMI 1640 medium supplied with 0.1% BSA, 100 U/ml penicillin, 0.1 mg/ml streptomycin, and 1.4% DMSO or 5 ng/ml PMA, respectively, resulting in a concentration of 500,000 HL-60/300µl or 300,000 THP-1/300µl. Upon the transfer of 300 µl cell suspension to HBMEC-seeded or cell-free FluoroBlok inserts each supplied with 1,000 µl corresponding medium within the basolateral acceptor compartment, cells were allowed to settle down for further 30 min. With HL-60 or THP-1-assembled inserts were carefully transferred to companion plates equipped with RPMI 1640 medium, 0.1% BSA, 100 U/ml penicillin, 0.1 mg/ml streptomycin, and 1.4% DMSO or 5 ng/ml PMA, respectively. If necessary, media were additionally supplemented with chemoattractants (10 nM fMLP for HL-60 or 100 ng/ml MCP-1 for THP-1) and/or 5 ng/ml IL-1β. Where applicable inserts were incubated on top af a MagnetoFACTOR 24-well plate (310 mT at 2 mm distance, field gradient 38.4 T/m) for 30 min before transmigration was monitored using the CLARIOstar microplate for at least 1,400 min with an excitation of λ_{ex} = 490/15 nm and detection at λ_{em} = 535/20 nm where the temperature was kept at 37 °C and CO_2 at 5%.).

2.10 Statistical Analyses

Data of repetitive independent experiments with multiple replicates each are presented as weighted mean ± (weighted) standard deviation. Statistical significance tests were performed using the Prism 6 (GraphPad Software, La Jolla, USA) applying a one- or two-way analysis of variance (ANOVA) with 95% confidence intervals followed by a multiple comparison test and correction according to Dunnett [153, 154], Tukey [155], or Sidak [156]. Differences are considered as statistically significant for $p < 0.05$ (*), $p < 0.01$(**), $p < 0.001$ (***), or $p < 0.0001$(****).

CHAPTER 3

Results

SPIONs are highly attractive candidates for various biomedical applications such as hyperthermia anti-tumor therapies, as drug delivery systems, and as contrast agents for magnetic-based imaging. The wide range of possibilities for SPION design regarding tuning in size, shape, and coating material as well as additional surface functionalization led to a huge diversity of SPION types. By now, several SPION-related products are already medically approved and occasionally used in clinical settings. However, this particle diversity results in major challenges, as the functionalities of specific SPIONs have to be verified in context of biological effects within the whole organism they are applied to. A detailed understanding of how such particles interact with cells and whether or how they penetrate biological barriers is crucial for their safe, targeted, and effective biomedical implementation. Therefore, in this study, the human cell line HBMEC was utilized for initial testing of diverse types of SPIONs for cytotoxic effects. Furthermore, SPION-specific particle binding to the cells and uptake into the cells were investigated in detail. In order to analyze the particle passage through a biological barrier, an HBMEC-based *in vitro* model simulating the human blood-brain barrier (BBB) was established and optimized in a next step. Using this transwell barrier system, SPION-induced effects on the barrier integrity and the particle passage through the cellular layer were studied in detail. Finally, the SPION-mediated passage of cells as well as the cell-mediated particle delivery across the BBB model were investigated in order to give a comprehensive insight into how SPIONs affect and cross such biological barriers.

3.1 Interaction of SPIONs with HBMEC

Investigations were performed in order to gain an insight into the general consequences of various types of SPIONs on both the cellular interaction and cell viability of HBMEC. On the one hand, the effect of diverse particle coatings comprising different particle surface charges were tested regarding their biological effects. Based on these initial experiments, particle types suitable for subsequent barrier passaging experiments were identified. On the other hand, the effect of the protein corona formed on the particle surface and its influence on biocompatibility and cellular interaction were investigated, analogously.

3.1.1 SPION-associated Effect on Cell Viability

The acute cytotoxic effects of SPION exposure of HBMEC for 3 h and 24 h was tested using the PrestoBlue™ assay. Results are shown in figure 3.1. For concentrations of up to 100 µg/cm^2 no noticeable effect on HBMECs' viability can be observed after 3 h or 24 h incubation with neutral fluidMAG-D and anionic SEON^{BSA} particles resulting in a relative cell viability of 90.0±2.5% and 79.7±1.9% after 24 h incubation with respective SPIONs. The exposure of HBMEC to up to 100 µg/cm^2 of cationic fluidMAG-DEAE for 24 h induced a slight concentration-dependent reduction in cellular viability to 67.1±4.2% compared to controls. Likewise cationic PEI-coated SPIONs strongly impede cell viabilities as incubations of 100 µg/cm^2 for 3 h and 24 h trigger a relative decrease to 49.4±3.6% and 13.1±1.7%, respectively.

3.1.2 Binding of SPIONs to Cells and Particle Uptake

Cellular binding and uptake of SPIONs are closely connected with cytotoxicity. Whereas highly-interactive particle types are usually associated with cytotoxic effects, biocompatible particles are often characterized by lower cellular affinities. In order to study these aspects for selected SPIONs, both Prussian blue staining and flow cytometry were applied. Figure 3.2 shows microscopic images of HBMEC incubated with indicated SPIONs and reveals that within a 3-hour incubation the cellular binding of neutral fluidMAG-D particles is low. In contrast, cells exposed to anionic SEON^{BSA}, cationic DEAE- and PEI-coated

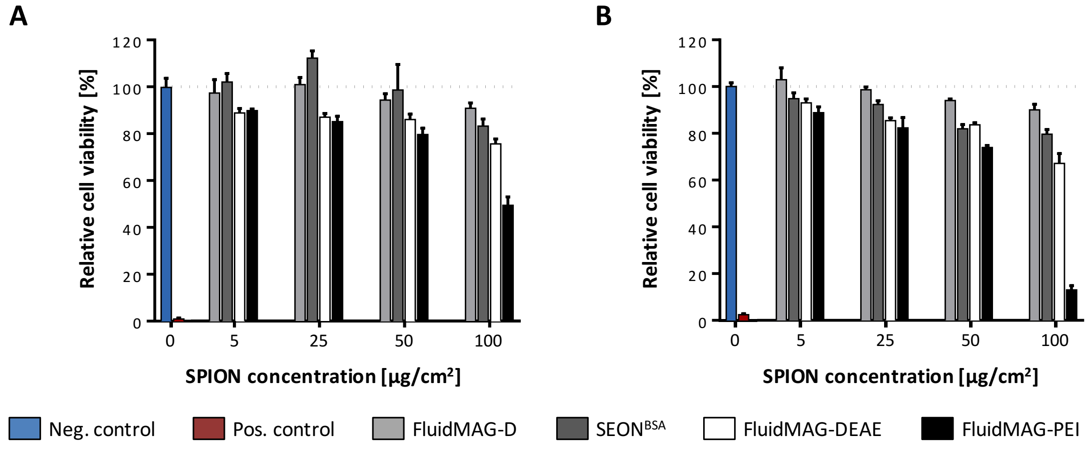

Figure 3.1: PrestoBlue™ cell viability assays of HBMEC exposed to diverse types of SPIONs. HBMEC seeded into 96-well plates in triplicates with a seeding density of 15,000 cells/well were exposed to indicated SPION types in final concentrations of 5–100 µg/cm^2 (corresponding to 19–378 µg/ml). Negative and positive control cells were treated with *aqua bidest.* or 0.02% triton X-100 final concentration. Upon incubation for 3 h (**A**) and 24 h (**B**) PrestoBlue™ assays were performed. Shown are weighted means ± standard deviation of two to four independent experiments.

SPIONs show a strong Prussian blue stain with the highest intensity for the latter. After 24 h the extensive Prussian blue staining of fluidMAG-D-incubated HBMEC reveals an enhanced cellular binding of these neutral particles compared to exposures for 3 h. Similarly, anionic SEON^{BSA} and cationic fluidMAG-DEAE and -PEI show a pronounced particle adherence as indicated by the more intense staining pattern upon 24 h. In all cases the particles seem to form clusters, whereby fluidMAG-PEI are again most notable.

In order to monitor the temporal progress of cellular SPION loading in context of quantity, flow cytometry of HBMEC exposed to fluorescence-labeled SPIONs was performed. Panels B and C of figure 3.2 give an overview of the results obtained for the—according to the Prussian blue staining—low-affinity starch-coated and high-affinity PEI-coated particles. HBMEC incubated with neutral nano-screenMAG-G/D show low fluorescence upon incubation for 5 min (11±1 RFU), which gradually increases during incubation for 30 min and 180 min with cellular fluorescences of 37±4 RFU and 228±22 RFU, respectively. Additional to cellular fluorescence labeling, side scatters (SSC) were recorded in order to monitor SPION loading via this granularity-representing parameter. However, for nano-screenMAG-G/D incubation for up to 180 min, the

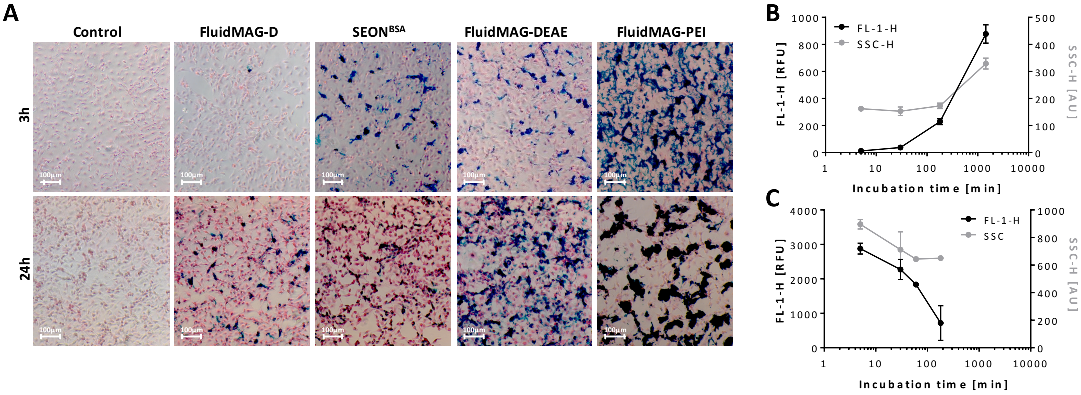

Figure 3.2: Cellular interaction of diverse types of SPIONs with HBMEC. A HBMEC seeded into 24-well plates with seeding densities of 165,000 cells/cm^2 were incubated with 50 µg/cm^2 (corresponding to 60 µg/ml) for 3 h and 24 h. SPIONs were stained by Prussian blue. HBMEC (pink) were counterstained with eosin Y-containing DiffQuick II solution. **B-C** HBMEC seeded into 12-well plates in duplicate with seeding densities of 80,000 cells/cm^2 were incubated with 50 µg/cm^2 (corresponding to 189 µg/ml) fluorescence-labeled nano-screenMAG-G/D (B) or nano-screenMAG-G/PEI (C) for 5 min to 24 h. Supernatant and harvested cells were fixed and analyzed by flow cytometry with 10,000 cellular events per sample. Shown are means ± standard deviation of one representative of two independent experiments. AU - arbitrary unit; FL-1-H - SPION-labeled fluorescence intensity; RFU - relative fluorescence units; SSC-H - side scatter intensity.

SSC shows only minor changes to 173±10 AU compared to control cells with 162±11 AU. After particle incubation for 24 h both the cellular fluorescence loading and the SSC strongly expand to 877±68 RFU and 329±20 AU, respectively. In contrast, cationic fluidMAG-PEI show the highest cellular labeling affinities of 2878±156 RFU immediately after particle addition to the cells (5 min) with a gradual decrease during 30 min, 60 min, and 180 min to 2273±291 RFU, 1834±65 RFU, and 719±504 RFU, respectively. Analogously, SSC rapidly increases from 162±11 AU to 896±34 AU upon incubation with nano-screenMAG-G/PEI for 5 min and subsequently decreases to 651±2 AU upon the 180-minute incubation.

Flow cytometry allows the analysis of cellular SPION loadings in a (semi-)quantitative manner. However, it is not possible to gain information of the actual particle uptake into the cells. This is why in the next step confocal laser scanning microscopy was used in order to identify the spatial distribution of fluorescence-labeled SPIONs within fixed, fluorescently stained HBMEC. By specifically blocking endocytotic pathways with diverse inhibitors, the uptake mechanisms for both starch- and PEI-coated SPIONs were investigated in detail. Figure 3.3 summarizes this analysis, whereby the image acquisition layer-by-layer was used to study the co-localization of SPIONs with the intracellular F-actin cytoskeleton within the limits of optical resolution. Based on this premise, internal SPIONs were quantified by integrating the particles' fluorescence intensities of F-actin overlapping signals. During microscopic analysis SPIONs have not been observed co-located with the cell's nucleus. The effects of specific inhibitors on the internalization of neutral fluidMAG-D into HBMEC is presented in panel A. Notably, the SPION uptake into HBMEC is massively compromised by approx. 90% when particle incubation is carried out at 4 °C instead of 37 °C indicating an energy-dependent uptake mechanism for this particle type. Through blocking of caveolin- and clathrin-dependent endocytotic pathways by filipin and chlorpromazine, the amount of internalized starch-coated particles is significantly reduced to 39±10% and 53±34%, respectively. Whereas the single drug treatment of HBMEC with cytochalasin D does not impair particle uptake significantly (61±29%), the combination of this F-actin depolymerizing substance with chlorpromazine efficiently decreases the SPION internalization by 82%. In contrast, the reduction of the incubation temperature from 37 °C to 4 °C does not impair the presence if internalized nano-screenMAG-G/PEI into HBMEC as relative SPION internalization is 100±3% and 114±17%, respectively (see figure 3.3 panel B).

3.1.3 Protein Corona-associated Effects on Cytotoxicity and SPION Interaction with Cells

The large surface-to-volume ratio of SPIONs evokes a high reactivity leading to an intensive interaction with their environment. Based on that, immediately after the contact of such particles with biological fluids a protein corona is formed, providing the SPIONs with a new biological identity. In order to investigate the magnitude of this effect, cationic PEI-coated particles were used. To achieve various levels of surface protein coronas, PEI particles were incubated in dilutions of specific FCS concentrations and analyzed for both cytotoxicity, cellular interaction, and uptake mechanisms. Thereby, serum-free or serum-reduced conditions for cell cultivation and -incubations were used in order to not influence the particles' protein corona additionally.

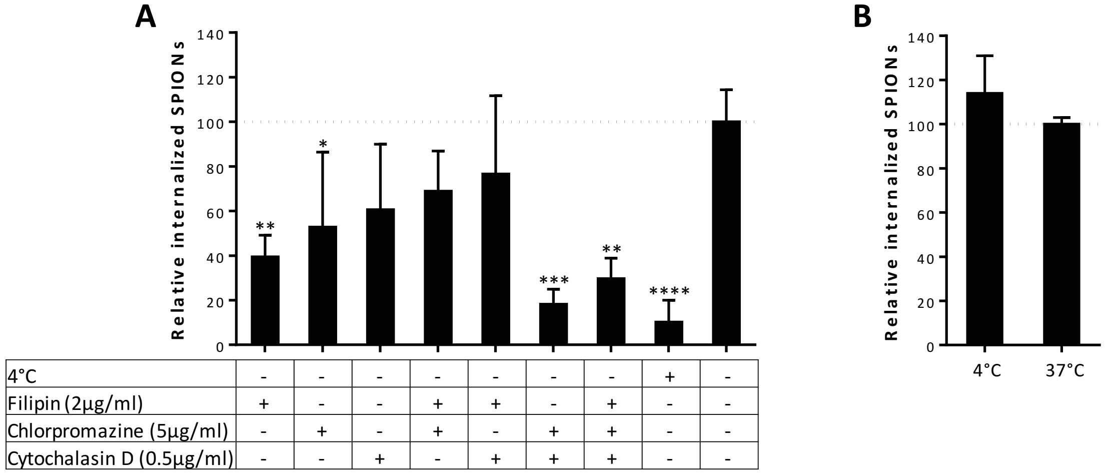

4°C	-	-	-	-	-	-	-	+	-
Filipin (2µg/ml)	+	-	-	+	+	-	+	-	-
Chlorpromazine (5µg/ml)	-	+	-	+	-	+	+	-	-
Cytochalasin D (0.5µg/ml)	-	-	+	-	+	+	+	-	-

Figure 3.3: Cellular uptake mechanisms of SPIONs analyzed by confocal laser scanning microscopy. HBMEC were seeded on glass cover slips placed within 24-well plates with a seeding density of 165,000 cells/cm^2. After pre-incubation of cells with indicated inhibitors for 60 min nano-screenMAG-G/D or -G/PEI were added resulting in a final concentration of 50 µg/cm^2 (corresponding to 60 µg/ml) and incubated for 3 h. Cells were fixed, permeabilized and stained with DAPI and Alexa Fluor® 633 Phalloidin. Internalized SPIONs were identified by SPION-derived fluorescence overlapping with cells′ actin-derived signals. **A** Quantitative analysis of internalized nano-screenMAG-G/D into HBMEC subjected to indicated incubation conditions. **B** Quantitative analysis of internalized nano-screenMAG-G/PEI into HBMEC subjected to indicated incubation conditions. Shown are means ± standard deviation of two independent experiments with three microscopic fields of view each. Statistical significance of indicated samples compared to controls was tested by one-way ANOVA followed by Dunnett′s multiple comparison, where differences are considered as statistically significant for $p < 0.05$ (*), $p < 0.01$(**), $p < 0.001$ (***), and $p < 0.0001$(****).

Figure 3.4 demonstrates the immediate concentration-dependent cytotoxic effect related to respective amounts of protein corona in panel A. The presented data reveal that cell viability of HBMEC exposed to 100 µg/cm^2 of the original corona-free fluidMAG-PEI particles is reduced to 36±9% compared to negative control cells, whereas a comprehensive protein corona in PEI particles (100% FCS) preserves cell viability at 84±8%. Remarkably, the gradual elevation of protein corona contents on the particles′ surface is associated with increasing cell viability. Additionally, long-term analysis of cytotoxic effects of SPIONs shown in panel B show cell indices of HBMEC exposed to corona-free fluidMAG-PEI continuously reduced by more than 83±4% for up to 96 h. Contrary, HBMECs′ indices continue on a stable level of 100–105% for up to 72 h before slightly decreasing to 85±10%, 96 h after the addition of PEI particles pre-incubated in FCS.

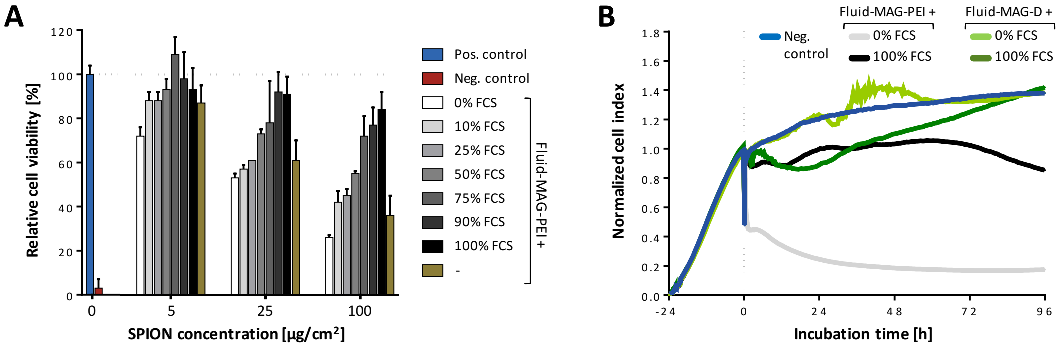

Figure 3.4: Acute and long-term cell viability studies of HBMEC exposed to SPIONs with varying levels of protein corona. **A** HBMEC seeded into 96-well plates in triplicates with a seeding density of 15,000 cells/well were subjected to serum-free conditions. FluidMAG-PEI particles pre-incubated within indicated concentrations of FCS (diluted in RPMI medium) were added resulting in final concentrations of 5–100 µg/cm^2 (corresponding to 19–378 µg/ml). Negative and positive control cells were treated with *aqua bidest.* or 0.02% triton X-100 final concentration. Upon incubation for 3 h, PrestoBlue™ assays were performed. Shown are means ± standard deviation of one representative from four independent experiments. **B** HBMEC were seeded into 16-well plates in duplicates under serum-reduced conditions (*i.e.*,, RPMI supplemented with 2% (v/v) FCS) with a seeding density of 10,000 cells/well. At time point 0 (dotted vertical line) fluidMAG-PEI or -D pre-incubated within indicated FCS concentrations (diluted with RPMI medium) were added resulting in final concentrations of 100 µg/cm^2 (corresponding to 100 µg/ml). Negative control cells were treated with *aqua bidest.*. Shown are means of one representative of three independent experiments.

In order to investigate the protein corona-associated effects on cellular interaction of SPIONs and additionally correlate these findings to cytotoxicity, HBMEC incubated with fluorescence-labeled particles were analyzed by flow cytometry, whereby cells with compromised cell membranes were identified using the SYTOX® Red staining. Figure 3.5 summarizes the time-dependent SPION-associated fluorescence loading of cells according to the protein corona on nanoscreenMAG-G/PEI in panel A, and the relative proportion of indicated populations in panels B–D. Data show for 5-minute incubations that cells are strongly loaded with PEI particles without a protein corona resulting in an intense cellular labeling (465.9±2.1 RFU), whereas the stepwise evolution of a protein corona reduces this cellular labeling gradually to a geometric mean of 33.1±0.2 RFU for 100% FCS. This observation is reflected by the respective cellular positive fraction for SPION-associated fluorescence (SPION$^+$), which is 98.7±4.6% and 55.3±2.5% for 0% FCS and 100% FCS, respectively. Simultaneously, the proportion of cells negatively stained for the SYTOX® Red (SYTOX $^-$) are 23.0±3.2% and 88.6±2.7% for PEI particles without (0% FCS) or with a complete (100%

FCS) protein corona. The cellular fraction being positive for both SPIONs and SYTOX® Red is largest (76.9±3.2%) for particles of 0% FCS and decreases to 8.9±1.7% for PEI particles pre-treated with 100%FCS. Similarly, after a particle exposure of 30 min, cellular SPION-associated fluorescence intensities of cells gradually increase to 472.9±10.6 RFU and 54.2±1.1 RFU for 0% FCS and 100% FCS, respectively. Simultaneously, the SPION$^+$ cell fractions decrease and SYTOX$^-$ increase with elevated protein corona contents. However, after incubation of particles possessing different protein corona contents for 180 min, both cellular SPION load and ratios of SPION$^+$ or SYTOX$^-$ increasingly come into line. Thus, the fractions of SPION$^+$ cells are 97.9±1.9% for protein-free particles and 97.6±2.0% for 100% FCS particles, whereas geometric means of cellular SPION-associated fluorescence are 330.9±33.2 RFU and 218.4±2.8 RFU, respectively. Remarkably, the percentage of cells positive for both SPIONs and SYTOX® Red strongly decreases to 21.4±1.5% for PEI particles pre-incubated in 0% FCS and slightly increases to 11.8±1.3% for PEI particles possessing a complete protein corona (100% FCS).

In addition to general flow cytometry-based interaction studies, particle-incubated cells were analyzed for internalized SPIONs by confocal laser scanning microscopy, too. The results shown in figure 3.6 demonstrate that for an incubation of 5 min only low particle amounts between 0.087±0.030 (0% FCS) and 0.050±0.06 (100% FCS) relative to the cellular area are detected intracellularly. Extending the incubation time to 30 min strongly increases the intracellular particle signals especially for non-corona particles (0% FCS) to 0.358±0.010 whereas the stepwise protein corona induction significantly and gradually reduces the relative internal SPIONs amounting in lower values of 0.123±0.005 for PEI particles pre-incubated in 100% FCS. For particle incubations of 180 min the relative amount of internalized SPIONs pre-incubated in 100% FCS increases to 0.349±0.080 and slightly decreases in case of PEI particles without protein corona (0.280±0.010). However, values do not significantly differ from one another.

As analyses of cellular particle interaction and uptake by flow cytometry and confocal laser scanning microscopy revealed a pronounced dependence on the level of protein corona on PEI-coated SPIONs, the corona-associated influence on uptake mechanisms itself was investigated next. In order to analyze the energy-dependence of this process, nano-screenMAG-G/PEI with no (0% FCS) or a complete (100% FCS) protein corona were added to HBMEC under serum-free conditions and a 180-minute incubation was carried out at either 37 °C or 4 °C (see figure 3.7). Subsequent analyses by flow cytometry presented in panels A-C indicate that the cellular particle-associated fluorescence loading for corona-free particles is 330.9±33.2 RFU for 37 °C and 489.0±4.3 RFU for 4 °C, and thus even slightly increases rather than decreases upon temperature reduction. In contrast, energy deprivation during cellular incubation with protein corona-possessing PEI particles strongly reduces this SPION-associated fluorescence from 218.4±2.8 RFU (37 °C) to 88.5±3.9 RFU (4 °C). Analogously, the cellular fraction negative for SYTOX® Red (SYTOX$^-$) is significantly higher for HBMEC exposed to corona-containing particles (87.7±7.6%) compared to corona-free particles (69.3±11.4%) for an incubation temperature of 4 °C, whereas the fraction positive for both SPIONs and SYTOX® Red significantly increases from 8.7±4.6% (100% FCS) to 45.7±18.3% (0% FCS). Further microscopic studies focused on the detection of intracellular SPIONs, reflect similar situation (see figure 3.7 panels D-E). Data demonstrate that for an incubation temperature of 37 °C the amount of internalized SPIONs relative to the cell area is on similar levels for both particle formulations, whereas the SPION incubation at 4 °C significantly reduces this amount from 0.337±0.009% to 0.081±0.030% for PEI particles without or with protein corona, respectively.

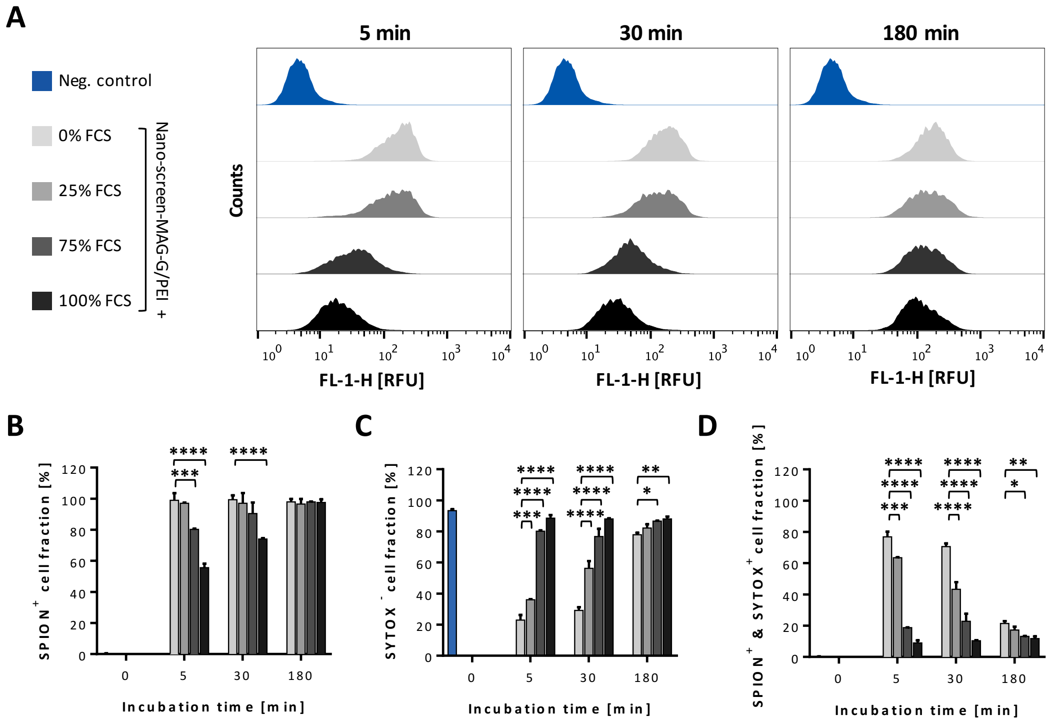

Figure 3.5: Cellular interaction of SPIONs and cell viability of HBMEC upon exposure, analyzed by flow cytometry. HBMEC seeded into 12-well plates in duplicates with seeding densities of 80,000 cells/cm^2 were subjected to serum-free conditions. Nano-screenMAG-G/PEI particles pre-incubated within indicated concentrations of FCS (diluted in RPMI medium) were added, resulting in final concentrations of 25 µg/cm^2 (corresponding to 94.5 µg/ml). After 5–180 min supernatant and harvested cells were stained with SYTOX® Red and analyzed by flow cytometry with 10,000 cellular events per sample. Presented are histograms of cellular SPION-associated fluorescence loading (**A**) or indicated cell fractions (**B-D**). Shown are means ± standard deviation of one representative of two independent experiments. Statistical significance of grouped samples compared among each other was tested by two-way ANOVA followed by Dunnett's multiple comparison, where differences are considered as statistically significant for $p < 0.05$ (*), $p < 0.01$(**), $p < 0.001$ (***), and $p < 0.0001$(****). FCS - fetal calf serum; FL-1-H - SPION-labeled fluorescence intensity; RFU- relative fluorescence units.

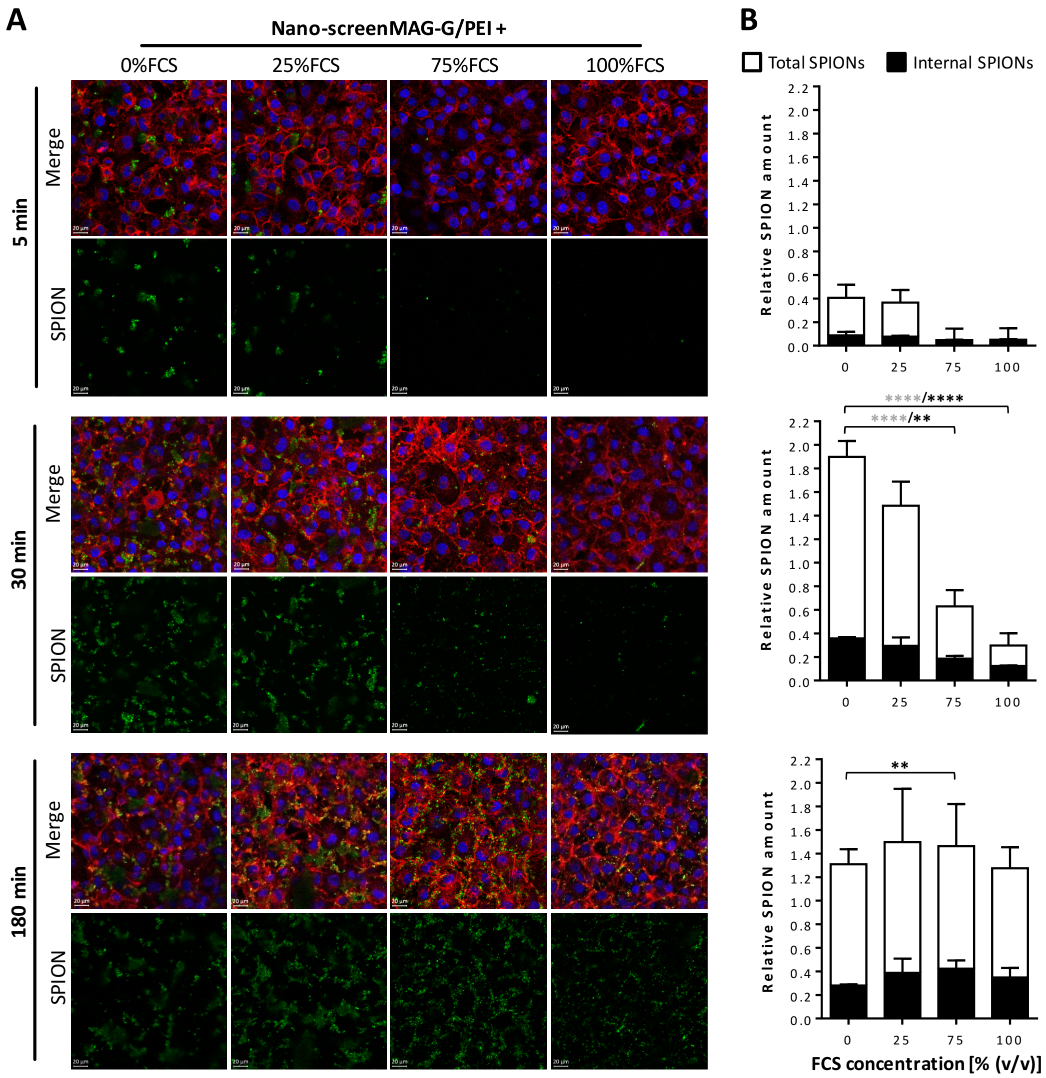

Figure 3.6: Protein corona-associated uptake of SPIONs into HBMEC analyzed by confocal laser scanning microscopy. HBMEC seeded on glass cover slips placed into 24-well plates with a seeding density of 165,000 cells/cm^2 were subjected to serum-free conditions. Nano-screenMAG-G/PEI particles (green) pre-incubated with indicated concentrations of FCS (diluted in RPMI medium) were added resulting in final concentrations of 25 µg/cm^2 (corresponding to 50 µg/ml) and incubated for 5–180 min. Cells were fixed, permeabilized and stained with DAPI (blue) and Alexa Fluor® 633 Phalloidin (red). **A** Microscopic images of SPIONs alone or merged with other channels. **B** Quantitative analysis of internalized nano-screenMAG-G/PEI into HBMEC dependent on the protein corona on SPIONs' surface. Shown are means ± standard deviation of two independent experiments with two to three microscopic fields of view each. Statistical significance among grouped samples was tested by two-way ANOVA followed by Dunnett's multiple comparison, where differences are considered as statistically significant for $p < 0.01$(**) and $p < 0.0001$(****). Levels of statistical significance are indicated for total SPIONs in gray and for internal SPIONs in black. Figure taken with permission and data extended from [157]. FCS - fetal calf serum.

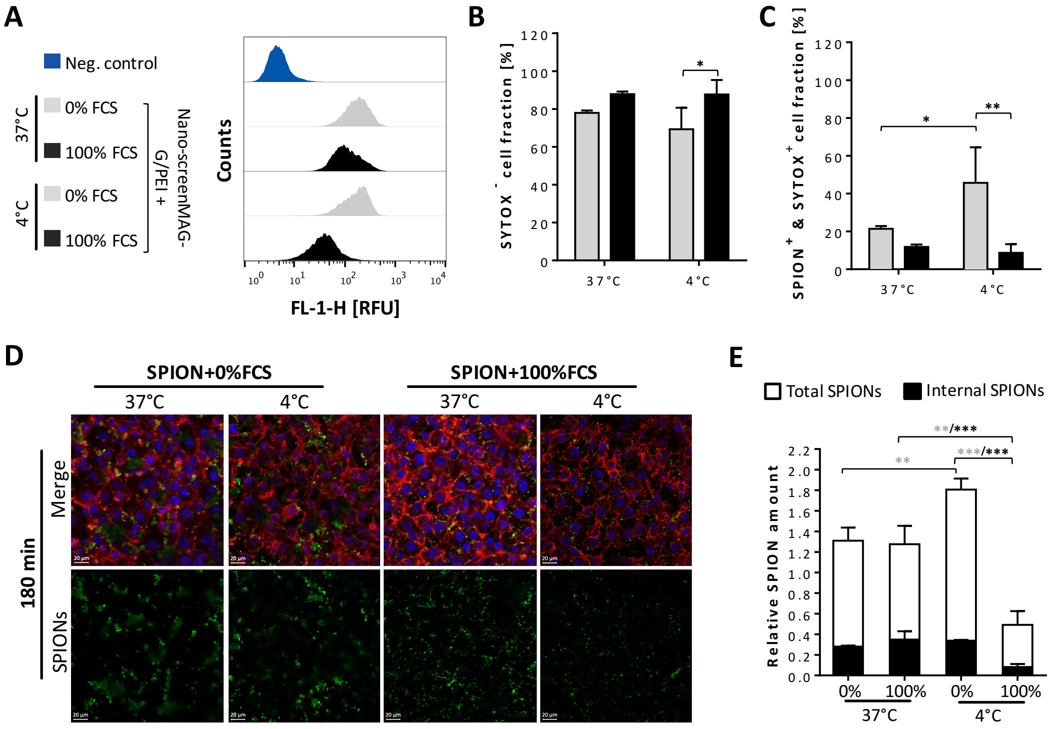

Figure 3.7: Effect of the protein corona on cellular SPION uptake mechanisms analyzed by flow cytometry and confocal laser scanning microscopy. HBMEC were seeded into 12-well plates (A-C) or to cover slips placed within 24-well plates with seeding densities of 80,000 cells/cm^2 or 165,000 cells/cm^2, respectively. Cells were subjected to serum-free conditions and nano-screenMAG-G/PEI particles pre-incubated with indicated concentrations of FCS (diluted in RPMI medium) were added, resulting in final concentrations of 25 µg/cm^2 (corresponding to 94.5 µg/ml or 50 µg/ml). **A-C** After 180 min supernatant and harvested cells were stained with SYTOX® Red and analyzed by flow cytometry with 10,000 cellular events per sample. Presented are histograms of cellular SPION-associated fluorescence loading (**A**) or indicated cell fractions (**B-C**). Shown are means ± standard deviation of two independent experiments. **D-E** Cells were fixed, permeabilized and stained with DAPI (blue) and Alexa Fluor® 633 Phalloidin (red). **D** Microscopic images of SPIONs alone or merged with other channels. **E** Quantitative analysis of internalized nano-screenMAG-G/PEI into HBMEC dependent on the protein corona on SPIONs' surface. Shown are means ± standard deviation of two independent experiments with three microscopic fields of view each. Statistical significance among grouped samples was tested by two-way ANOVA followed by Sidak's multiple comparison, where differences are considered as statistically significant for $p < 0.05$ (*), $p < 0.01$(**) and $p < 0.001$ (***). Levels of statistical significance are indicated for total SPIONs in gray and for internal SPIONs in black. FCS - fetal calf serum; FL-1-H - SPION-labeled fluorescence intensity; RFU- relative fluorescence units.

3.2 Establishing and Optimizing the Blood-Brain Barrier Model

In order to obtain a BBB-representing *in vitro* test model the human cell line HBMEC was utilized. Thereby, transwell inserts comprising a porous membrane were used for generating HBMEC layers separating the upper donor compartment from the lower acceptor compartment. As the barrier integrity is a critical factor for all further investigations regarding particle interaction and passage through the barrier cells, initial experiments revealing optimal cell culture conditions were performed.

3.2.1 Testing of Transwell System and Cell Seeding Density

Different types of membranes and additional coatings for transwell inserts are available for the generation of a cellular transwell barrier system. Testing collagen-coated PTFE- and tissue culture-treated PET membranes each seeded with cell numbers of 160,000–300,000 cells/insert, indicates distinct differences between the two transwell types (figure 3.8). While cells seeded on PTFE membranes can easily be imaged by bright field microscopy, the optically visible pores of PET membranes strongly impede the microscopic evaluation of cellular growth on the latter membrane type. However, investigating the cell barrier integrity regarding TEER revealed that HBMEC seeded on the PET membrane—irrespectively of the cell seeding number—reach higher TEER values compared to HBMEC seeded on PTFE membrane inserts. For instance, seven days after seeding 240,000 cells/insert HBMEC cultivated on PET membranes achieve TEER values of $53{\pm}2\,\Omega\cdot\ \mathrm{cm}^2$ whereas PTFE-cultivated cells remain at $26{\pm}1\,\Omega\cdot\ \mathrm{cm}^2$. Based on these findings PET membrane inserts and a cell seeding number of 240,000 cells/insert were used for all further experiments in order to obtain cellular barriers with appropriate characteristics.

3.2.2 Influence of Cell Media Supplements on HBMEC Layer Integrity

The influence of different cell media and media supplements on HBMEC layers was tested in context of their effect on diverse barrier integrity parameters. Fig.

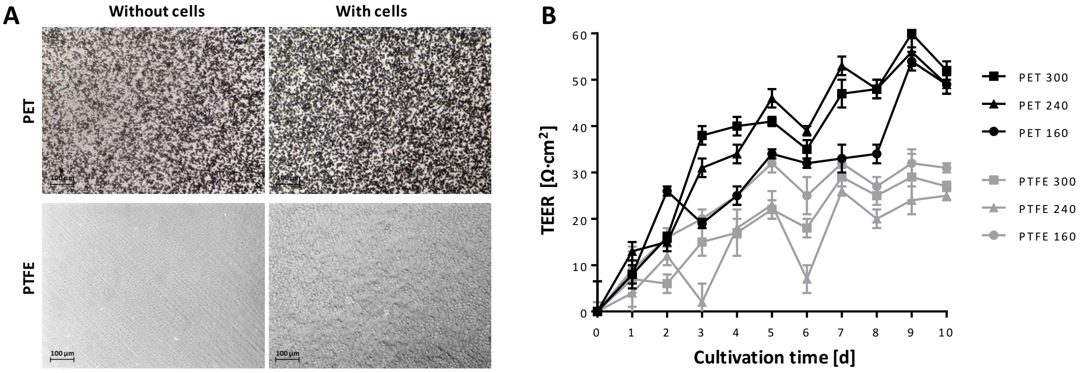

Figure 3.8: *In vitro* blood-brain barrier models formed by HBMEC cultivated on PET or PTFE membrane inserts. HBMEC were seeded and cultivated on collagen-coated PTFE- or tissue culture-treated PET membrane inserts with a cell density of 160,000, 240,000 or 300,000 cells/insert. **A** Microscopic bright field images of blank and cell-seeded membranes. **B** Transendothelial electrical resistance (TEER) measurements of HBMEC layers on respective membrane inserts. Shown are means of two replicate transwell inserts with three measurements each and background correction with cell-free membrane inserts. PET - polyethylene terephthalate; PTFE - polytetrafluoroethylene.

3.9 summarizes the results of these investigations. The Nuclear Fast Red staining of histological cross sections prepared from HBMEC layers cultivated under indicated media conditions (see figure 3.9 panel A) demonstrates that for non-supplemented RPMI medium a loose cell cluster is formed. By using astrocyte-conditioned medium (ACM) a more connected but tenuous cell layer is developed, whereas the addition of 10% (v/v) FCS to ACM seems to strengthen the cellular layer to a more consolidated appearance. However, the cultivation of HBMEC transwell systems with RPMI medium containing 10% (v/v) FCS induces the formation of a dense, continuous, and uniform cell barrier. Both the cytoskeletal and ZO-1 staining of HBMEC layers cultivated under the very same conditions shown in figure 3.9 panel B give similar results, whereby cells cultivated with non-supplemented RPMI appear rounded and sparse in cell-cell contacts without ZO-1 proteins located in the peripheral cell areas. In comparison, ACM-cultivated HBMEC layers seem to be flat and connected intercellularly which is highlighted in particular by the increased presence of ZO-1 at the cell margins. For both RPMI and ACM the addition of 10% (v/v) FCS seems to enhance the three-dimensional assembly of a tight cellular network whereas the peripheral ZO-1 localization is still present but slightly less intense. By repetitive TEER measurements the tightness of developing HBMEC layers was quantified over time (see figure 3.9 panel C). Notably, TEER values strongly increase during the first days after cell seeding and seem to reach a plateau between day five and seven. Whereas on day six non-supplemented RPMI medium results in the lowest TEER values of 24.0±0.7 $\Omega\cdot$ cm^2, plain ACM-treated HBMEC achieve a TEER of 31.9±0.8 $\Omega\cdot$ cm^2. The FCS supplementation of ACM and RPMI elevates the prospective TEER values to 36.4±0.6 $\Omega\cdot$ cm^2 and 46.9±0.7 $\Omega\cdot$ cm^2, respectively. The HBMEC layer's retention to the small molecular dye NaFl was tested as another integrity parameter. Results shown in figure 3.9 panel D indicate that both non-supplemented RPMI and ACM only allow a low barrier tightness with a 12.8±3.4 - and 7.1±0.4 -fold increase of the NaFl retention relative to cell-free transwell inserts after ten-minute incubation with the molecular dye. Again the addition of 10% (v/v) FCS to ACM and RPMI medium showed the most pronounced effects with elevations of the cell layer's molecular retention of 37.0±3.4 - and 31.4±9.2 -fold, respectively.

Taking into account all the results regarding the analysis of the influence of cultivation conditions on barrier integrity, for all further transwell experiments HBMEC layers were prepared by using RPMI medium supplemented with 10% FCS and cultivation for five to six days.

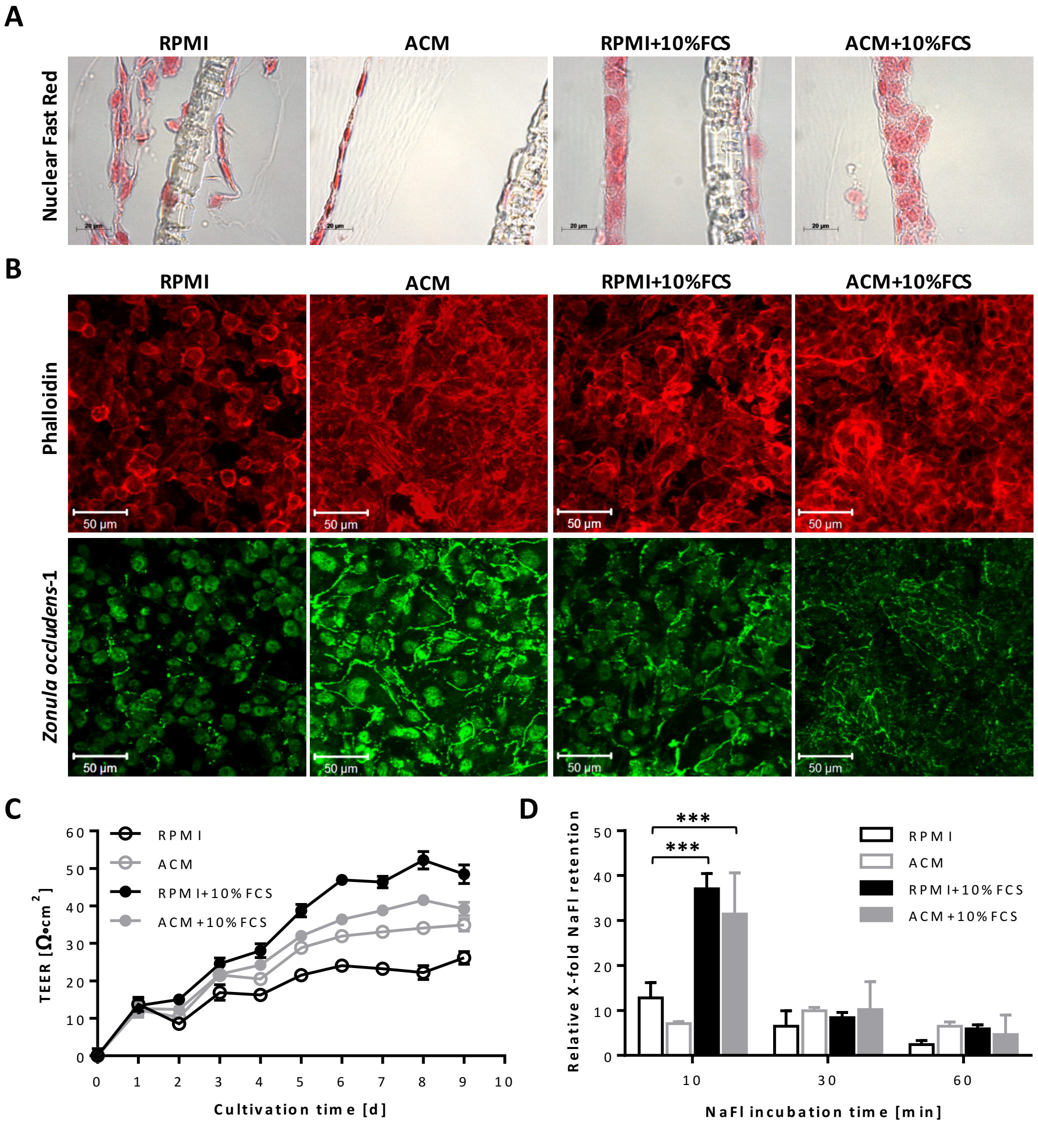

Figure 3.9: Influence of cell culture media and media supplements on barrier integrity parameters. HBMEC were seeded on transwell inserts and cultured for up to nine days. One day after cell seeding media were replaced by indicated fresh media and cultivated further. **A** Nuclear Fast Red-stained histological cross sections of cell layers cultivated under indicated conditions for five days. **B** Fluorescent staining of filamentous actin (red) and *zonula occludens-1* (green) of cell layers cultivated under indicated conditions for six days. **C** Transendothelial electrical resistance (TEER) measurements of HBMEC layers. Shown are means of two replicate transwell inserts with three measurements each and background correction with cell-free membrane inserts. **D** Molecular retention of cell layers to sodium fluorescein (NaFl) upon dye incubation for 10, 30 or 60 min. Shown are means of two replicate transwell inserts cultivated for six days relative to cell-free inserts. Statistical significance among grouped samples was tested by two-way ANOVA followed by Dunnett's multiple comparison, where differences are considered as statistical significant for $p < 0.001$ (***). Parts of the figure taken with permission from [151]. ACM - astrocyte-conditioned medium.

3.3 Interaction of SPIONs with the Blood-Brain Barrier Model

After having established an appropriate *in vitro* BBB model based on an HBMEC-seeded transwell system as described in section 3.2, the system was used for SPION interaction studies. On the one hand, the particles' effects on barrier integrity were tested by various methods in a time-dependent manner in order to gain an insight into the consequences for the barrier itself. On the other hand, SPION passage through the barrier-forming cells was analyzed and quantified in a next step for evaluating the particles' barrier-penetrating ability.

3.3.1 SPION-associated Effects on Barrier Integrity

Maintaining the physiological integrity of the BBB is an essential premise for keeping the brain's homeostasis. In order to investigate consequences of SPION exposure on the HBMEC-based *in vitro* model, TEER measurements before and after incubation with diverse types of SPIONs as well as molecular permeability assays and microscopic analysis of histological cross-sections were performed. Data summarized in figure 3.10 show that SPIONs differently affect the barrier integrity after particle exposure for 180 min. Both TEER measurements and molecular retentions to NaFl shown in panels A and B reveal strong and significant alterations under the influence of cationic fluidMAG-PEI with a decrease of TEER values (relative to initial values) to 0.80±0.03 and NaFl retentions to 0.40±0.02 (relative to control cells). Whereas a slight but significant decrease of TEER values to 0.94±0.01 is observed for fluidMAG-DEAE particles, no influence of these cationic particles is detected by molecular permeability assays based on NaFl. While for exposure of HBMEC layers to fluidMAG-D for 3 h and 24 h, TEER values do not show any significant changes, NaFl retentions are slightly but significantly reduced to 0.79±0.07 and 0.78±0.10, respectively. However, in case of incubation with SEON^{BSA} relative TEER values are significantly reduced to 0.86±0.03, whereas the cell layer's retention towards NaFl elevates the NaFl retention to 1.38±0.08 for three-hour incubations. An incubation of 24 h with these anionic particles is characterized by a strong and significant reduction of both relative TEER values (0.63±0.08) and NaFl retentions (0.41±0.24). Stained histological cross sections of particle-incubated transwell systems shown in panels C-D provide a more comprehensive insight into the cell layers' conditions after particle exposure to neutral fluidMAG-D and anionic SEON^{BSA}. Microscopic images imply that after the incubation with fluidMAG-D, HBMEC layers keep an intact and continuous appearance for incubation times of up to 24 h. In contrast, cross sections of SEON^{BSA}-incubated cells seem already slightly diminished after 3 h and strongly compromised after 24 h, where the layer's continuity is barely visible. Notably, HBMEC layers are not located directly on the transwell membrane, which might be a result of the multi-step sample preparation for this method. Focusing on Prussian blue-stained SPIONs detected within the cross sections it is striking that fluidMAG-D is hardly detectable in samples obtained after an incubation for 3 h but intensively abundant upon a 24-hour incubation. In contrast, cellular layers exposed to SEON^{BSA} show extensive SPION staining as soon as 3 h after particle addition.

3.3.2 Passage of SPIONs through *in vitro* Blood-Brain Barrier Model

As data presented in section 3.3.1 indicate that starch-coated fluidMAG-D minimally affect barrier integrities of HBMEC-based transwell models, the passage of these neutral particles was investigated in detail for incubation times of up to 3 h. To this end, MPS was used for directly detecting and quantifying SPIONs within the distinct compartments of the transwell system with a high sensitivity. Figure 3.11 sums up the experimental data obtained. The particle standard curve presented in panel A implies a close correlation of utilized fluidMAG-D and its detection and quantification via this magnetization response-based method over multiple orders of magnitude ranging from few ng to several hundred µg. Thus, the LOD is as small as 1.85 ng iron for the biological sample. Analyses of compartment-specific contents of SPION-associated magnetic iron shown in panel B demonstrate that with an average of 92.2±1.5% the great majority but not all utilized particles are recovered via this method including sample preparation. Furthermore, data imply that fluidMAG-D is predominantly found within the lower acceptor compartment after a three-hour incubation of cell-free transwell inserts with 100 µg/cm^2 and 200 µg/cm^2, as 83.3±9.4% (14.68±1.66 µg) and 93.1±11.3% (31.46±3.83 µg) of detected SPION-associated iron are found here, respectively. In the presence of HBMEC layers

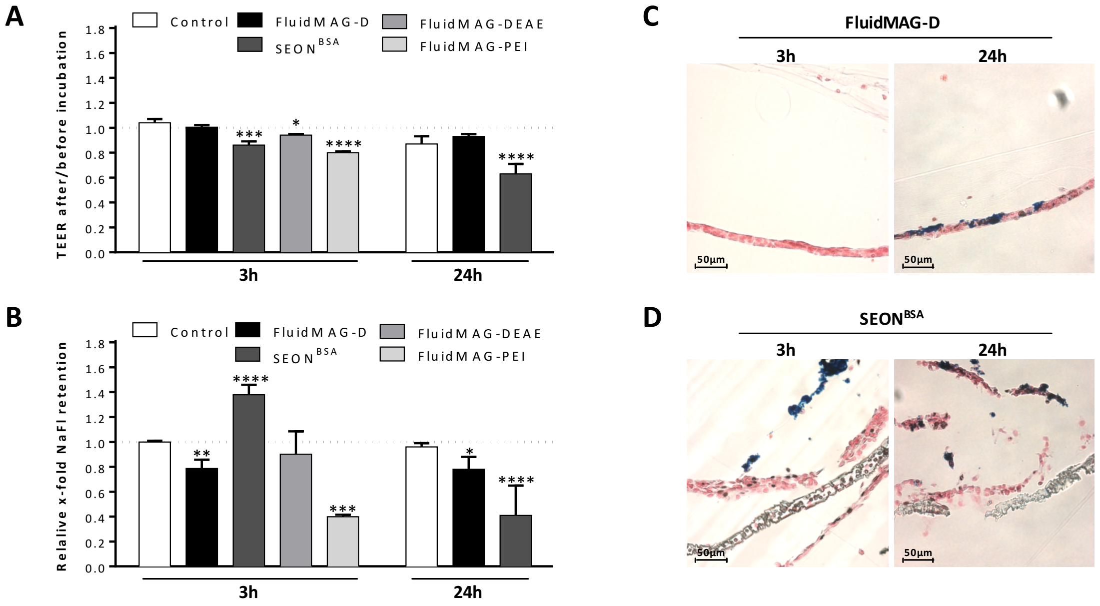

Figure 3.10: SPION-associated effects on barrier integrity parameters of HBMEC layers. HBMEC were seeded on transwell inserts and cultured for five days. Indicated SPIONs were added resulting in a final concentration of 100 µg/cm^2 (corresponding to 200 µg/ml) and incubated for 3 h or 24 h as indicated, whereby the first 30 min were carried out on top of a block magnet. **A** Ratios of transendothelial electrical resistance (TEER) measurements of cell layers before and after SPION incubation. Shown are means of two to four independent experiments with two replicate inserts each. **B** Molecular retention of SPION-incubated cell layers to sodium fluorescein (NaFl). Shown are means of two to four independent experiments with two replicate inserts each. Statistical significance of indicated samples compared to controls was tested by one-way ANOVA for fluidMAG-DEAE and -PEI and two-way ANOVA for fluidMAG-D and SEON^{BSA}. Both cases were followed by Dunnett's multiple comparison, where differences are considered as statistically significant for $p < 0.05$ (*), $p < 0.01$(**), $p < 0.001$ (***), and $p < 0.0001$(****). **C-D** Nuclear Fast Red- and Prussian blue-stained histological cross sections of cell layers incubated with fluidMAG-D (C) or SEON^{BSA} (D) as stated above.

on the transwell membrane most (95.9%-99.3%) of the fluidMAG-D are detected within the upper donor compartment. During the incubation of blank transwell inserts with 100 µg/cm^2 fluidMAG-D, particle amounts recovered within the cell-free membranes are 7.3±5.4 ng, whereas for cell-studded inserts the amount of magnetic iron within this compartment is significantly increased to 112.8±17.4 ng and 371.9±198.4 ng after 0.5 h and 3 h, respectively. A detailed analysis of lower acceptor medium of HBMEC-grown inserts incubated with 100 µg/cm^2 indicate a low (0.7±2.1 ng) amount of magnetic iron after 0.5 h, though below the LOD. However, extending the incubation time to 3 h results in the significant increase of magnetic iron to 5.8±3.0 ng within this compartment. Strikingly, neither for the three-hour incubation with 50 µg/cm^2 nor for 200 µg/cm^2 fluidMAG-D such pronounced increases are detectable (2.2±1.6 ng and 1.6±2.0 ng).

In order to verify the results of particle passage through the *in vitro* barrier model by MPS-based quantification of magnetic iron, AAS was applied, which allows the quantification of total iron. In addition to the detailed analysis of SPION presence within the barrier-forming HBMEC layer and lower acceptor medium, a second cell type located on bottom wells mimicking underlying tissues was applied and analyzed for iron. Furthermore, the passage of fluidMAG-D was compared to that of SEON^{BSA} in a time-dependent manner. Results summarized in figure 3.12 show the standard curve for fluidMAG-D derived from AAS quantification. While the linear correlation of utilized iron and AAS-detected signals are indicated for these particles in panel A, the detection range is limited to a maximum of 3 µg implicating additional dilution steps for quantifications of elevated iron amounts. The LOD of this method is 2 ng. The compartment-specific iron contents shown in panel B indicate again that the highest amounts of fluidMAG-D are found within the lower acceptor compartment and lower cells if cell-free transwell inserts are incubated for 3 h (20.51±4.71 µg and 2.81±1.16 µg) or 24 h (15.39±5.75 µg and 7.95±2.68 µg). Compared to that, the amount of analogously applied anionic SEON^{BSA} to cell-free inserts is 5.24±7.41 µg and 4.26±2.68 µg for 3 h and increases to 9.53±0.17 µg and 6.24±6.02 µg for 24 h. However, if membrane inserts are covered with HBMEC layers, most detected SPIONs are present within the barrier-forming HBMEC compartment. Thus, an incubation with fluidMAG-D increases to an iron accumulation of 3.12±0.30 µg after 24 h, whereas in case of SEON^{BSA} iron amounts within this compartment are significantly elevated to 9.95±7.15 µg after 3 h and 10.88±4.34 µg after 24 h. Focusing on iron contents detected within the lower acceptor medium, data imply that a three-hour incubation with fluidMAG-D results in a significant increase of iron (25.2±12.7 ng) compared to control inserts without SPION treatments, while for SEON^{BSA} an elevated tendency is observed but without statistical evidence. Extending incubation times for both particle types to 24 h significantly elevates iron contents of lower medium compartments especially for anionic SEON^{BSA}. Similarly, enhanced iron levels in well bottom-seeded lower cells are detectable with statistical evidence after 24 h for both fluidMAG-D (8.5±3.6 ng) and SEON^{BSA}

(11.2±6.6 ng), while for an incubation time of 3 h a statistically significant increase is observable for SEON^{BSA}-treated conditions only. Additionally to the MPS- and AAS-based quantification of iron within the distinct compartments of the transwell system, microscopic analyses of both upper barrier-forming HBMEC and underlaying lower cells after the incubation with fluorescence-labeled starch particles were performed. On the one hand, images presented in panel C demonstrate the presence of green particle signals in HBMEC layers after a three-hour incubation, which is further enhanced after 24 h. Remarkably, nano-screenMAG-G/D co-localizes with intracellular F-actin staining for both incubation times. On the other hand, analogous SPION signals co-localizing with F-actin staining of lower cells beyond the barrier can microscopically be detected very rarely after both 3 h and 24 h (see panel D).

Taken together, the passage of SPIONs trough the BBB-representing *in vitro* model is demonstrated by diverse methods comprising MPS and AAS for highly sensitive quantification and confocal laser-scanning microscopy for the optical detection and verification of particle internalization.

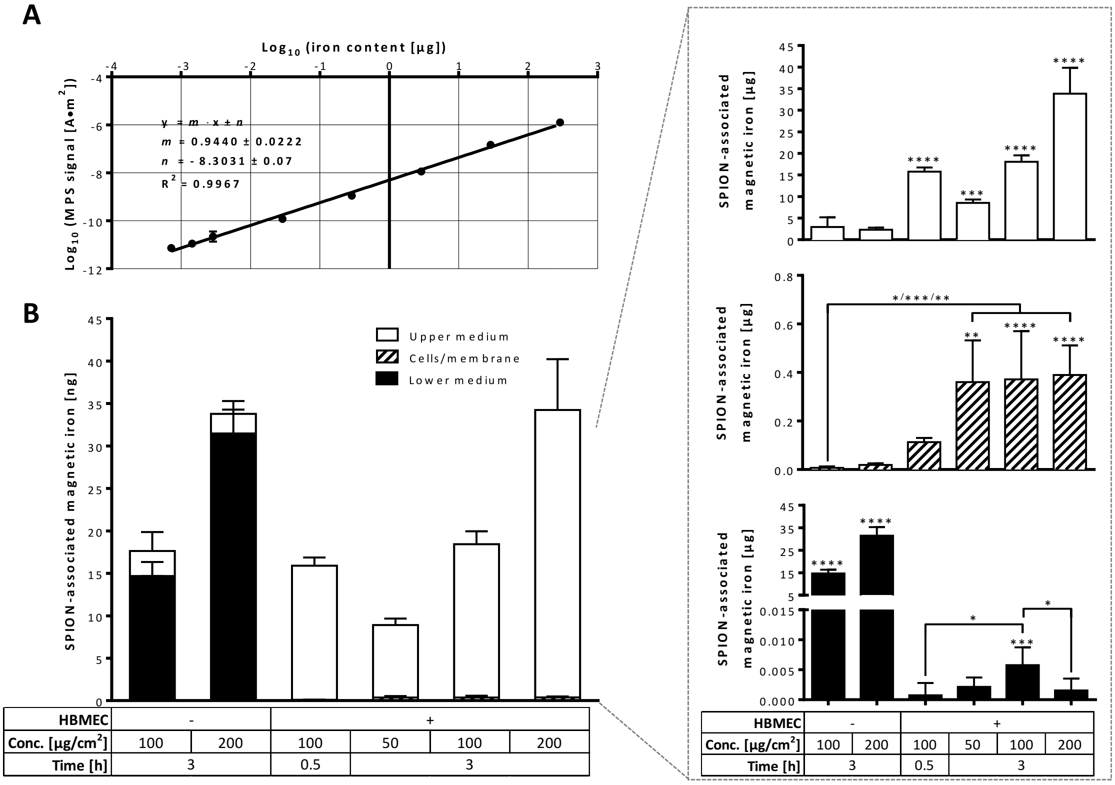

Figure 3.11: SPION distribution of distinct compartments of the *in vitro* blood-brain barrier model analyzed by magnetic particle spectroscopy (MPS). HBMEC were seeded on transwell inserts and cultured for five days. FluidMAG-D were added resulting in a final concentration of 50-200 µg/cm^2 (corresponding to 100-400 µg/ml) and incubated for up to 3 h, whereby the first 30 min were carried out on top of a block magnet. **A** Standard correlation curve of fluidMAG-D diluted in cell culture medium measured by MPS. **B** Compartment-specific contents of magnetic iron determined by MPS. Shown are means ± standard deviation of three independent experiments with three replicate inserts each. Statistical significance of samples compared to controls without SPIONs and amongst each other was tested by one-way ANOVA followed by Tukey's multiple comparison, where differences are considered as statistically significant for $p < 0.05$ (*), $p < 0.01$ (**), $p < 0.001$ (***), and $p < 0.0001$(****). Parts of the figure taken with permission from [151].

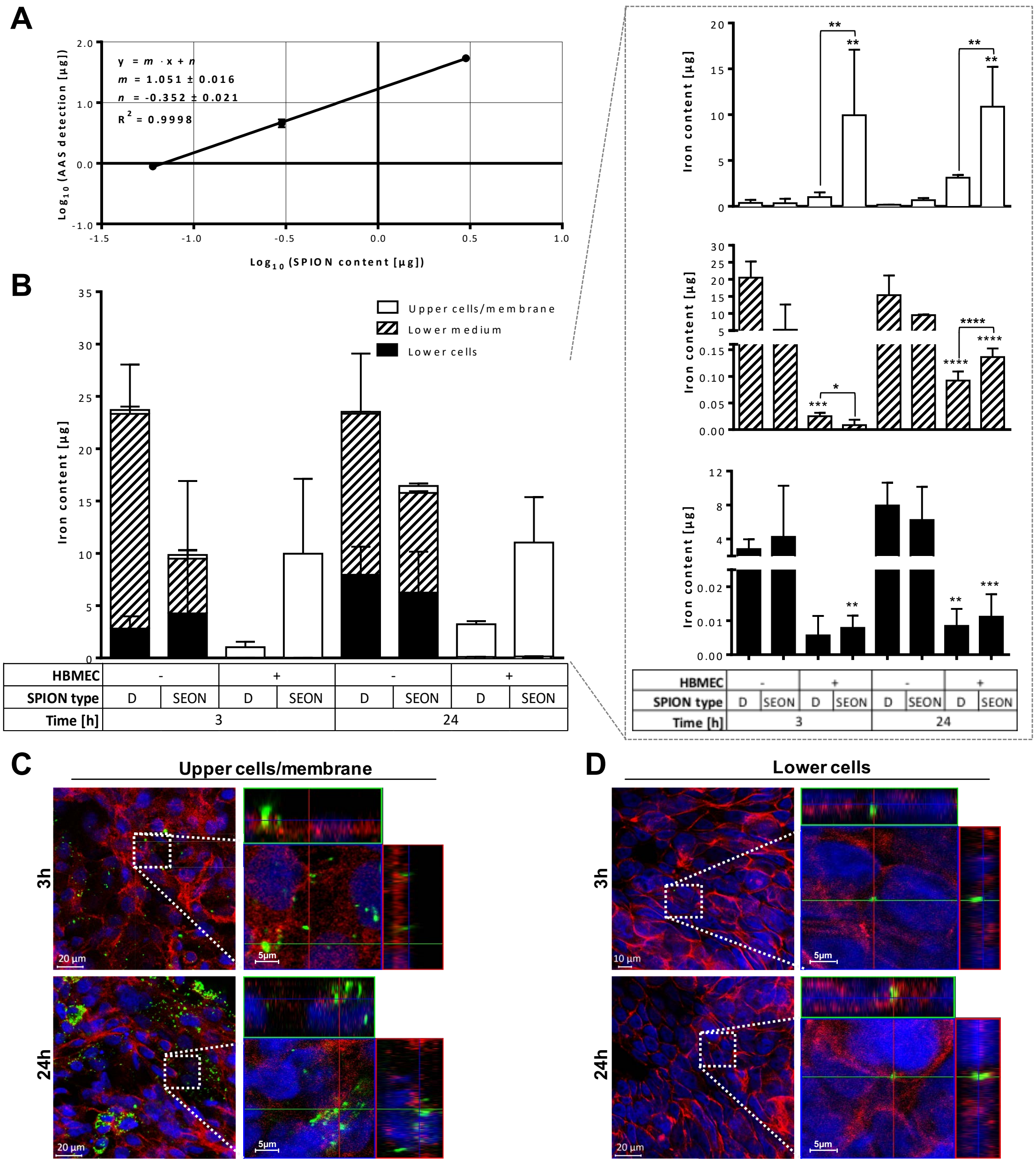

Figure 3.12: SPION distribution of distinct compartments of the *in vitro* blood-brain barrier model analyzed by atomic absorption spectroscopy (AAS). HBMEC were seeded on transwell inserts and cultured for five days. Indicated SPIONs were added resulting in a final concentration of 100 µg/cm^2 (corresponding to 200 µg/ml) and incubated for 3 h or 24 h, whereby the first 30 min were carried out on top of a block magnet. **A** Standard correlation curve of fluidMAG-D diluted in cell culture medium measured by AAS. **B** Compartment-specific contents of total iron determined by AAS. Shown are means ± standard deviation of three independent experiments with three replicate inserts each. **C-D** Fluorescent staining of barrier-forming HBMEC (upper cells/membrane, C) and MCF-7 cells seeded into well bottoms (lower cells, D) after incubation with nano-screenMAG-G/D (green). Nuclei and filamentous actin are stained with DAPI (blue) and Alexa Fluor® 633 Phalloidin (red), respectively. Samples were analyzed by confocal laser scanning microscopy. Statistical significance of grouped samples compared to controls without SPIONs and among each other was tested by two-way ANOVA followed by Dunnett's multiple comparison, where differences are considered as statistically significant for $p < 0.05$ (*), $p < 0.01$(**), $p < 0.001$ (***), and $p < 0.0001$(****).

3.4 SPION-induced Passage of Immune Cells trough Blood-Brain Barrier Model

The obvious route for SPIONs to cross biological barriers is their direct passage through barrier-forming cells. This option is demonstrated in detail for two different particle types in section 3.3.2 by utilizing the presented *in vitro* BBB model. However, there is also the possibility of other cells taking up SPIONs and subsequently transmigrating trough the biological barrier resulting in a cell-mediated delivery of particles. In order to investigate this relevant issue, immune cells characterized by either monocytic or neutrophil-like phenotypes were generated from THP-1 and HL-60 cells, respectively, as shown in supplemental figure B.6. For an effective cellular loading with SPIONs, SEON^{PAM} particles were added to differentiated THP1 (^{diff}THP-1) and HL-60 (^{diff}HL-60) cells resulting in a final concentration of 50 µg/cm^2 (corresponding to 189 µg/ml) and incubated for 120 min (see supplemental figure B.7). These SPION-loaded cells were added to barrier-forming HBMEC layers cultivated on FluoroBlok inserts and transmigration of ^{diff}THP-1 and ^{diff}HL-60 monitored depending on the presence of SPIONs themselves, the influence of an magnetic field, and the impact of an inflammatory stimulus.

3.4.1 SPION-mediated Transmigration of neutrophil-like HL-60 across Blood-Brain Barrier Model

As neutrophilic granulocytes constitute the most abundant fraction of leukocytes, they are likely being exposed to SPIONs present within the blood stream or other tissues. That is why the influence of ^{diff}HL-60's cellular loading with SPIONs was investigated respective to their transmigration across the HBMEC-based *in vitro* BBB model. Figure 3.13 summarizes the experimental outcome of these studies with continuous fluorescence measurements indicating transmigration kinetics of ^{diff}HL-60 across the biological barrier shown in panel A. Data show that non-loaded ^{diff}HL-60 ("blind neg. control") only slowly cross cell-free insert membranes, while upon the loading with SEON^{PAM} ("blind SPIONs") transmigration is more than doubled from 0.80±0.21 to 1.66±0.07 (relative to control conditions) after an incubation for 1,400 min. Strikingly, in the presence of HBMEC layers, the same particle pre-incubations of ^{diff}HL-60 ("SPIONs") elevate the passage of these neutrophil-like cells by approximately 89%, whereby especially for earlier incubation times the migration curve is steeper compared to non-loaded controls ("controls w/o SPIONs"). Additionally, applying a magnetic field for 30 min stimulates the presence of fluorescence-labeled $^{\text{diff}}$HL-60 within the lower acceptor compartment by 58±5% and even 102±7% relative to control cells at measurement time points of 30 min and 1,400 min, respectively. Similarly, during the presence of the inflammatory cytokine IL-1β the migratory kinetics of $^{\text{diff}}$HL-60 across the HBMEC layer is raised to 1.98±0.02 and 2.04±0.01 without and with the influence of an additional magnetic field. Upon having continuously monitored the cellular transmigration by fluorescence measurements for 1,400 min, microscopic analysis of fixed and counterstained membranes was performed in order to gain a more complete picture of ongoing events. Microscopic images of both upper and lower membrane sides are presented in panel B. Thereby, orange-labeled HBMEC cells are visible on upper apical membranes, whereas they are not detectable on lower basolateral membrane sides. $^{\text{diff}}$HL-60-representing green fluorescence signals, occasionally appearing on the apical and rarely on the basolateral membrane site, indicate the presence of these cells on the HBMEC layers or membrane before and after the transmigration However, only a low number of directly attached cells is detectable. Further results of lower acceptor compartments regarding the presence of $^{\text{diff}}$HL-60 beyond the HBMEC-formed barrier are shown in panel C. The presence of Nuclear Fast Red-stained $^{\text{diff}}$HL-60 in microscopic images verifies their transmigration across the BBB model. Remarkably, some Prussian blue-labeled SPIONs (indicated by arrows) can be detected within these cells in case of "SPIONs" samples, whereas the application of a magnetic field and/or IL-1β strongly elevates the presence of microscopically detectable cells and SPIONs within this compartment.

3.4.2 SPION-mediated Transmigration of monocytic THP-1 across Blood-Brain Barrier Model

In addition to neutrophil-like cells, monocytic cells form a class of phagocytosing leukocytes potentially being exposed to SPIONs. In order to study their ability to cross the BBB model upon loading with SEON$^{\text{PAM}}$, various analyses presented in figure 3.14 were performed using THP-1 cells differentiated to monocytic phenotypes ($^{\text{diff}}$THP-1). The time-dependent detection of fluorescently labeled cells within the lower acceptor compartment under indicated conditions is shown in panel A. Data indicate that ^{diff}THP-1 only marginally cross blank transwell membranes in the absence of HBMEC layers (0.44±0.08 of control conditions). However, the SPION loading of these monocytic cells strongly enhances the transmigration by 57% aligning to "control w/o SPIONs". In the presence of HBMEC layers, the migration of SPION-loaded ^{diff}THP-1 into lower acceptor compartments is sharply increased compared to controls especially for early incubation times as an 130-minute incubation induces an elevation from 0.29±0.06 to 0.58±0.04 for non-loaded and SEON^{PAM}-loaded cells, respectively. After an incubation for 1,400 min differences of 39±3% between these two conditions are still detectable. Additionally, applying a magnetic force to the system enhances the transmigration of SEON^{PAM}-loaded ^{diff}THP-1 to 1.56±0.08. Noticeably, the presence of IL-1β does not essentially affect the migration curve compared to analogous conditions without inflammatory stimulation. As seen previously, the microscopic analysis of fixed and counterstained transwell membrane samples presented in panel B reveal an even distribution of orange-labeled HBMEC cells covering upper apical membranes but not lower basolateral membrane sides. Whereas ^{diff}THP-1 labeled with green fluorescence are barely detectable on apical membrane sides, their abundant presence on lower basolateral sides implies an effective attachment of ^{diff}THP-1 after transmigration of HBMEC layers. In accordance to this observation, suspensious ^{diff}THP-1 are barely detectable within lower acceptor compartments' media as depicted in panel C. Furthermore, SPIONs are not visible within these few Prussian blue-stained cells.

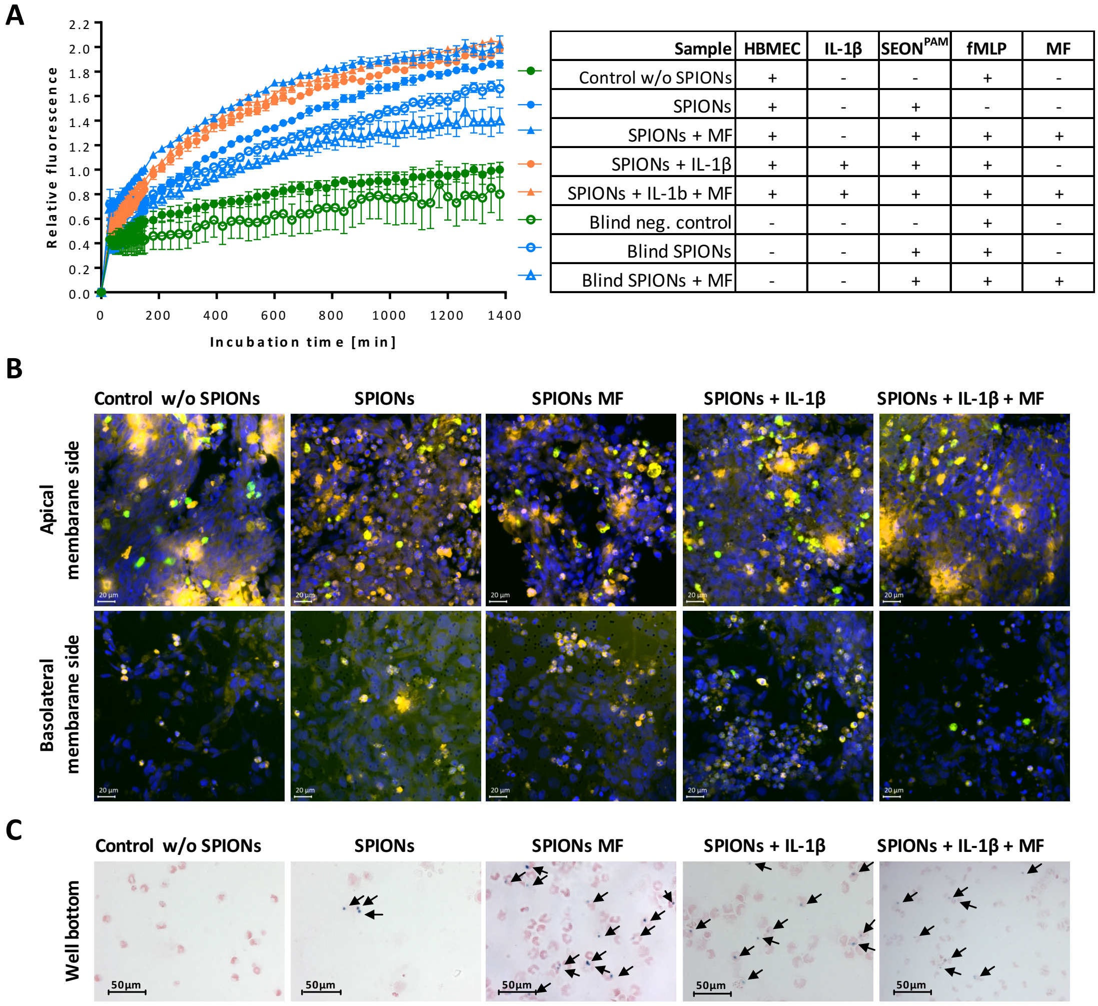

Sample	HBMEC	IL-1β	SEON^{PAM}	fMLP	MF
Control w/o SPIONs	+	-	-	+	-
SPIONs	+	-	+	-	-
SPIONs + MF	+	-	+	+	+
SPIONs + IL-1β	+	+	+	+	-
SPIONs + IL-1b + MF	+	+	+	+	+
Blind neg. control	-	-	-	+	-
Blind SPIONs	-	-	+	+	-
Blind SPIONs + MF	-	-	+	+	+

Figure 3.13: Transmigration of differentiated, SPION-loaded HL-60 cells across the *in vitro* blood brain barrier model. HBMEC were seeded on FluoroBlok transwell inserts and stained using CellTracker™ red CMTPX (orange) upon cultivation for five days. HL-60 differentiated with 1.4% DMSO (six days) were stained by CellTracker™ Green BODIPY® (green) and incubated with 50 µg/cm^2 (corresponding to 189 µg/ml) of SEON^{PAM} for 120 min. SPION-loaded HL-60 were added to HBMEC-seeded transwells with a density of 500,000 cells/insert. If indicated, HBMEC layers were pre-treated with 5 ng/ml IL-1β for 120 min before SPION-loaded immune cells were added. In order to chemically attract differentiated HL-60, acceptor compartments were provided with 10 nM (fMLP). For selected samples the first 30 min of incubation were carried out on top of a 24-well magnetic plate (indicated as "MF") before transmigration was monitored by fluorescence measurements of the lower compartment using a microplate reader. **A** Time-dependent relative fluorescence detected within the lower acceptor compartment. **B** After 1,400 min of transmigration transwell membranes were fixed, cell nuclei counterstained using Hoechst 33258 (blue), embedded on cover slips, and analyzed by confocal laser scanning microscopy. **C** Cells suspended in the lower acceptor compartment were transferred to microscopic slides by cytospin, fixed, and stained by Nuclear Fast Red. Additionally, SPIONs were stained with Prussian blue (indicated by black arrows). DMSO - dimethyl sulfoxide; fMLP - N-Formylmethionyl-leucyl-phenylalanine; MF - magnetic field; PAM - polyacrylat-co-maleat.

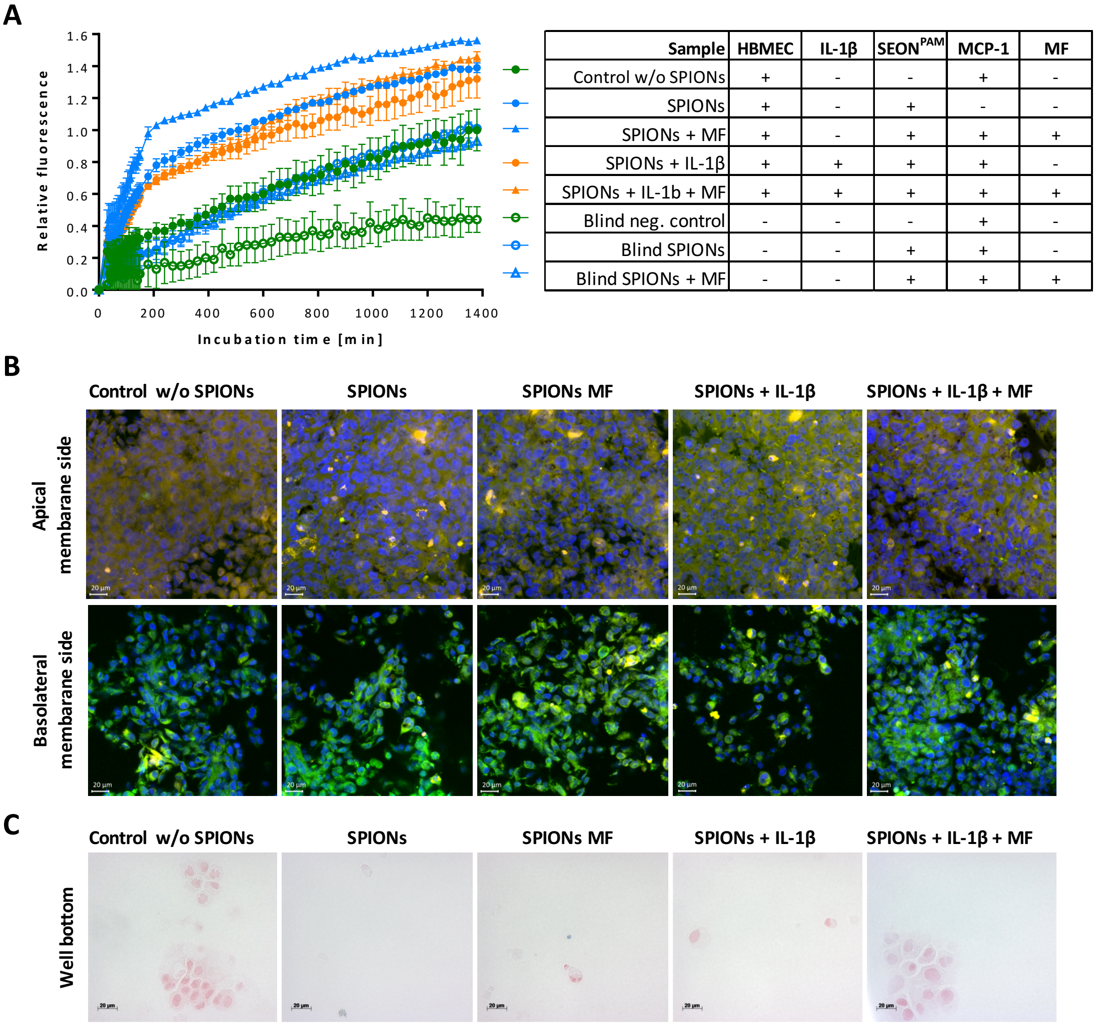

Sample	HBMEC	IL-1β	SEON^{PAM}	MCP-1	MF
Control w/o SPIONs	+	-	-	+	-
SPIONs	+	-	+	-	-
SPIONs + MF	+	-	+	+	+
SPIONs + IL-1β	+	+	+	+	-
SPIONs + IL-1b + MF	+	+	+	+	+
Blind neg. control	-	-	-	+	-
Blind SPIONs	-	-	+	+	-
Blind SPIONs + MF	-	-	+	+	+

Figure 3.14: Transmigration of differentiated, SPION-loaded THP-1 cells across the *in vitro* blood brain barrier model. HBMEC were seeded on FluoroBlok transwell inserts and stained using CellTracker™ red CMTPX (orange) upon cultivation for five days. THP-1 differentiated with 5 ng/ml PMA (five days) were stained by CellTracker™ Green BODIPY® (green) and incubated with 50 µg/cm^2 (corresponding to 189 µg/ml) of SEON^{PAM} for 120 min. SPION-loaded THP-1 were added to HBMEC-seeded transwells with a density of 300,000 cells/insert. If indicated, HBMEC layers were pre-treated with 5 ng/ml IL-1β for 120 min before SPION-loaded immune cells were added. In order to chemically attract differentiated THP-1, acceptor compartments were provided with 100 ng/ml MCP-1. For selected samples the first 30 min of incubation time were carried out on top of a 24-well magnetic plate (indicated as "MF") before transmigration was monitored by fluorescence measurements of the lower compartment using a microplate reader.**A** Time-dependent relative fluorescence detected within the lower acceptor compartment. **B** After 1,400 min of transmigration, transwell membranes were fixed, cell nuclei counterstained using Hoechst 33258 (blue), embedded on cover slips, and analyzed by confocal laser scanning microscopy. **C** Cells suspended in the lower acceptor compartment were transferred to microscopic slides by cytospin, fixed, and stained by Nuclear Fast Red. Additionally, SPIONs were stained with Prussian blue. MCP-1 - monocytic chemotactic protein-1; MF - magnetic field; PAM - polyacrylat-co-maleat; PMA - phorbol 12-myristate 13-acetate.

CHAPTER 4

Discussion

The utilization of nanomaterials for various applications is prevalent and steadily-increasing, which gives rise to an ever-expanding number of particle formulations [21]. In context of biomedical implementations, especially superparamagnetic iron oxide nanoparticles (SPIONs) are highly promising candidates, as they can be applied as contrast agents in magnetic imaging methods, as drug delivery systems with magnetic targeting, and for hyperthermia antitumor therapy during the presence of an alternating external magnetic field as well as many others [10, 41, 42]. To date, several SPION-based products are already clinically approved and commercially available [25], while even more are in the pipeline or under development for advanced biomedical applications [10]. On the one hand, the large degree of freedom in particle synthesis allows their tailored design and functionalization according to specific needs [21]. On the other hand, the great particle diversity demands an adequate risk and impact assessment for every individual formulation in order to achieve an efficient and safe implementation [74]. Both variabilities between different SPION batches and particle aging predominantly caused by oxidation present great challenges, too [158]. Moreover, a precise evaluation is frequently impeded by unique SPION properties such as optical properties, hydrophobicity, and catalytic activities, which often interfere with examination methods commonly used for studying other substance classes [74, 158, 159]. The introduction of SPIONs into biological systems embodies a challenging step along their way from scientific reports into clinical application. Prior to animal-based *in vivo* studies and clinical trials, convenient cell culture-based models combined with validated analyses represent powerful tools for efficient testing of biological effects of such substances in both mechanistic investigations and high-throughput practice. In consequence, *in vitro* pre-screening substantially contributes to the reduction of animal experiments in compliance with the principle of the "Three Rs" (*i.e.*, Replacement, Reduction, Refinement according to Altman [160]) [158, 161] and provides valuable insights into the biology of physiologic and pathophysiologic processes [127, 129, 130]. In the past, diverse cell lines have been utilized for the evaluation of nanoparticles including SPIONs [51, 162, 163]. In context of a whole organism, biological barriers embody striking structures essentially affecting biodistribution, tissue penetration, uptake, metabolism and storage of nanoparticles, as well as particle degradation and elimination [7]. In this context an important question is whether the biological barrier can act as a tight boundary layer protecting underlying tissue, such as the central nervous system (CNS), upon exposure to SPIONs. If not, the particle-induced impairment of barrier integrity may convey devastating effects such as influx of toxins, vasoactive substances as well as neuroinflammatory molecules [70]. Conversely it is important to evaluate if the barrier embodies an insuperable hurdle for SPIONs preventing their delivery during targeted therapy. These are fundamental questions, which need to be answered beyond doubt in order to achieve a safe and efficient biomedical particle implementation. Hence, the detailed understanding of which particle parameters affect barrier-penetrating, -disrupting, or -repulsing properties would take biomedicine a step further to the tailor-made design of SPIONs, which in turn accelerates the transfer of developed particles into clinical application. That is why in scope of this study a cell culture-based system representing a biological barrier is established and investigated in detail for the passage of SPIONs. Emphasis is put on a human brain microvascular endothelial cells (HBMEC)-based model representing the human blood-brain barrier (BBB), which embodies a highly sensitive and crucial interface between blood and the CNS. SPION formulations of different kinds comprising anionic, neutral, or cationic surface charges are tested. Besides particle passage through the barrier, SPION-induced consequences for barrier integrity are examined. The identification of reliable methods for the direct and highly sensitive SPION detection within the test system is focused on, too. In addition to the passage of free SPIONs through the BBB model, the ability of SPION delivery by barrier-penetrating immune cells, as well as the capacity of SPIONs to induce the barrier penetration by such immune cells, is evaluated.

4.1 General Biological Effects of SPIONs and Impact of the Protein Corona

In order to identify appropriate SPION candidates for the establishment of a reliable test system studying particle penetration through biological barriers, various types of SPIONs were analyzed for their effects on cellular interaction and cell viability. In accordance with data from literature [75, 159], both Prussian blue stain and flow cytometry (see figure 3.2) reveal that especially SPIONs coated with polyethylenimine (PEI, 750 kDa) exhibit intense interactions with HBMEC. Additionally, PrestoBlue™ assays (see figure 3.1) show pronounced cytotoxicity. These effects can predominantly be explained by the high cationic surface charge of these particles, which is assessed to +47±7 mV and +54±9 mV for non-labeled and fluorochrome-labeled PEI particles used in the presented study, respectively (see table 2.1). The considerably elevated positive zeta potential mediates a strong adsorption to negatively charged glycocalix and phospholipid membranes of cells and enhanced cellular loading with SPIONs [63]. The kinetic analysis of SPION loading by fluorescence-based flow cytometry implies a highly intense affinity to HBMEC immediately after addition to the cells. Remarkably, this interaction seems to decrease during the incubation process, indicated by both attenuated cellular fluorescence labeling and side scatter (SSC) signals detected. A reason for that decline might be found in the cytotoxic nature of these particles. Thus, heavily loaded cells severely disrupted from the impact of PEI-coated SPIONs are excluded from the cytometric detection of cellular events reducing the median cellular fluorescence signal. Additionally, the presence of fetal calf serum (FCS) within the incubation medium might induce the evolution of a protein corona on the surface of PEI particles. In turn, the cellular interaction of SPIONs can be reduced gradually and decelerated as discussed in detail later within this section. Fischer *et al.* demonstrated that besides the cationic surface net charge, charge density and flexibility of the three dimensional structure of the coating molecules also essentially determine biological effects [75]. They showed that the high-molecular-weight coating with 500 kDa diethylamine ethyl (DEAE)-dextran possessing low cationic charge densities shows good biocompatibility. In contrast, nanoparticles with polymer coating of similar molecular weight (600 kDa) of branched PEI, exhibit strong cytotoxicity based on the pronounced charge density. Given that fact, together with the moderately cationic zeta potential (+36±7 mV, see table 2.1) of fluidMAG-DEAE used in scope of this thesis, the elevated cellular adherence of DEAE-coated SPIONs revealed by Prussian blue stain accompanied by the slight cytotoxic effects observed during PrestoBlue™ assays can be explained. In contrast, anionic SEON^{BSA} do not demonstrate any significant effects on cell viability when evaluated by PrestoBlue™, whereas microscopic analyses of Prussian blue-stained HBMEC indicate a substantial cellular affinity already noted after a 3-hour incubation. Similar observations were made by Zaloga and colleagues, who detected that the exposure of primary human umbilical vein endothelial cells (HUVECs) to up to 75 µg/ml SEON^{BSA} did not reduce viable cell count, while flow cytometry data suggested sufficient cellular binding and/or particle uptake [133]. Interestingly, the authors could find significantly decreased SSC signals representing cellular SPION content, when comparing the particles to same formulations without an additional BSA coating. As both SPION types used by Zaloga *et al.* showed similar surface charges, the reduced cellular adherence of SEON^{BSA} was explained by the protein corona-induced decelerating effect on particle binding and uptake, too. With respect to neutral starch-coated SPIONs analyzed within the here presented thesis, no cytotoxic events are found during PrestoBlue™-based viability studies for up to 100 µg/cm^2 (equal to 378 µg/ml) for 24 h. This is accompanied by low cellular interactions shown by Prussian blue stain and flow cytometry during the first three hours of incubation, while a 24-hour exposure results in extensive cellular accumulation of fluidMAG-D and nano-screenMAG-G/D, respectively. Thus, the biocompatible phenotype of such starch-coated SPIONs may be mediated by the slow and gentle cell accumulation. In fact, neutral SPIONs are usually barely associated with cytotoxic events in previous literature [57, 78, 159], where a rational reason can be found in the low adherence at the polar plasma membrane [76]. This seems plausible especially when considering cellular interaction and cytotoxicity of biocompatible, less cell adhering neutral starch-coated and cytotoxic intensively interacting cationic PEI particles as discussed earlier in this section. Detecting the cellular accumulation of nanoparticles by flow cytometry-obtained SSC intensities has been described before [164–166]. Though comprehensive data achieved within this thesis clearly show, that the sensitivity of this internal complexity-associated SSC parameter is limited. Focusing on cells exposed to nano-screenMAG-G/D for up to 3 h, geometric means of cellular fluorescence labeling indicate gradually increasing cellular particle accumulation, while SSC signals do not change significantly or even slightly decrease. Only for strong particle accumulation upon incubations for 24 h elevated SSC is detectable agreeing with fluorescence signals. *Vice versa*, fluorescence-based data of nano-screenMAG-G/PEI-incubated cells reveal a clear decrease in mean cellular particle content after 180 min compared to 60 min incubation time, whereas SSC is not affected. Bringing these findings in context to biocompatibility data discussed earlier in this section, cytotoxic events inducing altered cellular morphology and internal complexity, such as nuclear fragmentation, cytosolic condensation, membrane blebbing and others [167], can interfere with a precise detection of cellular particle binding based on SSC. Moreover, particle aggregation and agglutination affect SSC signals too, which again impede the evaluation of cellular SPION loading exclusively based on SSC signals.

The determination of nanoparticle internalization by methods such as flow cytometry and SPION quantification procedures including ultraviolet spectroscopy, magnetic particle spectroscopy (MPS), and atomic absorption spectroscopy (AAS) is occasionally claimed [164, 165]. However, virtually no discrimination between surface-bound and actually internalized particles can be made, as even after several washing steps strongly bound SPIONs might remain on external plasma membranes. Consequently, they are detected during subsequent SPION quantification. Hence, in scope of this thesis, confocal laser scanning microscopy was used in order to gain information on the spatial distribution of cell-associated SPIONs to specifically identify internal particles. Thereby, SPIONs are defined as "internal" when co-localized with fluorescence-stained intracellular structures, such as the filamentous (F)-actin-based cytoskeleton. Thus, the additional treatment with distinct endocytosis inhibitors reveals that starch-coated nano-screenMAG-G/D are taken up into cells via energy-dependent mechanisms (see figure 3.3). As the cellular incubation with F-actin-depolymerizing cytochalasin D substantially reduces the uptake of the starch-coated particles, clathrin-dependent endocytosis seems to be predominantly involved in the particle uptake. This finding appears reasonable due to the superior role of clathrin-coated pits on brain microvascular endothelial cell (BMEC) membranes compared to only rarely abundant caveolin, which has been described before [70]. Moreover, similar studies identified clathrin-dependent endocytosis of diverse nanoparticle formulations [56, 57, 76] and the common clathrin-mediated transport of molecules at the BBB [168] as well. However, the fact that the additional presence of chlorpromazine further decreases the cellular incorporation of these starch-coated SPIONs indicates the ancillary involvement of more endocytotic processes. These might include other clathrin- and caveolae-independent pathways, as filipin incubation additional to cytochalasin D and chlorpromazine does not further attenuate the level of SPIONs found co-localized with intracellular F-actin. Indeed, the active clathrin and caveolae-independent uptake of other nanoparticles and polymers has been shown previously [169–171] and seems to be associated with electrostatically neutral or anionic formulations. Interestingly, this process was demonstrated to bypass Rab5-positive early endosomes/lysosomes and transport to the endoplasmic reticulum [170], which offers the possibility of particle transcytosis. In contrast to that, uptake mechanism studies of nano-screenMAG-G/PEI conducted within this thesis in presence of 4 °C, clearly demonstrate the energy-independent nature of this process. This implies that PEI particles are not taken up into cells by canonical endocytotic mechanisms but rather penetrate cellular membranes independent from intrinsic active internalization pathways. One possible route PEI particles may take can be based on the perturbation of the plasma membrane upon electrostatic adsorption. The induction of transient nanoholes within cellular membranes mediated by PEI polymers has been described before [57, 77]. Furthermore, the fact that PEI particle-treated cells are characterized by a strongly elevated positive stain with SYTOX® Red especially during early incubation (see figure 3.5) supports this hypothesis as discussed in detail later in this section. Another option for the internalization of PEI-coated SPIONs into cells might happen by facilitated diffusion via selective membrane protein channels. For cationic cargoes, membrane penetration through porines has been observed, though—based on channel geometry—its occurrence is restricted to particle sizes of up to 30 nm [172, 173]. However, a number of studies already revealed that nanoparticles of up to 600 nm show passive transportation into red blood cells lacking the endocytotic machinery [174, 175]. The exact mechanism and the question whether specific carrier proteins mediating passive transport are involved, has not been fully clarified yet.

The protein corona formed on the surface of nanoparticles in context of biological consequences has been focused on in several studies [95, 96, 176]. While it is clear that nanoparticle-protein interactions are highly dependent on particles' physicochemical properties, exposure time, and the protein source itself, the picture of how protein adsorption and nanoparticle properties correlate with cellular responses and subsequent mechanisms is still incomplete [53]. Nevertheless, the substantial influence of the protein corona, which can shield targeting ligands functionalized to the surface of therapeutic SPIONs has been shown several times [177, 178] and underlines its crucial role. That is why, one objective of this thesis comprises the investigation of protein corona-associated effects on cytotoxicity and cellular interaction with BBB-forming HBMEC. To this end, fluidMAG-PEI and nano-screenMAG-G/PEI were equipped with protein coronas. As demonstrated by figure B.1, particle incubation within rising concentrations of FCS induces increasing amounts of protein coronas conferring gradually ascending amounts of SPION-associated proteins as described by Gräfe *et al.* [157]. It has to be noted, that for the presented data SPION incubation in 100% FCS corresponds to an effective FCS content of 87% and 77% due to dilution upon addition of non-labeled and fluorochrome-labeled particles, respectively. Both PrestoBlue™ and real time cell analysis (RTCA) clearly demonstrate that progressive levels of protein corona on the surface of fluidMAG-PEI stepwise reduce acute- as well as long-term cytotoxicity for at least 72 h (see figure 3.4). Similar biocompatibility-inducing effects of the protein corona have been described for other nanoparticle formulations [97, 176, 179]. Interestingly, Wang *et al.* demonstrated that the presence of a protein corona on amino-modified polystyrene nanoparticles prevent cytotoxic effects of bare particles by avoiding early membrane permeabilization [179]. However, the authors observed lysosomal swelling and damage upon enzymatic digestion of the protein corona within the lysosome. Thus, cells exposed to protein corona-equipped formulations entered cathepsin-induced apoptosis by a delay of approximately 8 h. Comparing these findings to long-term RTCA assays performed in this thesis, such delayed cytotoxic events of protein corona-possessing PEI particles are not observed, even in spite of the utilization of 100 µg/ml (corresponding to 100 $\mu g/cm^2$) particles instead of 50 µg/ml used by Wang and co-workers. Possible explanations may be found in particle sizes different (40–50 nm) from the ones used in this thesis (157 nm, see table 2.1). Devoting attention to the particles' decreasing zeta potentials during progressive protein corona formation (see figure B.2), reduced cytotoxicity might be explained, as these hamper electrostatic interactions of the intrinsically cationic particles with anionic plasma membranes. Interestingly, flow cytometry-based data reveal a protein corona-dependent attenuation of cellular particle accumulation especially during early incubation times but more equalized cellular SPION loading after an 180-minute exposure (see figure 3.5). This fact supports the concept that in presence of the protein corona, particle-cell interaction is decelerated rather than impaired. In line with this hypothesis are microscopic observations revealing that both total cell-associated and internalized PEI particles decrease with ascending protein corona contents for early incubation times but not for an incubation of 3 h (see figure 3.6). Moreover, correlating the protein corona-dependent velocity for cellular interaction to cell viability, gives worthwhile insights (see figure 3.5): during early incubation progress the fraction of viable SYTOX® Red-negative cells is strongly reduced for intensively interacting PEI particles without protein corona. In contrast, slower interacting PEI particles with increasing protein corona do not show such effects. However, these differences are detectable to a minimal extend upon three-hour incubations. Furthermore, data clearly allow the direct correlation between cellular particle accumulation by corona-free SPIONs and positive staining with SYTOX® Red, especially after short-term exposure (see figure 3.5 panel D), which has never been shown before. One explanation for this phenomenon can be found in the fact that cells heavily loaded during exposure to no-corona PEI particles are rapidly destroyed and excluded from the cytometric detection of cellular events. In consequence, only remaining vital cells are uncovered during subsequent SYTOX® Red Dead cell staining and flow cytometric analysis. Though, as used particle concentration were only 25 µg/cm^2 (equal to 94.5 µg/ml), a more relevant reason might be found in the mechanism behind the assay itself. There, dead cells are defined by a positive stain with SYTOX® Red, which can not pass intact cell membranes but compromised plasma membranes [180]. Hence, SYTOX® Red-positive cells can be characterized by increased permeability, which does not inevitably mean cell death if limited. As PEI embodies a cationic polymer vector commonly used for transfecting nucleic acids into eukaryotic cells, its transient membrane-permeabilizing effect has been described before and is utilized for transferring nucleic acids into eukaryotic cells [181]. Moreover, Hong *et al.* showed that polycationic polymers can induce temporal nanoscale hole formation within membranes increasing cell permeability [77]. The authors demonstrated that cells recover upon exposure to low concentrations while integrated membrane damage due to elevated polymer amounts result in cell death. Similarly, SYTOX® Red-based data shown within the here presented thesis might indicate the transient induction of cell permeability for highly cationic PEI particles without protein corona during early incubation. In contrast, decreasing surface-charged particles possessing a protein corona do not. Furthermore, microscopic investigations of SPION internalization confirm the delay-inducing effect of protein corona-possessing PEI particles in context of cellular internalization processes (see figure 3.6). In line with this assumption are observations made during both flow cytometry-based and microscopic investigations of cellular particle accumulation and internalization under different incubation temperatures (see figure 3.7). Results point out that the presence of a protein corona on PEI particles essentially affects the uptake mechanism as corona-equipped SPIONs are barely detected inside 4 °C-incubated cells, whereas no-corona possessing particles are. As during incubations at 37 °C protein corona-possessing PEI particles are still internalized but more slowly, alternative active uptake pathways must be taken by these SPIONs. One possible scenario might include protein corona-originated ligand binding to surface receptors, which provokes receptor-mediated endocytosis. Whether clathrin-dependent or other endocytotic processes are involved needs to be investigated in future studies, where changes in SPION size due to protein corona formation should be focused on too. Nevertheless, such shifts in uptake mechanisms are conceivable and also other scientists observed similar phenomena for different particle formulations. Thus, Caracciolo *et al.* observed that bare cationic lipoplexes are internalized into murine fibroblasts via clathrin-dependent endocytosis, while the presence of a protein corona deflects entry mechanisms to caveolae-mediated pathways [182]. Taken together, the comprehensive and detailed investigation presented here provides profound insights into protein corona-induced effects and underlying interrelations. Thus, the conclusion can be drawn that—with regard to PEI-coated particles—the corona reduces the cationic particle surface charge, which in turn prevents the abrupt and highly intense adsorption to the anionic plasma membrane. Passive membrane penetration via the induction of nanoscale holes and subsequent cell permeability are substantially diminished. Hence, the protein corona formed on PEI particles strongly reduces cytotoxicity and decelerates SPION uptake.

4.2 SPIONs and the Blood-Brain Barrier Model

For a convenient and reliable assessment of the SPION passage through biological barriers and the resulting effects on barrier integrity, an appropriate and well-characterized model system is of vital importance. Focusing on a BBB-representing *in vitro* cell culture model, the well-established cell line HBMEC was utilized for seeding on porous transwell membranes separating the upper donor- from the lower acceptor compartment [131, 137]. While polytetrafluoroethylene (PTFE) membranes show improved visibility of seeded cells, the use of membranes made of polyethylene terephthalate (PET) were preferred, as elevated transendothelial electrical resistance (TEER) values are detected for cells seeded on the latter one (see figure 3.8). Besides the transwell membrane type, the medium type and additional supplement factors can influence the formation and tightness of the biological barrier. Apart from TEER measurements, molecular permeability of small-molecular-weight sodium fluorescein (NaFl) and microscopic evaluation of histological cross sections are performed for a detailed evaluation of barrier integrity. According to the recommendations of Deli and colleagues, the formation of tight junctions was analyzed by means of immunofluorescent staining of the associated protein *zonula occludens* (ZO)-1 as well [129]. Whereas Eigenmann *et al.* observed detrimental impacts [131], the beneficial effect of astrocytes in co-culture with BMECs or the use of astrocyte-conditioned medium (ACM) has been described by Siddharthan *et al.* [132]. Siddharthan and co-workers demonstrated that both cultivation arrangements significantly reduced the barrier's molecular permeability for propidium iodide by 30% and 70%, respectively, and increased TEER by more than 100%. The underlying mechanism is assumed to be based in the secretion of transforming growth factor (TGF)-β, glial cell-derived neurotrophic factor (GDNF), and fibroblast growth factor (FGF) by astrocytes [103, 104, 132]. Prompted by these findings, the integrity-enhancing impact of conditioned medium obtained from primary mouse astrocytes on HBMEC was tested in scope of this thesis (see figure 3.9). While ACM substantially increases the expression and peripheral distribution of ZO-1 in HBMEC, both TEER and NaFl permeability show only slight changes. These apparently contradictory observations may be based on the fact that under the influence of ACM, HBMEC form a continuous but highly tenuous cell layer as revealed by microscopic investigations of histological cross sections. Thus, narrow cellular layers and sporadic gaps allow the paracellular breach of ions through these layers to a higher extend compared to compact layers of elevated thickness, which most probably would apply to SPIONs as well. A reason for why HBMEC utilized within the here presented thesis do not sufficiently respond to ACM might be found in interspecies differences between human BMECs and mouse-obtained ACM. However, the response of immortalized mouse brain capillary endothelial cells on human TGF-β1 as well as the tightness-inducing effect of human FGF-2 on bovine brain capillary endothelial cells have been shown before [183, 184]. There, the molecular permeability was significantly reduced upon presence of the molecules. According to the UniProt database, the alignment of human and murine TGF-β1 (UniProt identifiers P01137 and P04202) as well as GDNF (P39905 and P48540) results in identities of 89.74% and 92.89% [185]. With regards to FGF, especially basic FGF-2 has been described as a potent factor for the induction of typical BBB characteristics [184, 186]. Aligning protein sequences of human (P09038) to murine (P15655) or bovine (P03969) FGF-2 gives 51.04% and 53.13% identity, predominantly based on the fact that the murine and bovine proteins are truncated by 134 amino acids on the amino-terminal end. The resulting lack of high-molecular-weight FGF-2, which possesses three nuclear localization sequences, might in turn cause the insufficient formation of highly condensed and thick HBMEC layers in the here presented thesis. This is underpinned by the fact that the FGF-2 isoform is thought to stimulate the mitogenic response and survival especially under serum-reduced conditions [187, 188]. In addition to ACM, medium supplementation with 550 nM hydrocortisone was tested too (data not shown). Although Schrot and colleagues demonstrated a hydrocortisone-induced increase in marginal folds of both murine and bovine BMECs [189], the human cells used in scope of this thesis do not respond on basis of TEER, molecular permeability, or ZO-1 expression and distribution. This corresponds to observations made by Eigenman *et al.* [131]. Hence, the usage of hydrocortisone was not pursued any further. The composition of FCS contained within cell culture medium is highly complex and may vary from batch to batch, which impedes reproducibility between different experiments. Thus, its abandonment during the generation of the BBB-representing *in vitro* model is verified as well. Data indicate that tight, continuous HBMEC layers possessing both elevated TEER values, low NaFl permeability, and enhanced overall and peripheral ZO-1 expression could only be obtained in presence of FCS during cell cultivation. Therefore, RPMI medium supplemented with 10% (v/v) FCS was used for the generation of HBMEC layers of high barrier integrity. Comparing resulting TEER values of maximum 52±2 Ω· cm^2 to literature reveals a good agreement with experimental setups using similar human cell models [129, 190–192]. Nevertheless, it is to be noted, that these human models using immortalized cell lines represent tightness parameters achieving only small fractions of the ones present *in vivo*, which are estimated to 1,000–2,000 Ω· cm^2 [110, 191]. Although comparable *in vitro* models utilizing primary cells of porcine or bovine origin generate up to 2,500 Ω· cm^2 [127], the transfer of experimental outcomes to human context is limited. Thus, instead of switching to non-human models, a further advancement of human *in vitro* seems reasonable. As indicated by several studies, the shift from static to dynamic cell culture systems does not only mimic *in vivo* situations present at the BBB more closely, but also beneficially affects phenotypes of BMECs [105,132,193,194]. Moreover, other sophisticated dynamic models utilize hollow fibers, which carry pulsatile flow and provide the framework for scaffolding BMECs in addition to astrocytes on luminal and abluminal surfaces [195]. Finally, the derivation of human BMECs from human induced pluripotent stem cells may also offer an attractive alternative, as TEER values exceeding 1,900 Ω· cm^2 could be reached using these cells and the induction of further BBB characteristics including the expression of tight junction proteins could be achieved [196].

Using the established HBMEC-based model system, SPION-associated effects on barrier integrity are investigated first (see figure 3.10). Thereby realistic SPION concentration prevailing at the biological barrier are difficult to estimate [197]. In general, particle dilution within the blood volume and clearance by the reticuloendothelial system (RES) contribute to low global concentrations. However, targeting strategies—either by surface functionalization or magnetic forces—might bring on strongly elevated local particle amounts [38]. Due to that, following investigations primarily address consequences of incubations with elevated SPION concentrations. In agreement with cytotoxicity data from two-dimensional cell culture experiments discussed above, neutral fluidMAG-D hardly influences the intactness of transwell HBMEC layers with respect to TEER values and NaFl retention, as well as microscopic analysis of histological cross sections for incubation of up to 24 h. A related study performed by

Thomsen and colleagues using starch-coated SPIONs made similar observations [190]. In contrast, the exposure to anionic SEON^{BSA} reduces TEER values in a time-dependent manner, while NaFl retention is significantly increased relative to controls before its pronounced reduction. Correlating these findings to microscopic investigations provides a reasonable explanation for the observed phenomenon: the rapid and comprehensive accumulation of SEON^{BSA} on HBMEC layers during the first three hours might obstruct the diffusion of NaFl molecules from the upper donor- into the lower acceptor compartment, which gives rise to an apparently elevated retention capacity for this molecular dye. Following further SEON^{BSA} incubation, NaFl permeability is finally increased due to the barrier-disrupting nature of these anionic SPIONs. This observation seems contradictory to the previously discussed biocompatible character of SEON^{BSA} detected with PrestoBlue™ viability assays performed on two-dimensional HBMEC cultures. In order to evaluate this issue, attention must be drawn to the differential growth stages prevailing in the distinct experimental setups: while for PrestoBlue™ viability assays cells are in a proliferative phase, barrier-forming cells on transwell membranes have been in confluence for several days before SPIONs are added. Indeed, RTCA analyses of HBMEC exposed to SEON^{BSA} shown in figure B.3 imply that acute adverse effects induced by SEON^{BSA} exposure of proliferating HBMEC are marginal only, while particle addition to confluent HBMEC layers evokes a rapid and concentration-dependent reduction of relative cell indices. The RTCA-based detection of cell indices is predicated by impedance measurements generated by adhering cells. Thus, not only cytotoxic events reducing the number of viable cells are detected, but alterations in cell morphology, cell-surface and cell-cell contacts influence the experimental outcome too [198]. Taking all these factors together, data presented in this thesis strongly indicate the possibility that intensively-interacting SEON^{BSA} destabilizes the established cell layers by events such as disturbing cell-cell contacts, which eventually reduces barrier integrity and elevates endothelial permeability. Moreover it has to be noted, that the strongly damaged appearance of histological HBMEC cross sections upon SEON^{BSA} incubation is probably strengthened by the multistep sample preparation upon barrier destabilization. Do SEON^{BSA} particles specifically bind distinct cellular structures and surface components or are there general non-specific interactions with cells that bring on the barrier disruption? Does immunogenicity in cells of human origin in response to the massive exposure to bovine albumin via the induction of permeability-increasing cytokines play a role? Based on the protein alignment of human and bovine albumin (UniProt identifiers P02768 and P02769) an identity not exceeding 76.34% leaves scope for such possibility [185]. Additionally, cytokine-inducing effects in human cell cultures have been described before [199]. In order to answer this question further comprehensive analyses are still pending. In general, (human) serum albumin seems highly attractive for drug transport due to its charge-reversible feature together with its endogenous origin and particle-stabilizing effects [10, 200]. With reference to cationic fluidMAG-PEI, more pronounced diminishing impacts on HBMEC layers are already detectable after a 3-hour incubation, which manifest in the significant reduction of both TEER and NaFl retention and agrees to PEI particles' cytotoxic phenotype mentioned earlier in this chapter. Similarly in accordance with biocompatibility observations discussed above, an exposure to cationic fluidMAG-DEAE entails no relevant detectable effects on barrier integrity. In spite of these interesting aspects, both cationic particle formulations are not suitable for the transwell test system assessing particle passage through the biological barrier. The reason for being that—probably based on excessive particle accumulation and agglutination within the cell culture medium with aggregates of up to 5 µm (data not shown)—neither fluidMAG-PEI nor fluidMAG-DEAE pass cell-free transwell membranes in an appropriate manner as demonstrated in figure B.4. Hence, for subsequent evaluations of SPION passage through the *in vitro* model representing the human BBB, neutral fluidMAG-D and anionic SEON^{BSA} are utilized.

Tracking of nanoparticles within biological systems is still complex, time-consuming, expensive, and usually provides only limited static insights into particle localization [201]. Requiring elevated resolutions, transport studies in cell culture-based setups often use radioactive- and chromatography-based methods as well as spectroscopic detection of fluorochrome-labeled particles. Especially with respect to the latter, both disintegration of the fluorescent dye and dye leakage are serious issues leading to critical consideration of data detecting and quantifying nanoparticles in biological settings [202, 203]. The use of SPIONs, on the one hand, hampers the application of various analytical assays due to their special optical properties as mentioned earlier [74, 158, 159]. On the other hand, it opens up new possibilities in specifically utilizing the iron-based character for direct particle detection [164]. Hence, SPIONs' superparamagnetic properties are exploited in scope of this thesis in order to highly sensitively quantify particle amounts present within the distinct compartments of incubated HBMEC transwell systems, which in turn gives insights into particle passage at this biological barrier. By applying MPS it is shown that this technique based on the non-linear magnetic susceptibility response, accurately and highly sensitively detects fluidMAG-D particles over multiple orders of magnitude (see figure 3.11). Utilizing the MPS-based direct detection of SPIONs within such barrier interaction studies are made for the first time in scope of this thesis and provide profound insights on the passages' dynamics and underlying mechanisms [151]. Actually the comparison of MPS, ultraviolet/visible-, atomic absorption- and atomic emission spectroscopy by Friedrich *et al.* already identified MPS as the most sensitive technique [164]. Focusing on here presented experimental outcome obtained from compartment-specific quantification of fluidMAG-D in the transwell model, data indicate that the presence of an HBMEC layer on the transwell membrane almost entirely prevents the translocation of fluidMAG-D from the upper into the lower compartment, which confirms the pronounced barrier tightness. Strikingly, the increase of particle concentrations from 50 µg/cm^2 to 100 µg/cm^2 and 200 µg/cm^2 (equal to 100–400 µg/ml) does not enhance SPION accumulation within the cellular fraction. This fact might suggest that HBMEC can not bind and internalize more of the starch-coated particles during the first three hours of incubation, potentially due to a fully stretched cellular endocytosis apparatus. As discussed above, the slow cellular accumulation kinetics as well as the active clathrin-dependent uptake of fluidMAG-D into HBMEC correspond well to this assumption. Moreover, another substantial factor affecting the bioavailability of SPIONs to cells must be seen in particle agglomeration. As high SPION concentrations diminish the nanoparticles' stability, decreased amounts of free particles contribute to less particle-cell interaction and the generation of false negative or false postive results, which have been discussed in literature previously [158]. The fact that within the lower acceptor compartment a small but statistically significant amount of SPIONs is detectable after the 3-hour incubation with 100 µg/cm^2 fluidMAG-D only, provides further proofs for the active particle transport across the BBB model via transcytotic processes. The absence of SPIONs within this compartment after 30 min implies the time-dependent character. Furthermore, the decrease of acceptor-specific magnetic particles after exposure to 200 µg/cm^2 fluidMAG-D compared to 100 µg/cm^2 supports the hypothesis of reduced cellular uptake and transcytosis due to decreased bioavailability and presence of larger particle agglomerates. In order to verify the transcytotic passage of fluidMAG-D through HBMEC layers, the incubation with endocytosis inhibitors during SPION exposure can provide substantial evidence. Nevertheless, as demonstrated by figure B.5, the treatment of stable HBMEC layers with inhibitors restricting either all active endocytosis pathways (*i.e.*, 4 °C) or clathrin-dependent mechanisms (*i.e.*, chlorpromazine and cytochalasin D) strongly increases endothelial permeability. Hence, such control experiments are inappropriate, as SPIONs passaging the HBMEC layer paracellularly interfere with an accurate assessment of transcytosed particles present within the lower acceptor compartment. Further studies approving transcytosis within this experimental setup in more detail are required. Time series of high resolution microscopic techniques such as electron microscopy may provide a possible option. In addition, the verification of exosomal markers or membrane remnants on the surface of SPIONs arriving within the lower acceptor compartment may underline the transcytotic passage, but is intricate due to low amounts of accessible particles. Anyway, the presence of active transcytotic processes of SPIONs without any additional functionalization has been suggested by different using other experimental setups, too. For instance, using starch-coated SPIONs of 100 nm, it has been observed that particles do not cross cell-free transwell inserts without an external magnetic field, whereas they traverse cell-seeded inserts [190]. Another study performed by Kim and colleagues implies that receptor mediated transcytosis seems to play a key role during translocation of anionic polyethylene glycol (PEG)-coated nanoparticles (140 nm) at BBBs represented by rat BMECs [204]. Remarkably, authors also emphasize the crucial involvement of the protein corona during this process. In addition to MPS, in this thesis AAS is used in order to spectroscopically quantify total iron and validate particle passage through the *in vitro* barrier model, also in context of SEON^{BSA} (see figure 3.12). As MCF-7 cells have been observed to incorporate diverse types of SPIONs to a high degree (data not shown), these cells seeded into bottom wells are used representing underlying tissue cells, which additionally indicate particle passage through the HBMEC layer. Agreeing to previously discussed particle-cell interaction, AAS reveals a far superior role of anionic SEON^{BSA} regarding the accumulation within barrier-forming HBMEC layers compared to neutral fluidMAG-D. Despite this multiple increased amount of SEON^{BSA} present within HBMEC compartments, only a low proportion proceeds into the lower acceptor compartment's medium or tissue-representing cells, whereas already after 3 h of particle incubation about twice as much fluidMAG-D is found within the lower compartments. This hints towards a constrained extend of SEON^{BSA} penetration through HBMEC layers and implies the cell-accumulating nature of these particles. The eventual elevation of iron within lower acceptor compartments 24 h upon SEON^{BSA} addition might result from enhanced paracellular particle passage through HBMEC layers resting upon barrier-destabilization and disruption by these particles as discussed earlier in this section. Indeed, Harush-Frenkel and co-workers observed that in contrast to cationic NPs, anionic NPs undergo degradative lysosomal processes upon uptake into human epithelial cells detected by means of fluorescence-based co-localization studies [205]. Thus, these particles hardly underwent transcytosis in this report as well. Another study performed by Lin *et al.* demonstrated that albumin nanoparticles were able to cross monolayers of murine BMECs and finally ended up in glioblastoma cells, which highly express the albumin-binding secreted protein acidic and rich in cysteine (SPARC) [206]. Unfortunately, the authors did not focus on the barrier-penetrating process and its consequences for barrier integrity, therefore no data regarding barrier integrity are available in the indicated study. Thus, data obtained within the here presented thesis provide valuable insights into ongoing processes and consequences. The overall comparison of data obtained from MPS and AAS shows elevated iron amounts for the latter. This is accounted for by the fact that MPS is based on the specific detection of intact superparamagnetic particles, while during AAS degraded particles or particle fragments also contribute to the determined signal. Another relevant issue can be seen in potentially altered magnetic behavior of SPIONs during the incubation progress. Thus, pronounced particle agglomeration modifies the magnetic susceptibility response. As such a shift is detected by ratios of the 5^{th} and 3^{rd} spectrum amplitude (*i.e.*, A5/A3 ratio) recorded during MPS measurements, inaccuracies can be corrected by switching to references of convenient A5/A3 ratios [147]. An alternative method for the highly sensitive *in vitro* quantification of SPIONs, regardless of any particle labeling might be seen in a technique introduced by Gunn and co-workers [207].

There, authors utilized the standardized methodology of proton nuclear magnetic resonance to quantitatively detect SPIONs within biological samples for five orders of magnitude and iron concentrations of 10 ng/ml. However, the particles' disintegration as well as cell debris and cell digest hamper the unconditional application of this methodology [207]. Taken together, the data presented here demonstrate that the combination of the *in vitro* model with both SPION quantification methods (*i.e.*, MPS and AAS) and integrity evaluating assays allow the detailed investigation of SPION passage through this biological barrier and the assessment of resulting consequences on the barrier itself.

4.3 SPIONs and Barrier-penetrating Cells

The straight passage of free SPIONs across biological barriers is one option delivering particles into the tissue beyond. Another possibility recently attracting attention is the cell-mediated transport of nanoparticles through such barriers [208]. Neutrophils constitute approximately 60% of leukocytes and are the first immune cells immobilized from the blood pool invading respective sites upon tissue damage and infection [209]. This dramatic neutrophilia primarily provokes the typical features of an acute inflammation, as well as induces the release of monocytes from bone marrow [209]. On their chemokine-directed way, monocytes differentiate into macrophages embodying the subsequent type of immune cells arriving at the inflammatory site. Thereby, both neutrophils and monocytes/macrophages are phagocytosing cells with distinct barrier-penetrating abilities. Thus—in context of the BBB—they may shuttle SPIONs ingested at the luminal site of circulating blood into the brain, which in turn can deliver therapeutics [208]. *Vice versa*, the uptake of circulating SPIONs into these cells might promote cell migration and their penetration through the BBB, which might be enhanced further by an external magnetic field or inflammatory brain conditions. In scope of this thesis the SPION-delivering ability of monocytic and neutrophilic cells, as well as the SPION-mediated effect on their cellular transmigration across the BBB model are investigated. As demonstrated in figure B.6, human leukemic cell lines HL-60 and THP-1 are utilized for their differentiation into neutrophilic-like and monocytic cells as described before [138–141]. Matching to expectations and previous observations [210] respectively, both obtained phagocytotic cell types display an augmented SPION accumulation compared to barrier-forming HBMEC, whereby anionic SEON^{PAM} particles are superior to neutral fluidMAG-D (see figure B.7). While cell viability is not compromised for incubations of up to 100 µg/cm^2 (corresponding to 378 µg/ml; see figure B.8), AAS reveals that incubation of differentiated HL-60 and THP-1 with 50 µg/cm^2 (corresponding to 189 µg/ml) SEON^{PAM} for 120 min results in total iron contents of 11.75±0.17 pg/cell and 16.63±0.07 pg/cell, respectively (data not shown). Compared to a similar study incubating primary human macrophages with 100 µg/ml anionic caboxydextran-coated SPIONs, which resulted in an iron load of approximately 8 pg/cell [211], data are in good agreement. Transmigration experiments of SEON^{PAM}-loaded ^{diff}HL-60 and ^{diff}THP-1 cells across the *in vitro* BBB model clearly show a SPION-induced cellular translocation from apical donor- to basolateral acceptor compartments (see figures 3.13 and 3.14). Several studies already demonstrated that SPIONs promote the differentiation of monocytes to macrophages and in general exert immune response-inducing effects on monocyte-derived macrophages and neutrophils [210, 212, 213]. Underlying mechanisms can be found in the oxidative stress-inducing nature of SPIONs as well as their induction of altered gene expression of pro- and anti-inflammatory cytokines such as interleukin (IL)-10, IL-1β, and IL-8 [210, 213, 214]. Interestingly, transmigration in scope of the here presented experimental model is distinctly pronounced in presence of barrier-forming HBMEC for both cell types. That seems reasonable, as several steps of this process, such as capture, rolling, arrest, and crawling, depend on the formation of distinct cell-cell contacts between the endothelium and transmigrating granulocytes or monocyte/macrophages [209]. The pronounced homing of SPION-ingested macrophages across the BBB into the central nervous system has also been suggested by Tong *et al.*, who performed animal studies with acute inflammatory mouse models [210]. This study is in line with here presented data implying that also in absence of the chemotactic stimuli *N*-Formylmethionyl-leucyl-phanylalanine (fMLP) and monocyte chemotactic protein (MCP)-1 the exposure of ^{diff}HL-60 and ^{diff}THP-1 to SEON^{PAM} is sufficient to induce transmigration through the barrier. Furthermore, an *in vivo* study performed by Alizadeh and co-workers pointed out that macrophages, which had taken up intravenously applied nanoparticles not only crossed the BBB but also accumulated in close proximity to glioma cells [215]. The chemoattractive nature of vascular endothelial growth factor (VEGF), which is highly expressed in glioma cells, might play a major role in this regulatory process [89]. Another work presented by Chu *et al.* impressively demonstrated on the basis of an *in vivo* mouse lung inflammation model, that neutrophils effectively transferred drug-loaded nanoparticles into inflammatory sites and alleviated inflammatory symptoms [216]. Taken together, these facts emphasize both the tumor- and immuno-attractant properties of such particle-loaded cells, which might in turn be exploited for an enhanced delivery of therapeutic nanoparticles as well as immuno-responsive cells during therapies such as of inaccessible brain tumors. *Vice versa*, this migratory-inducing ability of monocytes/macrophages and neutrophils must be given special consideration to during the therapy of patients suffering from chronic neuroinflammatory diseases. For instance, in multiple sclerosis the enhanced invasion of nanoparticle-incorporated monocytes as well as neutrophils might exacerbate the progression of neuronal demyelination [217]. Hence, detailed knowledge on SPION-induced consequences with respect on BBB's integrity and immune cell penetration is of vital importance for a safe and efficient particle implementation, where the here presented *in vitro* system offers a comprehensive test platform. IL-1β is a major mediator of the inflammatory response and with regards to the BBB negatively regulates barrier integrity via decreasing tight junction formation [104]. In this work, brain inflammatory conditions are induced using IL-1β, which provokes the elevation of various barrier permeability parameters (see figure B.9). Nevertheless, transmigration experiments reveal that pre-conditioning of HBMEC layers with this inflammatory molecule does only augment the strength of barrier penetration by neutrophil-like $^{\text{diff}}$HL-60 but not monocytic $^{\text{diff}}$THP-1. As the phorbol ester-based induction of IL-1β receptor expression, which is decisively involved in IL-1β-mediated cell recruitment, has been described before [218], the reason for non-responding $^{\text{diff}}$THP-1 is not clear. However, as it has been shown by several studies, astrocytes and microglia have a substantial impact on the regulation of BMEC permeability and leukocyte recruitment especially during inflammatory conditions [219–221]. This fact points out the need for an extension of the here presented *in vitro* model of the BBB to a co- or tri-culture system along with astrocytes and/or pericytes for detailed analyses of immune cell migration as well as SPION passage with regards to an inflammatory status. Magnetic (drug) targeting provides a large field of SPIONs' application and may do great work to overcome difficulties in efficient delivery of therapeutic substances also with respect to barrier passage. In context of the application of an additional magnetic stimulus for the first 30 min of leukocyte transmigration through the HBMEC layer, strong accelerating effects on SPION-loaded $^{\mathrm{diff}}$HL-60 and in particular $^{\mathrm{diff}}$THP-1 are noticeable in the work presented here. The superior role of monocytic THP-1 to neutrophil-like HL-60 may be due to the elevated cellular particle loading as discussed above. In line with this observation, Kong *et al.* demonstrated that in a rat model the accumulation of SPIONs within brain tissue is strongly augmented upon magnetic targeting [197]. Furthermore, the enhanced delivery of monocyte-delivered SPIONs into the brain via magnetic heating has been shown only *in vivo* before [210,222,223], where reversible BBB permeability was induced in presence of an alternating external magnetic field. As indicated in figure B.10 barrier transmigration of $^{\mathrm{diff}}$THP-1 strongly impair barrier integrities, whereas $^{\mathrm{diff}}$HL-60-penetrated HBMEC layers seem only disintegrated in presence of additional inflammatory stimuli. Furthermore, data presented by this figure suggest that SPION contents within the lower acceptor compartments are not quantitatively detectable by AAS. However, this might be brought about by insufficient sensitivity, as microscopic images of Prussian blue-stained HL-60 (see figure 3.13) reveal the actual presence of SPIONs associated with these neutrophil-like cells upon transmigration. Most likely due to the accumulation of adherent THP-1 at bottom sides of transwell membranes no or only few cells were noticeable on the bottom or within the lower acceptor medium compartment (see figure 3.14). Thus, no information on whether these cells actually transported SPIONs across the BBB model are available from the here presented data. Whether SPIONs remain within barrier-forming HBMEC during leukocyte transmigration, which in turn might influence the barrier's function, needs to be investigated in future studies. Similarly, an excess SPION loading of monocytes/macrophages or granulocytes might hamper migratory abilities of these phagocytosing cells as suggested previously [210]. Additionally, enhanced SPION binding to structures of the BBB upon particle functionalization and subsequent magnetic radiofrequency may irreversibly disrupt this biological barrier. All of these factors have to be assessed in order to achieve an efficient and safe biomedical implementation of SPIONs. Hence, both the here presented *in vitro* model representing the human BBB and the indicated experimental assays and detection methods are valuable tools contributing to the scientific and purposeful elucidation of these objectives.

CHAPTER 5

Conclusion & Outlook

The here presented thesis establishes an experimental *in vitro* tool for the detailed evaluation of SPION interactions at and passage through a biological barrier including the assessment of SPION-associated consequences for the barrier integrity. By utilizing the BBB-representing HBMEC monoculture transwell system in combination with several barrier integrity parameters and sensitive SPION detection methods, the two distinct SPION systems of neutral starch-coated fluidMAG-D and anionic BSA-coated SEON^{BSA} are extensively tested. For the first time, MPS is adopted in this experimental biological setting analyzing SPION passage through biological barriers in order to achieve a direct and highly sensitive particle detection within the distinct compartments. Hence a profound insight into passage's dynamics is provided. Furthermore, presented results impressively demonstrate that free fluidMAG-D traverse the barrier system in a time-dependent manner most likely based on clathrin-induced transcytotic processes. In addition, barrier integrity remains unaffected upon particle passage, which is explained by the comparatively slow and gentle cellular accumulation and uptake. In contrast, data imply that SEON^{BSA} intensively assemble within the barrier-forming cells and affect the BBB model in a barrier-disrupting manner. Another aspect addressed within this thesis refers to cell-mediated SPION delivery across the BBB by both neutrophils and monocytic cells derived from HL-60 and THP-1 cell lines, respectively. On the one hand, SPION engulfment by both cell types massively enhances barrier penetration of indicated immune cells. On the other hand, it is implied that these phagocytosing immune cells can be hijacked to deliver SPIONs across this *in vitro* model. These observations are made for non-functionalized SPIONs and can be carried out for each individual SPION formulation in order to achieve a comprehensive risk assessment. For applications not targeting the brain, particle penetration into and accumulation within the CNS upon repeated administration is strictly undesirable. Though, according to purposes when transition of SPIONs into brain is required—for instance in case of SPION-mediated drug delivery or hyperthermia therapy of glioblastoma—additional functionalizations such as by ligand binding may be utilized for the enhanced particle delivery across the BBB and need to be evaluated as well. The here presented test system provides an appropriate platform for both instances and allows an insight into underlying mechanisms, thus contributing to a comprehensive understanding of particle interactions with the BBB. In consequence, gained knowledge aids to the tailored design of SPIONs according to the particular application. Furthermore, the presented investigations focusing on the impact of the protein corona emphasize its pivotal role on biological effects and underline the need of its consideration during SPION functionalization as it may present opsonins or shield functional groups on the particle surface. Utilizing and extending the here established system, the inclusion of flow conditions—for instance by transferring the system into a microfluidic biochip as previously shown for other models [224]—might mimic the *in vivo* situation even closer. Also the integration of continuous SPION detection within the lower acceptor flow chamber finally allows sustained insights into the passage's dynamics and kinetics. The here presented SPION detection via MPS provides an excellent methodology for implementing this proposal. Additionally, the transfer of the presented test system to a blood-placenta barrier-representing regime has been introduced recently [225] and provides further information regarding SPION-associated impacts on this biological barrier. Nevertheless, it has to be noted that the experimental setup has some limitations, too. Results indicate that especially when testing the passage of free SPIONs as well as their leukocyte-mediated transport across the BBB under inflammatory conditions, an extension of the monoculture system to a co- or tri-culture system with astrocytes or/and pericytes seems reasonable. Whereas such elevated models are more difficult in handling and more interference-prone, they even closer represent the complexity of this biological tissue and incorporate the eclectic interplay of BMECs with surrounding astrocytes or microglia during inflammatory states. The detailed analysis and magnetic characterization of SPIONs after barrier penetration is of vital importance as this also influences tissue distribution, magnetic response during SPION applications such as imaging or therapeutic heating and elimination processes. Hence, the HBMEC *in vitro* model in line with further verifications according to Barnes *et al.* [226] must be utilized for such clarifications in the future. Resulting knowledge can help to improve arrangement of magnets in order to achieve appropriate magnetic fields, which optimize SPION application efficacy. Pedram *et al.* emphasized that the application of a magnetic field between 0.6–2.5 T and a minimal gradient and/or amplitude are crucial for not damaging the BBB [227]. Furthermore, alternative approaches in magnet-assisted transport of SPIONs across barriers and into deeper tissues might solve problems in the delivery of therapeutic substances. A remarkable example can be seen in the novel method developed by Shapiro and colleagues, who use a two-magnet system in order to push magnetic nanomedicines into diseased tissue [228]. Taken together, SPION-based therapies bear promising and versatile potentials to solve major biomedical problems. For instance, the combination of Temozolomide with radiosensitizing nanoparticles loaded with O^6-methylguanine-DNA methyltransferase (MGMT) inhibitors is a promising approach to overcome chemotherapeutic resistance in glioblastomas [46]. Analogously, hyperthermia therapy before radiotherapy reduces activation of the protein kinase Akt, which in turn radiosensitizes glioma cells [46]. However, in order to bring safe and efficient approved formulations on the way, data obtained from the here presented *in vitro* tool can contribute tremendous and viable knowledge.

APPENDIX A

Materials

Table A.1: List of used chemicals.

Chemical substance	**Supplier**
1,10-phenanthroline, $\geq$99% Agarose BioReagent, low EEO BSA, heat shock fraction, pH 7, $\geq$ 98% Chlorpromazine hydrochloride Cytochalasin D from *Z. mansonii* EDTA trisodium salt hydrate, $\geq$ 96% Filipin III from *S. filipinensis*	Sigma-Aldrich Chemie GmbH, Steinheim, Germany
Histosec pastilles (paraffin)	Merck KgaA, Darmstadt, Germany
Hydrocortisone, BioReagent	Sigma-Aldrich Chemie GmbH, Steinheim, Germany
Iron(III) chloride hexahydrate	Merck KgaA, Darmstadt, Germany
N-Formyl-Met-Leu-Phe (fMLP), $\geq$97% PMA, $\geq$96% (TLC)	Sigma-Aldrich Chemie GmbH, Steinheim, Germany
Potassium ferrocyanide trihydrate	ICN Biomedicals GmbH, Eschwege, Germany
rh IL-1β rh IL-8 / 1-77a.a. rh MCP-1 / CCL2 rh MIP-1α / CCL3 rh TNF-α	ImmunoTools GmbH, Friesoythe, Germany
Trichloroacetic acid, $\geq$99%	Carl Roth GmbH & Co. KG, Karlsruhe, Germany

Table A.2: List of used reagents and media.

Reagent/Medium	**Supplier**
20× reducing agent 20× XT MES running buffer 4× XT sample buffer	Bio-Rad Laboratories, Inc., Hercules, USA
Acetic acid	Sigma-Aldrich Chemie GmbH, Steinheim, Germany
BD FACS Flow™ Sheath Fluid BD FACS™ Clean Solution BD FACS™ Rinse Solution	BD Biosciences, Singapore
Biozidal ZF™	WAK - Chemie Medical GmbH, Steinbach, Germany
Coulter Isoton II	Beckman Coulter GmbH, Krefeld, Germany
D-PBS	Thermo Fisher Scientific Inc., Waltham, USA
DiffQuick solution II	Medion Diagnostics GmbH, Düdingen
Dimethyl sulfoxide	Sigma-Aldrich Chemie GmbH, Steinheim, Germany
Disinfection Softasept® N	B. Braun Melsungen AG, Melsungen, Germany
HCl, 32%	Carl Roth GmbH & Co. KG, Karlsruhe, Germany
DMEM /HAM's F12 DMEM + GlutaMAX™ Entellan® New	Thermo Fisher Scientific Inc., Waltham, USA Merck KgaA, Darmstadt, Germany
Ethanol denatured	Carl Roth GmbH & Co. KG, Karlsruhe, Germany
FBS (*also denoted as FCS*)	Biochrom GmbH, Berlin, Germany
Formalin, neutral buffered, 10%	Sigma-Aldrich Chemie GmbH, Steinheim, Germany
Giemsa's azur eosin methylene blue	Merck KgaA, Darmstadt, Germany
HCl, 37%	Sigma-Aldrich Chemie GmbH, Steinheim, Germany
HyClone™ HyQTase™	GE Healthcare Life Sciences, Little Chalfont, UK
Kaleidoscope Precision Plus Protein standards	Bio-Rad Laboratories, Inc., Hercules, USA

Reagent/Medium	Supplier
May-Grünwald's eosine-methylene blue	Merck KgaA, Darmstadt, Germany
Methanol HiPerSolv CHROMANORM®	VWR International, Radnor, USA
Nuclear Fast Red solution	Sigma-Aldrich Chemie GmbH, Steinheim, Germany
Penicillin-Streptomycin (10,000 U/ml)	Thermo Fisher Scientific Inc., Waltham, USA
PrestoBlue™ cell viability Reagent	Thermo Fisher Scientific Inc., Waltham, USA
RPMI 1640 + GlutaMAX™	
RPMI 1640, no phenol red	
Shandon™ Immu-Mount™	
Triton™ X-100	Sigma-Aldrich Chemie GmbH, Steinheim, Germany
Trypsin-EDTA (0.05%)	Thermo Fisher Scientific Inc., Waltham, USA
Xylene	Carl Roth GmbH & Co. KG, Karlsruhe, Germany

Table A.3: List of used fluorescent dyes and antibodies.

Antibody/Dye	Supplier
α-rabbit IgG, Alexa Fluor® 488 conjugate (goat)	Cell Signaling Technology Inc., Danvers, USA
α-ZO-1 antibody (rabbit)	Thermo Fisher Scientific Inc., Waltham, USA
Alexa Fluor® 633 phalloidin	
CellTracker™ Green BODIPY ® Dye	
CellTracker™ Red CMTPX Dye	
CompBeads Plus BD™ α-Mouse Ig, κ	BD Biosciences, Singapore
CD11b/Mac-1-APC, α-Human (mouse IgG1, κ)	
CD13-FITC (mouse IgG1)	Immunotech Inc., Quebec, Canada
CD14-PE (Mϕ P9) (mouse IgG2, κ)	BD Biosciences, Singapore
CD16-PE Mouse α-Human (mouse IgG1, κ)	
CD34-FITC Mouse α-Human (mouse IgG1, κ)	

Antibody/Dye	**Supplier**
CD40-PE (mouse IgG1, κ)	Immunotech Inc., Quebec, Canada
DAPI I counterstain (1,000 ng/ml)	Abbott GmbH & Co. KG, Wiesbaden, Germany
Fluorescein sodium salt	Sigma-Aldrich Chemie GmbH, Steinheim, Germany
Hoechst 33258, Pentahydrate 10 mg/ml SYTOX® Red Dead Cell Stain	Thermo Fisher Scientific Inc., Waltham, USA

Table A.4: List of used consumables.

Consumable	**Supplier**
CELLSTAR® Cell culture flask (25, 75, 175 cm^2) CELLSTAR® Multiwell plate (6, 12, 24 wells)	Greiner Bio-One GmbH, Frickenhausen, Germany
ceramic scalpel, 20mm, anti-magnetic, form 34	VWR International, Radnor, USA
Cover slips, Menzel glass, round (12 mm)	Thermo Fisher Scientific Inc., Waltham, USA
Criterion™ XT precast gel, 4-12% Bis-Tris	Bio-Rad Laboratories, Inc., Hercules, USA
Cytospin adapters for glass slides Cytospin filters	Andreas Hettich GmbH & Co. KG, Tuttingen, Germany
Embedding cassettes	Carl Roth GmbH & Co. KG, Karlsruhe, Germany
FACS tubes, polystyrene, round bottom, 5 ml	Corning Inc. Life Sciences, Corning, USA
gentleMACS™ M Tubes	Miltenyi Biotec GmbH, Bergisch Gladbach, Germany
HaemoDiff® with smear rim	Sarstedt AG & Co., Nümbrecht, Germany
MicroAmp® Fast Reaction Tube with Cap, 0.1ml	Thermo Fisher Scientific Inc., Waltham, USA
Microplate, 96 wells, PS, F-bottom, µ-Clear®	Greiner Bio-One GmbH, Frickenhausen, Germany
Microtome blade R35	pfm medical, Köln, Germany
Nalgene syringe filter, SFCA, 0.2 µm Polysine™ microscopic adhesion slides	Thermo Fisher Scientific Inc., Waltham, USA

Consumable	Supplier
PP conic sample vials, 3 ml	Analytik Jena AG, Jena, Germany
Symex SP slides	Sysmex Deutschland GmbH, Norderstedt, Germany
Transwell FluoroBlock™ 24 well companion plate Transwell FluoroBlock™ 24 well inserts, PET, 3.0 µm Transwell® 24 well inserts, PET, tissue culture-treated, 3.0 µm Transwell® 24 well insert, PTFE, collagen-coated, 3.0 µm	Corning Inc. Life Sciences, Corning, USA

Table A.5: List of used technical devices and instruments.

Instrument	Supplier
Axiovert 25 inverse microscope Axioplan 2 imaging microscope AxioCAM HRC	Carl Zeiss Microscopy GmbH, Jena, Germany
Cell Coulter	Beckman Coulter GmbH, Krefeld, Germany
Centrifuge 5417C Centrifuge 5810R	Eppendorf AG, Hamburg, Germany
Chop stick electrodes STX2	World Precision Instruments, Sarasota, USA
Criterion™ Vertical Electrophoresis Cell	Bio-Rad Laboratories, Inc., Hercules, USA
Cytospin Rotofix 32	Andreas Hettich GmbH & Co. KG, Tuttlingen, Germany
Dry cabinet, Dry-Line®	VWR International, Radnor, USA
Epithelial voltohmmeter EVOM2	World Precision Instruments, Sarasota, USA
gentleMACS™ dissociator	Miltenyi Biotec GmbH, Bergisch Gladbach, Germany
Incubator HERAcell 240i CO_2	Thermo Fisher Scientific Inc., Waltham, USA
Magnetic block NeoDeltaMagnet® (NdFeB), 100×100×15mm	IBS Magnet, Berlin, Germany
Magnetic 24-well plate MagnetoFACTOR	chemicell GmbH, Berlin, Germany

Instrument	**Supplier**
Milli-Q® Reference water purification system	Merck KgaA, Darmstadt, Germany
Orbital Shaker Incubator	GFL GmbH, Burgwedel, Germany
PowerPac 200 power supply	Bio-Rad Laboratories, Inc., Hercules, USA
Steril work bench HERAsafe® HS12/2	Thermo Fisher Scientific Inc., Waltham, USA
Thermomixer comfort	Eppendorf AG, Hamburg, Germany
Vacusafe	Integra Biosciences GmbH, Biebertal, Germany

APPENDIX B

Supplement

B.1 Incubation Conditions Influence the SPION-associated Protein Corona Formation

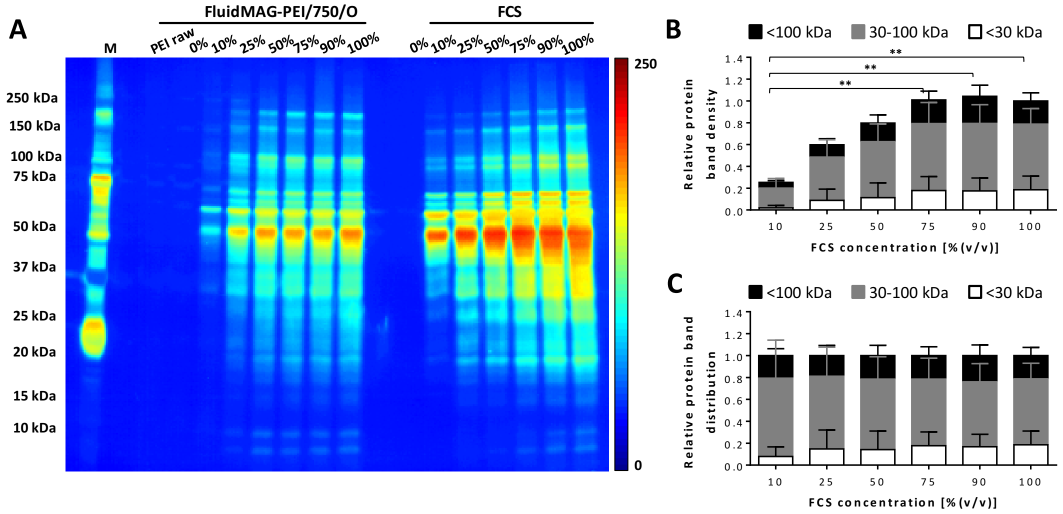

Figure B.1: Gel electrophoretic analysis of protein corona formation on SPIONs. FluidMAG-PEI incubated with indicated FCS concentrations were subjected to sodium dodecyl sulfate polyacrylamide gel electrophoresis. Corona-derived proteins were visualized by highly sensitive silver staining. Lanes 3–10 comprise protein bands derived from particles, lanes 12–18 show protein bands of respective FCS solutions prior to particle incubation. **A** Image presented in alternative color mapping with low intensities depicted in blue and high intensities in red. Optical density measurements of protein bands of low (<30 kDa), medium (30–100 kDa), and high (>100 kDa) molecular weight are shown relative to 100% FCS-treated lanes (**B**) as well as their distribution within respective lanes (**C**). Statistical significance of indicated total optical mean densities were tested by one-way ANOVA followed by Tuckey's multiple comparison. Differences are considered as statistically significant for $p < 0.01$(**). Figure taken with permission and data extended from [157]. FCS - fetal calf serum; M - protein standard marker; PEI - polyethylenimine.

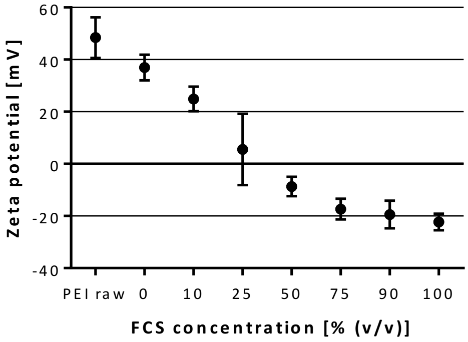

Figure B.2: Zeta potential measurements of SPIONs with diverse protein coronas. FluidMAG-PEI incubated with indicated concentrations of FCS [% (v/v)] were subjected to zeta potential measurements. Figure taken with permission from [157]. FCS - fetal calf serum; PEI - polyethylenimine.

B.2 SPION-associated Cytotoxicity Depends on Proliferative State

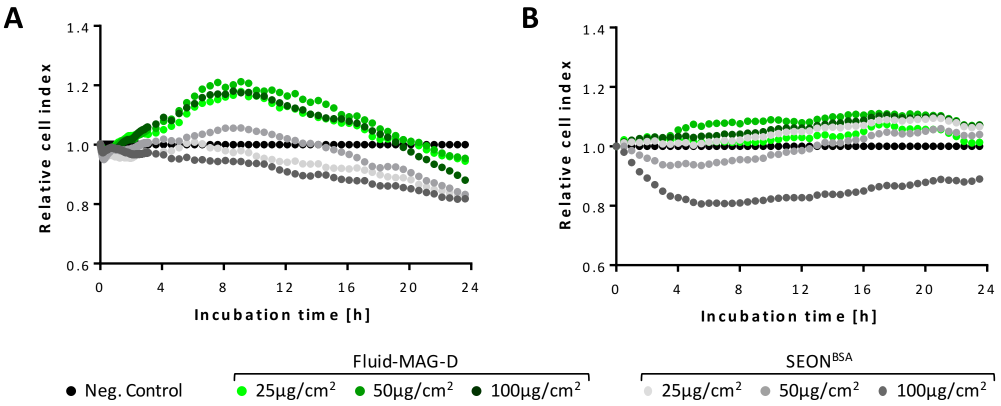

Figure B.3: Real-time cell analysis of HBMEC exposed to SPIONs. HBMEC were seeded into 16-well plates in duplicates with a seeding density of 10,000 cells/well. After 24 h (**A**) or 48 h (**B**) SPIONs were added during the proliferative log phase or stationary phase of confluent layers resulting in final concentrations of 25–100 µg/cm^2 (corresponding to 25–100 µg/ml). Negative controls were treated with *aqua bidest.*. Shown are means of one representative of two independent experiments with two replicates each.

B.3 Cationic SPIONs barely Pass Transwell Membranes

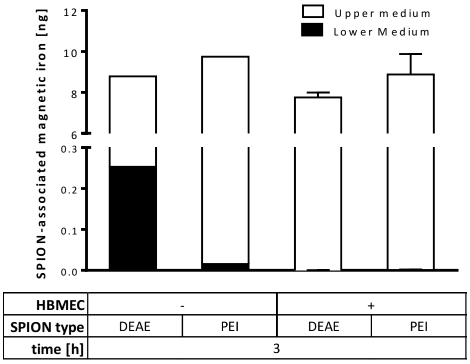

Figure B.4: Analysis of membrane passage of cationic SPIONs by magnetic particle spectroscopy (MPS). HBMEC were seeded on transwell inserts and cultured for five days. DEAE- or PEI-coated SPIONs were added resulting in a final concentration of 100 µg/cm^2 (corresponding to 200 µg/ml) and incubated for 3 h, whereby the first 30 min were carried out on top of a block magnet. Distinct compartments were sampled and analyzed for magnetic iron contents by MPS. Shown are means ± standard deviation of three independent experiments with three replicate inserts each. DEAE - diethylamine ethyl; PEI - polyethylenimine.

B.4 Endocytosis Inhibitors Affect Barrier Integrity

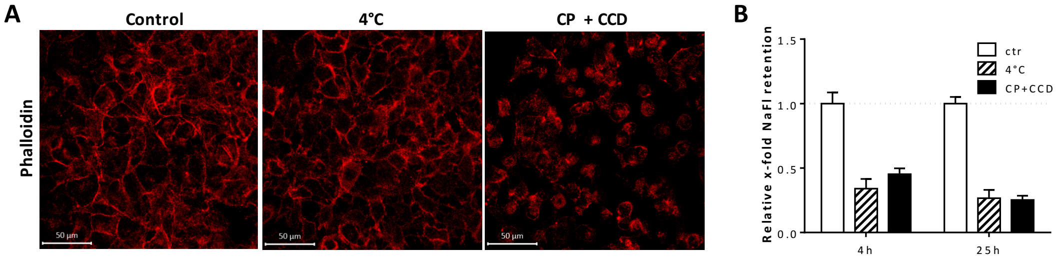

Figure B.5: Analysis of cell layer integrity under the influence of endocytosis inhibitors. HBMEC were seeded on transwell inserts and cultured for five days. Endocytosis inhibitors comprising 4 °C or chlorpromazine (CP) and cytochalasin D (CCD) were applied for 4-25 h. **A** Cells incubated for 25 h were fixed, stained using Alexa Fluor® 633 Phalloidin (red), and analyzed by confocal laser scanning microscopy. **B** Molecular restraint of cell layers to sodium fluorescein (NaFl) upon dye incubation for 10 min relative to control cells. Shown are means of two independent experiments with two replicate transwell inserts each.

B.5 SPION-induced Passage of Immune Cells trough Blood-Brain Barrier Model

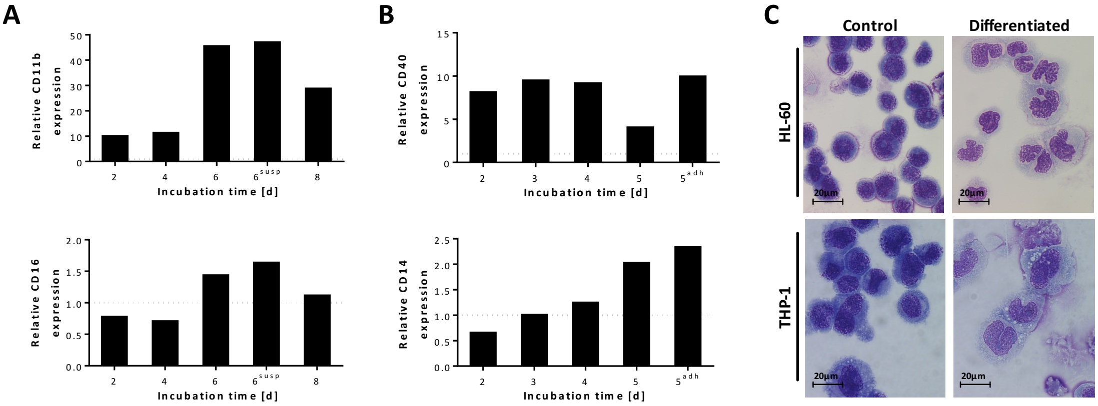

Figure B.6: Analysis of differentiation of HL-60 and THP-1 by flow cytometry and microscopic investigation. HL-60 were differentiated for six days using 1.4% DMSO, whereas THP-1 were treated with 5 ng/ml PMA for five days to obtain monocytic cells. **A** Time-dependent neutrophilic surface marker expression of differentiated HL-60 analyzed by flow cytometry. **B** Time-dependent monocytic surface marker expression of differentiated THP-1 analyzed by flow cytometry. **C** Pappenheim-stained smear preparations of HL-60 and THP-1 at day six and five, respectively. DMSO - dimethyl sulfoxide; PMA - phorbol 12-myristate 13-acetate.

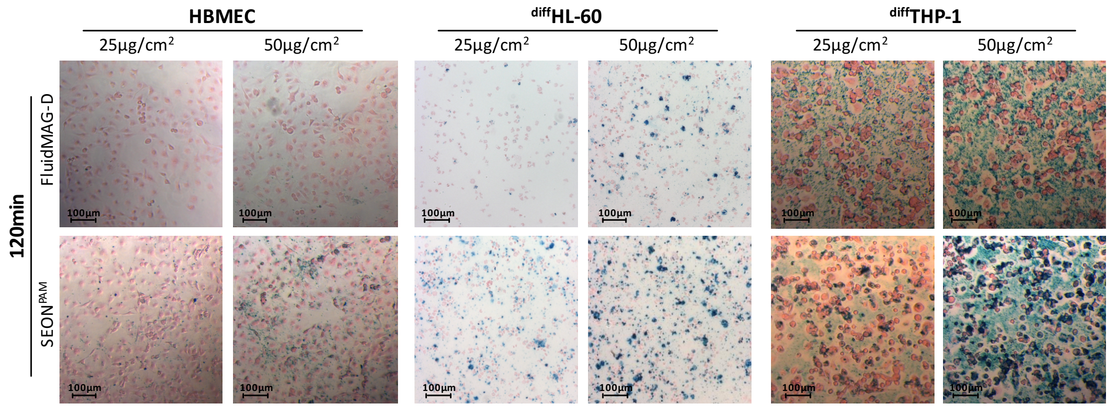

Figure B.7: Cellular interaction of diverse types of SPIONs with HBMEC and differentiated HL-60 and THP-1. HBMEC, differentiated HL-60 ($^{\text{diff}}$HL-60), and differentiated THP-1 ($^{\text{diff}}$THP-1) were seeded into 96-well plates with a seeding density of 15,000, cells/well 60,000 cells/well, and 120,000 cells/well, respectively. Cells were exposed to indicated SPION types in final concentrations of 25 µg/cm^2 or 50 µg/cm^2 (corresponding to 94.5 µg/ml or 189 µg/ml). Upon incubation for 120 min cells were washed, fixed and stained using Nuclear Fast Red. Additionally, SPIONs were stained by Prussian blue. PAM - polyacrylat-co-maleat.

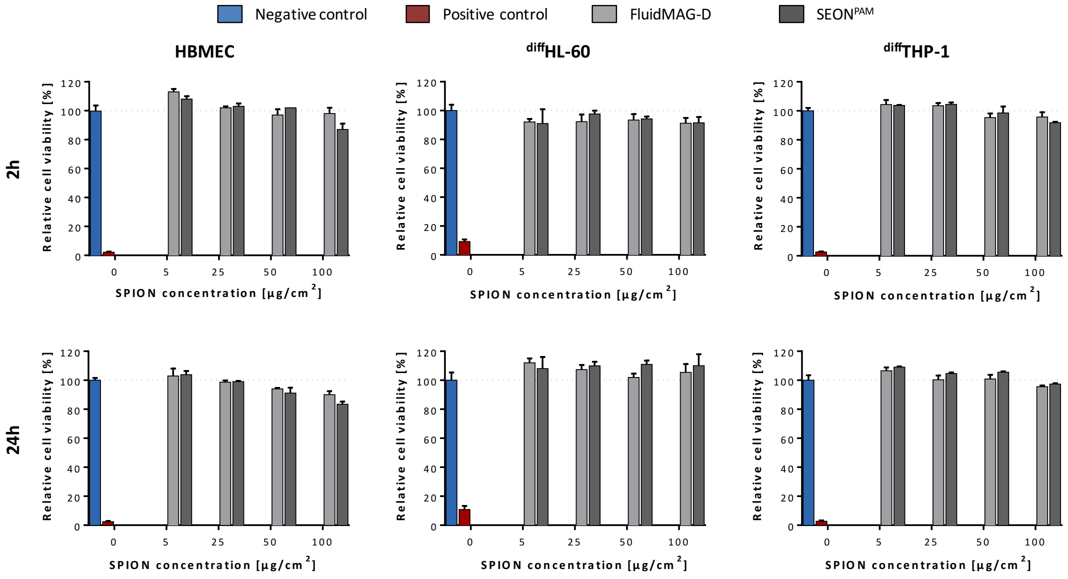

Figure B.8: PrestoBlue™ cell viability assays of HBMEC and differentiated HL-60 and THP-1 exposed to diverse types of SPIONs. HBMEC, differentiated HL-60 ($^{\text{diff}}$HL-60), and differentiated THP-1 ($^{\text{diff}}$THP-1) were seeded into 96-well plates in triplicates with a seeding density of 15,000, cells/well 60,000 cells/well, and 120,000 cells/well, respectively. Cells were exposed to indicated SPION types in final concentrations of 5–100 µg/cm^2 (corresponding to 19–378 µg/ml). Negative and positive control cells were treated with *aqua bidest.* or 0.02% triton X-100 final concentration analogously. Upon incubation for 3 h and 24 h PrestoBlue™ assays were performed. Shown are weighted means ± standard deviation of two to four independent experiments. PAM - polyacrylat-co-maleat.

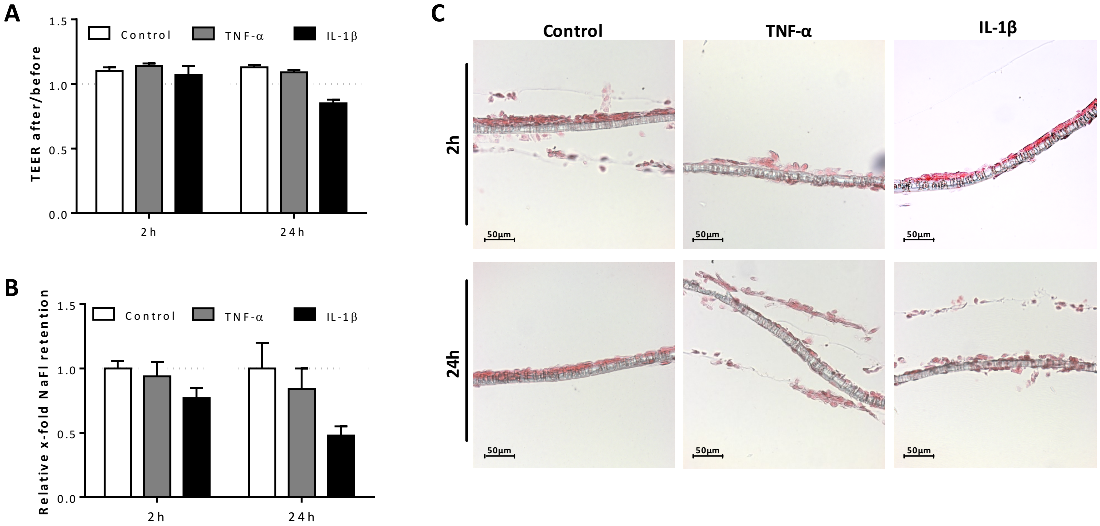

Figure B.9: Analysis of cell layer integrity under the influence of inflammatory cytokines. HBMEC were seeded on transwell inserts and cultured for five days. Inflammatory cytokines comprising TNF-*α* (2 ng/ml) or IL-1*β* (5 ng/ml) were applied for 2–24 h. **A** Transendothelial electrical resistance (TEER) measurements before and after cytokine incubation relative to control cells. **B** Molecular restraint of cell layers to sodium fluorescein (NaFl) upon dye incubation for 10 min relative to control cells. Shown are means of two independent experiments with two replicate transwell inserts each. **C** Nuclear Fast Red-stained histological cross sections of HBMEC layers after indicated treatment.

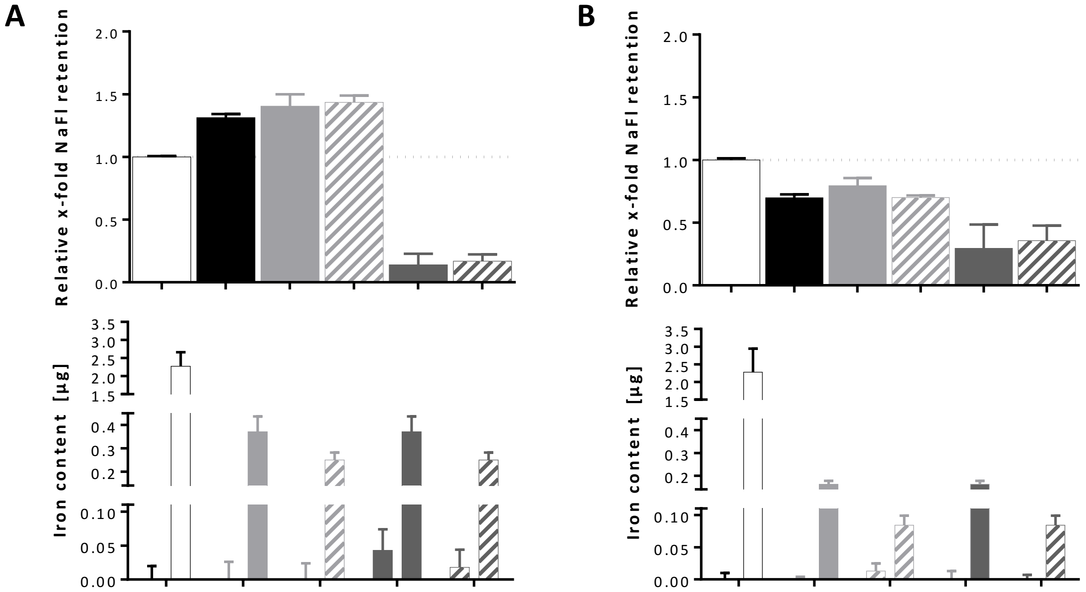

IL-1β	-		-		-		+		+	
SEON^{PAM}	(+)		+		+		+		+	
fMLP	-		-		+		+		+	
MF	-		-		+		-		+	
HBMEC	+	-	+	-	+	-	+	-	+	-

IL-1β	-		-		-		+		+	
SEON^{PAM}	(+)		+		+		+		+	
MCP-1	-		-		+		+		+	
MF	-		-		+		-		+	
HBMEC	+	-	+	-	+	-	+	-	+	-

Figure B.10: Barrier integrity of cell layers and iron content of lower acceptor compartments after passage of differentiated HL-60 and THP-1. HL-60 (**A**) and THP-1 (**B**) differentiated with 1.4% DMSO (six days) and 5 ng/ml PMA (five days), respectively, and loaded with 50 µg/cm^2 (corresponding to 189 µg/ml) of SEON^{PAM} for 120 min. Transmigration of 500,000 HL-60/insert or 300,000 THP-1/insert through transwell membranes seeded with HBMEC (+) or not (-) was performed for 1,400 min. If indicated, HBMEC layers were pre-treated with 5 ng/ml IL-1*β* for 120 min before SPION-loaded immune cells were added. Chemical attraction of HL-60 and THP-1 was induced by 10 nM fMLP or 100 ng/ml MCP-1 as indicated. For selected samples the first 30 min of incubation time were carried out on top of a 24-well magnetic plate (indicated as "MF"). After transmigration molecular retention of sodium fluorescein (NaFl) of HBMEC layers was tested. Additionally, total iron contents of lower acceptor media compartments were determined by atomic absorption spectroscopy. DMSO - dimethyl sulfoxide; fMLP - N-Formylmethionyl-leucyl-phenylalanine; MCP-1 - Monocyte chemoattractant protein-1; MF - magnetic field; PAM - polyacrylat-co-maleat; PMA - phorbol 12-myristate 13-acetate.

References

[1] I. Freestone, N. Meeks, M. Sax, and C. Higgitt, “The Lycurgus Cup — A Roman nanotechnology,” Gold Bulletin **40**, 270 (2007).

[2] S. Pérez-Villar, J. Rubio, and J. L. Oteo, “Study of color and structural changes in silver painted medieval glasses,” Journal of Non-Crystalline Solids **354**, 1833 (2008).

[3] J. Pérez-Arantegui, J. Molera, A. Larrea, T. Pradell, M. Vendrell-Saz, I. Borgia, *et al.*, “Luster Pottery from the Thirteenth Century to the Sixteenth Century: A Nanostructured Thin Metallic Film,” Journal of the American Ceramic Society **84**, 442 (2001).

[4] S. Padovani, C. Sada, P. Mazzoldi, B. Brunetti, I. Borgia, A. Sgamellotti, A. Giulivi, *et al.*, “Copper in glazes of Renaissance luster pottery: Nanoparticles, ions, and local environment,” Journal of Applied Physics **93**, 10058 (2003).

[5] M. Reibold, P. Paufler, A. A. Levin, W. Kochmann, N. Patzke, and D. C. Meyer, “Materials: Carbon nanotubes in an ancient Damascus sabre,” Nature **444**, 286 (2006).

[6] D. A. Jefferson, “The surface activity of ultrafine particles,” Philosophical Transactions of the Royal Society of London A: Mathematical, Physical and Engineering Sciences **358**, 2683 (2000).

[7] H. Su, Y. Wang, Y. Gu, L. Bowman, J. Zhao, and M. Ding, “Potential applications and human biosafety of nanomaterials used in nanomedicine,” Journal of Applied Toxicology n/a–n/a, jAT-17-0101.R1 (2017).

[8] M. Zaman, E. Ahmad, A. Qadeer, G. Rabbani, and R. H. Khan, “Nanoparticles in relation to peptide and protein aggregation,” International Journal of Nanomedicine **9**, 899 (2014).

[9] S. Horikoshi and N. Serpone, *Introduction to Nanoparticles*, 1–24, Wiley-VCH Verlag GmbH & Co. KGaA (2013).

[10] B. Pelaz, C. Alexiou, R. A. Alvarez-Puebla, F. Alves, A. M. Andrews, S. Ashraf, L. P. Balogh, *et al.*, “Diverse Applications of Nanomedicine,” ACS Nano **11**, 2313 (2017).

[11] "Nanotechnologies – Vocabulary – Part2: Nano-objects," Iso/ts 80004-2:2015(en), International Organization of Standardization, Geneva, Switzerland (2015).

[12] M. L. Etheridge, S. A. Campbell, A. G. Erdman, C. L. Haynes, S. M. Wolf, and J. McCullough, "The big picture on nanomedicine: the state of investigational and approved nanomedicine products," Nanomedicine: Nanotechnology, Biology and Medicine **9**, 1 (2013).

[13] C. A. Schütz, L. Juillerat-Jeanneret, H. Mueller, I. Lynch, and M. Riediker, "Therapeutic nanoparticles in clinics and under clinical evaluation," Nanomedicine **8**, 449 (2013).

[14] European Medicines Agency, "Nanotechnology," `http://www.ema.europa.eu/ema/index.jsp?curl=pages/special_topics/general/general_content_000345.jsp&mid=WC0b01ac05800baed9` (August 2017).

[15] R. D. Handy, R. Owen, and E. Valsami-Jones, "The ecotoxicology of nanoparticles and nanomaterials: current status, knowledge gaps, challenges, and future needs," Ecotoxicology **17**, 315 (2008).

[16] P. Kumar, L. Pirjola, M. Ketzel, and R. M. Harrison, "Nanoparticle emissions from 11 non-vehicle exhaust sources – A review," Atmospheric Environment **67**, 252 (2013).

[17] T. Benn, B. Cavanagh, K. Hristovski, J. D. Posner, and P. Westerhoff, "Journal of Environmental Quality," **39**, 1875 (2010).

[18] T. G. Smijs and S. Pavel, "Titanium dioxide and zinc oxide nanoparticles in sunscreens: focus on their safety and effectiveness," Nanotechnology, Science and Applications **4**, 95 (2011).

[19] A. S. Wu and T.-W. Chou, "Carbon nanotube fibers for advanced composites," Materials Today **15**, 302 (2012).

[20] C. K. Chan, H. Peng, G. Liu, K. McIlwrath, X. F. Zhang, R. A. Huggins, and Y. Cui, "High-performance lithium battery anodes using silicon nanowires," Nature Nanotechnology **3**, 31 (2008).

[21] L. Y. T. Chou, K. Ming, and W. C. W. Chan, "Strategies for the intracellular delivery of nanoparticles," Chemical Society Reviews **40**, 233 (2011).

[22] S. Onoue, S. Yamada, and H. K. Chan, "Nanodrugs: pharmacokinetics and safety," International Journal of Nanomedicine **9**, 1025 (2014).

[23] Y. Matsumura and H. Maeda, "A New Concept for Macromolecular Therapeutics in Cancer Chemotherapy: Mechanism of Tumoritropic Accumulation of Proteins and the Antitumor Agent Smancs," Cancer Research **46**, 6387 (1986).

[24] R. Bazak, M. Houri, S. El Achy, S. Kamel, and T. Refaat, “Cancer active targeting by nanoparticles: a comprehensive review of literature,” Journal of Cancer Research and Clinical Oncology **141**, 769 (2015).

[25] C. W. Noorlander, M. W. Kooi, A. G. Oomen, M. V. Park, R. J. Vandebriel, and R. E. Geertsma, “Horizon scan of nanomedicinal products,” Nanomedicine **10**, 1599 (2015).

[26] European Medicines Agency, “Abraxane (paclitaxel),” `http://www.ema.europa.eu/ema/index.jsp?curl=pages/medicines/human/medicines/000778/human_med_000620.jsp&mid=WC0b01ac058001d124` (August 2017).

[27] ClinicalTrials.gov, “AuroShell (Identification no. NCT02680535),” `https://www.clinicaltrials.gov/ct2/show/NCT02680535?term=auroshell&recrs=a&rank=1` (August 2017).

[28] S. Zaidi, L. Misba, and A. U. Khan, “Nano-therapeutics: A revolution in infection control in post antibiotic era,” Nanomedicine: Nanotechnology, Biology and Medicine – (2017).

[29] C. D. Chin, V. Linder, and S. K. Sia, “Commercialization of microfluidic point-of-care diagnostic devices,” Lab on a Chip **12**, 2118 (2012).

[30] F. Gorjikhah, S. Davaran, R. Salehi, M. Bakhtiari, A. Hasanzadeh, Y. Panahi, *et al.*, “Improving "lab-on-a-chip” techniques using biomedical nanotechnology: a review,” Artificial Cells, Nanomedicine, and Biotechnology **44**, 1609 (2016).

[31] N. Vanden Bon, B. van Grinsven, M. S. Murib, W. S. Yeap, K. Haenen, W. De Ceuninck, P. Wagner, *et al.*, “Heat-transfer-based detection of SNPs in the PAH gene of PKU patients,” International Journal of Nanomedicine **9**, 1629 (2014).

[32] European Medicines Agency, “nanocolloidal technetium (99mTc) albumin,” `http://www.ema.europa.eu/ema/index.jsp?curl=pages/regulation/general/general_content_001195.jsp&mid=WC0b01ac058029a224` (August 2017).

[33] E. Piktel, K. Niemirowicz, M. Wątek, T. Wollny, P. Deptuła, and R. Bucki, “Recent insights in nanotechnology-based drugs and formulations designed for effective anti-cancer therapy,” Journal of Nanobiotechnology **14**, 39 (2016).

[34] C. P. Bean and J. D. Livingston, “Superparamagnetism,” Journal of Applied Physics **30**, S120 (1959).

[35] D. Caruntu, G. Caruntu, and C. J. O'Connor, "Magnetic properties of variable-sized Fe3O4 nanoparticles synthesized from non-aqueous homogeneous solutions of polyols," Journal of Physics D: Applied Physics **40**, 5801 (2007).

[36] Y. Qiang, J. Antony, A. Sharma, J. Nutting, D. Sikes, and D. Meyer, "Iron/iron oxide core-shell nanoclusters for biomedical applications," Journal of Nanoparticle Research **8**, 489 (2006).

[37] B. Blasiak, F. C. J. M. van Veggel, and B. Tomanek, "Applications of Nanoparticles for MRI Cancer Diagnosis and Therapy," Journal of Nanomaterials **2013**, 148578 (2013).

[38] N. Singh, G. J. Jenkins, R. Asadi, and S. H. Doak, "Potential toxicity of superparamagnetic iron oxide nanoparticles (SPION)," Nano Reviews **1**, 5358 (2010).

[39] L. Kautz and E. Nemeth, "Molecular liaisons between erythropoiesis and iron metabolism," Blood **124**, 479 (2014).

[40] M. Worwood, B. J. Bain, and I. Bates, *Chapter 7 - Iron deficiency anaemia and iron overload A2 - Lewis, S. Mitchell*, 131–160, Churchill Livingstone, Philadelphia (2006).

[41] P. B. Santhosh and N. P. Ulrih, "Multifunctional superparamagnetic iron oxide nanoparticles: Promising tools in cancer theranostics," Cancer Letters **336**, 8 (2013).

[42] A. S. Wahajuddin, "Superparamagnetic iron oxide nanoparticles: magnetic nanoplatforms as drug carriers," International Journal of Nanomedicine **7**, 3445 (2012).

[43] M. Yu, S. Huang, K. J. Yu, and A. M. Clyne, "Dextran and Polymer Polyethylene Glycol (PEG) Coating Reduce Both 5 and 30 nm Iron Oxide Nanoparticle Cytotoxicity in 2D and 3D Cell Culture," International Journal of Molecular Sciences **13**, 5554 (2012).

[44] R. Alwi, S. Telenkov, A. Mandelis, T. Leshuk, F. Gu, S. Oladepo, and K. Michaelian, "Silica-coated super paramagnetic iron oxide nanoparticles (SPION) as biocompatible contrast agent in biomedical photoacoustics," Biomedical Optics Express **3**, 2500 (2012).

[45] S. Laurent, S. Dutz, U. O. Häfeli, and M. Mahmoudi, "Magnetic fluid hyperthermia: Focus on superparamagnetic iron oxide nanoparticles," Advances in Colloid and Interface Science **166**, 8 (2011).

[46] M. Shevtov and G. Multhoff, "Recent Developments of Magnetic Nanoparticles for Theranostics of Brain Tumor," Current Drug Metabolism **17**, 737 (2016).

[47] MagForce Nanotechnologies AG, "MagForce Nanotechnologies AG receives European regulatory approval for its NanoCancer therapy," `http://www.magforce.de/en/presse-investoren/news-events/detail/article/magforce-nanotechnologies-ag-erhaelt-europaeische-zulassung-fuer-die-nano-krebsR-therapie.html` (August 2017).

[48] M. Angelakeris, "Magnetic nanoparticles: A multifunctional vehicle for modern theranostics," Biochimica et Biophysica Acta (BBA) - General Subjects **1861**, 1642 (2017).

[49] K. Hayashi, M. Nakamura, W. Sakamoto, T. Yogo, H. Miki, S. Ozaki, M. Abe, *et al.*, "Superparamagnetic Nanoparticle Clusters for Cancer Theranostics Combining Magnetic Resonance Imaging and Hyperthermia Treatment," Theranostics **3**, 366 (2013).

[50] C. S. Brazel and X. Huang, *The Cost of Optimal Drug Delivery: Reducing and Preventing the Burst Effect in Matrix Systems*, volume 879, 267–282, American Chemical Society (2004).

[51] M. Mahmoudi, A. Simchi, A. S. Milani, and P. Stroeve, "Cell toxicity of superparamagnetic iron oxide nanoparticles," Journal of Colloid and Interface Science **336**, 510 (2009).

[52] P. H. Hoet, I. Brüske-Hohlfeld, and O. V. Salata, "Nanoparticles –known and unknown health risks," Journal of Nanobiotechnology **2**, 12 (2004).

[53] J. Shi, P. W. Kantoff, R. Wooster, and O. C. Farokhzad, "Cancer nanomedicine: progress, challenges and opportunities," Nature Reviews Cancer **17**, 20 (2017).

[54] F. Kiessling, M. E. Mertens, J. Grimm, and T. Lammers, "Nanoparticles for Imaging: Top or Flop?" Radiology **273**, 10 (2014).

[55] I. Canton and G. Battaglia, "Endocytosis at the nanoscale," Chemical Society Reviews **41**, 2718 (2012).

[56] L. Treuel, X. Jiang, and G. U. Nienhaus, "New views on cellular uptake and trafficking of manufactured nanoparticles," Journal of The Royal Society Interface **10**, 20120939 (2013).

[57] A. Verma and F. Stellacci, "Effect of Surface Properties on Nanoparticle–Cell Interactions," Small **6**, 12 (2010).

[58] A. Aderem and D. M. Underhill, "Mechanisms of phagocytosis in macrophages," Annual Review of Immunology **17**, 593 (1999).

[59] H. Kettiger, A. Schipanski, P. Wick, and J. Huwyler, "Engineered nanomaterial uptake and tissue distribution: from cell to organism," International Journal of Nanomedicine **8**, 3255 (2013).

[60] B. Alberts, A. Johnson, J. Lewis, M. Raff, K. Roberts, and P. Walter, *Molecular Biology of the Cell*, chapter 13, 789–799, Garland Sciences, 5th edition (2007).

[61] H. Hillaireau and P. Couvreur, "Nanocarriers' entry into the cell: relevance to drug delivery," Cellular and Molecular Life Sciences **66**, 2873 (2009).

[62] R. Schauer, "Sialic acids and their role as biological masks," Trends in Biochemical Sciences **10**, 357 (1985).

[63] T. Yeung, G. E. Gilbert, J. Shi, J. Silvius, A. Kapus, and S. Grinstein, "Membrane Phosphatidylserine Regulates Surface Charge and Protein Localization," Science **319**, 210 (2008).

[64] S. D. Conner and S. L. Schmid, "Regulated portals of entry into the cell," Nature **422**, 37 (2003).

[65] N. Bohmer and A. Jordan, "Caveolin-1 and CDC42 mediated endocytosis of silica-coated iron oxide nanoparticles in HeLa cells," Beilstein Journal of Nanotechnology **6**, 167 (2015).

[66] T.-G. Iversen, T. Skotland, and K. Sandvig, "Endocytosis and intracellular transport of nanoparticles: Present knowledge and need for future studies," Nano Today **6**, 176 (2011).

[67] X. Jiang, A. Musyanovych, C. Rocker, K. Landfester, V. Mailander, and G. U. Nienhaus, "Specific effects of surface carboxyl groups on anionic polystyrene particles in their interactions with mesenchymal stem cells," Nanoscale **3**, 2028 (2011).

[68] G. Sahay, D. Y. Alakhova, and A. V. Kabanov, "Endocytosis of nanomedicines," Journal of Controlled Release **145**, 182 (2010).

[69] P. Sandin, L. W. Fitzpatrick, J. C. Simpson, and K. A. Dawson, "High-Speed Imaging of Rab Family Small GTPases Reveals Rare Events in Nanoparticle Trafficking in Living Cells," ACS Nano **6**, 1513 (2012).

[70] F. A. Cupaioli, F. A. Zucca, D. Boraschi, and L. Zecca, "Engineered nanoparticles. How brain friendly is this new guest?" Progress in Neurobiology **119**, 20 (2014).

[71] S. Guo and L. Huang, "Nanoparticles Escaping RES and Endosome: Challenges for siRNA Delivery for Cancer Therapy," Journal of Nanomaterials **2011**, 11:1 (2011).

[72] N. Oh and J.-H. Park, "Endocytosis and exocytosis of nanoparticles in mammalian cells," International Journal of Nanomedicine **9**, 51 (2014).

[73] K. Y. Win and S.-S. Feng, "Effects of particle size and surface coating on cellular uptake of polymeric nanoparticles for oral delivery of anticancer drugs," Biomaterials **26**, 2713 (2005).

[74] M. Mahmoudi, S. Laurent, M. A. Shokrgozar, and M. Hosseinkhani, "Toxicity Evaluations of Superparamagnetic Iron Oxide Nanoparticles: Cell "Vision" versus Physicochemical Properties of Nanoparticles," ACS Nano **5**, 7263 (2011).

[75] D. Fischer, Y. Li, B. Ahlemeyer, J. Krieglstein, and T. Kissel, "In vitro cytotoxicity testing of polycations: influence of polymer structure on cell viability and hemolysis," Biomaterials **24**, 1121 (2003).

[76] F. Marano, S. Hussain, F. Rodrigues-Lima, A. Baeza-Squiban, and S. Boland, "Nanoparticles: molecular targets and cell signalling," Archives of Toxicology **85**, 733 (2011).

[77] S. Hong, P. R. Leroueil, E. K. Janus, J. L. Peters, M.-M. Kober, M. T. Islam, B. G. Orr, *et al.*, "Interaction of Polycationic Polymers with Supported Lipid Bilayers and Cells: Nanoscale Hole Formation and Enhanced Membrane Permeability," Bioconjugate Chemistry **17**, 728 (2006).

[78] A. Villanueva, M. Cañete, A. G. Roca, M. Calero, S. Veintemillas-Verdaguer, C. J. Serna, *et al.*, "The influence of surface functionalization on the enhanced internalization of magnetic nanoparticles in cancer cells," Nanotechnology **20**, 115103 (2009).

[79] N. Ghinea and N. Simionescu, "Anionized and cationized hemeundecapeptides as probes for cell surface charge and permeability studies: differentiated labeling of endothelial plasmalemmal vesicles." The Journal of Cell Biology **100**, 606 (1985).

[80] M. Sajid, M. Ilyas, C. Basheer, M. Tariq, M. Daud, N. Baig, and F. Shehzad, "Impact of nanoparticles on human and environment: review of toxicity factors, exposures, control strategies, and future prospects," Environmental Science and Pollution Research **22**, 4122 (2015).

[81] C. C. Berry, S. Charles, S. Wells, M. J. Dalby, and A. S. Curtis, "The influence of transferrin stabilised magnetic nanoparticles on human dermal fibroblasts in culture," International Journal of Pharmaceutics **269**, 211 (2004).

[82] F. Braet, E. Wisse, P. Bomans, P. Frederik, W. Geerts, A. Koster, L. Soon, and S. Ringer, "Contribution of high-resolution correlative imaging techniques in the study of the liver sieve in three-dimensions," Microscopy Research and Technique **70**, 230 (2007).

[83] E. Blanco, H. Shen, and M. Ferrari, "Principles of nanoparticle design for overcoming biological barriers to drug delivery," Nature Biotechnology **33**, 941 (2015).

[84] S. Wohlfart, S. Gelperina, and J. Kreuter, "Transport of drugs across the blood–brain barrier by nanoparticles," Journal of Controlled Release **161**, 264 (2012).

[85] C. Chouly, D. Pouliquen, I. Lucet, J. J. Jeune, and P. Jallet, "Development of superparamagnetic nanoparticles for MRI: effect of particle size, charge and surface nature on biodistribution," Journal of Microencapsulation **13**, 245 (1996).

[86] F. Roohi, J. Lohrke, A. Ide, G. Schütz, and K. Dassler, "Studying the effect of particle size and coating type on the blood kinetics of superparamagnetic iron oxide nanoparticles," International Journal of Nanomedicine **7**, 4447 (2012).

[87] J. P. M. Almeida, A. L. Chen, A. Foster, and R. Drezek, "In vivo biodistribution of nanoparticles," Nanomedicine **6**, 815 (2011).

[88] M. Johannsen, U. Gneveckow, K. Taymoorian, B. Thiesen, N. Waldöfner, R. Scholz, K. Jung, *et al.*, "Morbidity and quality of life during thermotherapy using magnetic nanoparticles in locally recurrent prostate cancer: Results of a prospective phase I trial," International Journal of Hyperthermia **23**, 315 (2007).

[89] Y. Cheng, R. A. Morshed, B. Auffinger, A. L. Tobias, and M. S. Lesniak, "Multifunctional nanoparticles for brain tumor imaging and therapy," Advanced Drug Delivery Reviews **66**, 42 (2014).

[90] K. Prapainop, D. P. Witter, and P. Wentworth, "A Chemical Approach for Cell-Specific Targeting of Nanomaterials: Small-Molecule-Initiated Misfolding of Nanoparticle Corona Proteins," Journal of the American Chemical Society **134**, 4100 (2012).

[91] L. Vroman, "Effect of absorbed proteins on the wettability of hydrophilic and hydrophobic solids." Nature **196**, 476 (1962).

[92] J. Wolfram, Y. Yang, J. Shen, A. Moten, C. Chen, H. Shen, *et al.*, "The nanoplasma interface: Implications of the protein corona," Colloids and Surfaces B: Biointerfaces **124**, 17 (2014).

[93] M. Rahman, S. Laurent, N. Tawil, L. Yahia, and M. Mahmoudi, *Nanoparticle and Protein Corona*, 21–44, Springer Berlin Heidelberg, Berlin, Heidelberg (2013).

[94] C. D. Walkey and W. C. Chan, “Understanding and controlling the interaction of nanomaterials with proteins in a physiological environment,” Chemical Society Reviews **41**, 2780 (2012).

[95] M. Mahmoudi, S. Sheibani, A. S. Milani, F. Rezaee, M. Gauberti, R. Dinarvand, and H. Vali, “Crucial role of the protein corona for the specific targeting of nanoparticles,” Nanomedicine **10**, 215 (2015).

[96] S. Tenzer, D. Docter, S. Rosfa, A. Wlodarski, J. Kuharev, *et al.*, “Nanoparticle Size Is a Critical Physicochemical Determinant of the Human Blood Plasma Corona: A Comprehensive Quantitative Proteomic Analysis,” ACS Nano **5**, 7155 (2011).

[97] L. Landgraf, C. Christner, W. Storck, I. Schick, I. Krumbein, H. Dähring, K. Haedicke, *et al.*, “A plasma protein corona enhances the biocompatibility of Au@Fe3O4 Janus particles,” Biomaterials **68**, 77 (2015).

[98] D. Hühn, K. Kantner, C. Geidel, S. Brandholt, I. De Cock, S. J. H. Soenen, P. Rivera-Gil, *et al.*, “Polymer-Coated Nanoparticles Interacting with Proteins and Cells: Focusing on the Sign of the Net Charge,” ACS Nano **7**, 3253 (2013).

[99] N. J. Butcher, G. M. Mortimer, and R. F. Minchin, “Drug delivery: Unravelling the stealth effect,” Nature Nanotechnology **11**, 310 (2016).

[100] C. Corbo, R. Molinaro, A. Parodi, N. E. Toledano Furman, F. Salvatore, and E. Tasciotti, “The impact of nanoparticle protein corona on cytotoxicity, immunotoxicity and target drug delivery,” Nanomedicine **11**, 81 (2016).

[101] D. F. Rolfe and G. C. Brown, “Cellular energy utilization and molecular origin of standard metabolic rate in mammals,” Physiological Reviews **77**, 731 (1997).

[102] B. T. Hawkins and T. P. Davis, “The Blood-Brain Barrier/Neurovascular Unit in Health and Disease,” Pharmacological Reviews **57**, 173 (2005).

[103] Y. Takeshita and R. M. Ransohoff, “Inflammatory cell trafficking across the blood-brain barrier (BBB): Chemokine regulation and in vitro models,” Immunological Reviews **248**, 228 (2012).

[104] N. J. Abbott, L. Ronnback, and E. Hansson, “Astrocyte-endothelial interactions at the blood-brain barrier,” Nature Reviews Neuroscience **7**, 41 (2006).

[105] J. Bicker, G. Alves, A. Fortuna, and A. Falcão, “Blood–brain barrier models and their relevance for a successful development of CNS drug delivery systems: A review,” European Journal of Pharmaceutics and Biopharmaceutics **87**, 409 (2014).

[106] M. S. Balda and K. Matter, "The tight junction protein ZO-1 and an interacting transcription factor regulate ErbB-2 expression," The EMBO Journal **19**, 2024 (2000).

[107] K. K. Jain, "Nanobiotechnology-based strategies for crossing the blood–brain barrier," Nanomedicine **7**, 1225 (2012).

[108] B. Srinivasan, A. R. Kolli, M. B. Esch, H. E. Abaci, M. L. Shuler, and J. J. Hickman, "TEER Measurement Techniques for In Vitro Barrier Model Systems," Journal of Laboratory Automation **20**, 107 (2015).

[109] A. M. Butt, H. C. Jones, and N. J. Abbott, "Electrical resistance across the blood-brain barrier in anaesthetized rats: a developmental study." The Journal of Physiology **429**, 47 (1990).

[110] N. J. Abbott, A. A. K. Patabendige, D. E. M. Dolman, S. R. Yusof, and D. J. Begley, "Structure and function of the blood–brain barrier," Neurobiology of Disease **37**, 13 (2010).

[111] S. Hori, S. Ohtsuki, K.-I. Hosoya, E. Nakashima, and T. Terasaki, "A pericyte-derived angiopoietin-1 multimeric complex induces occludin gene expression in brain capillary endothelial cells through Tie-2 activation in vitro," Journal of Neurochemistry **89**, 503 (2004).

[112] E. Farkas and P. G. Luiten, "Cerebral microvascular pathology in aging and Alzheimer's disease," Progress in Neurobiology **64**, 575 (2001).

[113] L. He, K. Vasiliou, and D. W. Nebert, "Analysis and update of the human solute carrier (SLC) gene superfamily," Human Genomics **3**, 195 (2009).

[114] C. Fernandes, U. Soni, and V. Patravale, "Nano-interventions for neurodegenerative disorders," Pharmacological Research **62**, 166 (2010).

[115] D. S. Miller, "Regulation of ABC Transporters at the Blood-Brain Barrier," Clinical Pharmacology and Therapeutics **97**, 395 (2015).

[116] G. McCaffrey and T. P. Davis, "Physiology and pathophysiology of the blood-brain barrier: P-glycoprotein and occludin trafficking as therapeutic targets to optimize CNS drug delivery," Journal of Investigative Medicine **60**, 1131 (2012).

[117] N. D. Doolittle, M. E. Miner, W. A. Hall, T. Siegal, E. J. Hanson, E. Osztie, L. D. McAllister, *et al.*, "Safety and efficacy of a multicenter study using intraarterial chemotherapy in conjunction with osmotic opening of the blood-brain barrier for the treatment of patients with malignant brain tumors," Cancer **88**, 637 (2000).

---

[118] D. S. Hersh, A. S. Wadajkar, N. Roberts, J. G. Perez, N. P. Connolly, V. Frenkel, J. A. Winkles, *et al.*, "Evolving Drug Delivery Strategies to Overcome the Blood Brain Barrier," Current Pharmaceutical Design **22**, 1177 (2016).

[119] K. Hynynen, N. McDannold, N. Vykhodtseva, and F. A. Jolesz, "Noninvasive MR Imaging–guided Focal Opening of the Blood-Brain Barrier in Rabbits," Radiology **220**, 640 (2001).

[120] T. Simuni and H. Hurtig, *Parkinson's Disease: Diagnosis and Clinical Management*, chapter Levadopa: A Pharmacologic Miracle Four Decades Later, Demos Medical Publishing (2008).

[121] A. Schnyder and J. Huwyler, "Drug transport to brain with targeted liposomes," NeuroRX **2**, 99 (2005).

[122] M. W. Smith and M. Gumbleton, "Endocytosis at the blood–brain barrier: From basic understanding to drug delivery strategies," Journal of Drug Targeting **14**, 191 (2006).

[123] X.-H. Tian, X.-N. Lin, F. Wei, W. Feng, Z.-C. Huang, P. Wang, *et al.*, "Enhanced brain targeting of temozolomide in polysorbate-80 coated polybutylcyanoacrylate nanoparticles," International Journal of Nanomedicine **6**, 445 (2011).

[124] M. R. Choi, K. J. Stanton-Maxey, J. K. Stanley, C. S. Levin, R. Bardhan, D. Akin, S. Badve, *et al.*, "A cellular trojan horse for delivery of therapeutic nanoparticles into tumors," Nano Letters **7**, 3759 (2007).

[125] T. Bagci-Onder, W. Du, J.-L. Figueiredo, J. Martinez-Quintanilla, and K. Shah, "Targeting breast to brain metastatic tumours with death receptor ligand expressing therapeutic stem cells," Brain **138**, 1710 (2015).

[126] P. L. Bonate, "Animal models for studying transport across the blood-brain barrier," Journal of Neuroscience Methods **56**, 1 (1995).

[127] H. C. Helms, N. J. Abbott, M. Burek, R. Cecchelli, P.-O. Couraud, M. A. Deli, C. Förster, *et al.*, "In vitro models of the blood–brain barrier: An overview of commonly used brain endothelial cell culture models and guidelines for their use," Journal of Cerebral Blood Flow & Metabolism **36**, 862 (2016).

[128] W. M. Pardridge, J. Yang, J. Eisenberg, and W. W. Tourtellotte, "Isolation of intact capillaries and capillary plasma membranes from frozen human brain," Journal of Neuroscience Research **18**, 352 (1987).

[129] M. A. Deli, C. S. Ábrahám, Y. Kataoka, and M. Niwa, "Permeability Studies on In Vitro Blood–Brain Barrier Models: Physiology, Pathology, and Pharmacology," Cellular and Molecular Neurobiology **25**, 59 (2005).

[130] I. Wilhelm and I. A. Krizbai, “In Vitro Models of the Blood–Brain Barrier for the Study of Drug Delivery to the Brain,” Molecular Pharmaceutics **11**, 1949 (2014).

[131] D. E. Eigenmann, G. Xue, K. S. Kim, A. V. Moses, M. Hamburger, and M. Oufir, “Comparative study of four immortalized human brain capillary endothelial cell lines, hCMEC/D3, hBMEC, TY10, and BB19, and optimization of culture conditions, for an in vitro blood–brain barrier model for drug permeability studies,” Fluids and Barriers of the CNS **10**, 33 (2013).

[132] V. Siddharthan, Y. V. Kim, S. Liu, and K. S. Kim, “Human astrocytes/astrocyte-conditioned medium and shear stress enhance the barrier properties of human brain microvascular endothelial cells,” Brain Research **1147**, 39 (2007).

[133] J. Zaloga, C. Janko, J. Nowak, J. Matuszak, S. Knaup, D. Eberbeck, R. Tieze, *et al.*, “Development of a lauric acid/albumin hybrid iron oxide nanoparticle system with improved biocompatibility,” International Journal of Nanomedicine **9**, 4847 (2014).

[134] I. Tóth, E. Illés, R. A. Bauer, D. Nesztor, M. Szekeres, I. Zupkó, and E. Tombácz, “Designed Polyelectrolyte Shell on Magnetite Nanocore for Dilution-Resistant Biocompatible Magnetic Fluids,” Langmuir **28**, 16638 (2012).

[135] R. P. Friedrich, J. Zaloga, E. Schreiber, I. Tóth, E. Tombácz, S. Lyer, and C. Alexiou, “Tissue Plasminogen Activator Binding to Superparamagnetic Iron Oxide Nanoparticle—Covalent Versus Adsorptive Approach,” Nanoscale Research Letters **11**, 297 (2016).

[136] A. Weidner, C. Gräfe, M. von der Lühe, H. Remmer, J. H. Clement, D. Eberbeck, F. Ludwig, *et al.*, “Preparation of Core-Shell Hybrid Materials by Producing a Protein Corona Around Magnetic Nanoparticles,” Nanoscale Research Letters **10**, 282 (2015).

[137] M. F. Stins, J. Badger, and K. S. Kim, “Bacterial invasion and transcytosis in transfected human brain microvascular endothelial cells,” Microbial Pathogenesis **30**, 19 (2001).

[138] S. J. Collins, F. W. Ruscetti, R. E. Gallagher, and R. C. Gallo, “Terminal differentiation of human promyelocytic leukemia cells induced by dimethyl sulfoxide and other polar compounds,” Proceedings of the National Academy of Sciences **75**, 2458 (1978).

[139] K. M. Henkels, K. Frondorf, M. E. Gonzalez-Mejia, A. L. Doseff, and J. Gomez-Cambronero, “IL-8-induced neutrophil chemotaxis is mediated by Janus kinase 3 (JAK3),” FEBS Letters **585**, 159 (2011).

[140] A. Millius and O. D. Weiner, "Chemotaxis in Neutrophil-Like HL-60 Cells," Methods in Molecular Biology **571**, 167 (2009).

[141] E. K. Park, H. S. Jung, H. I. Yang, M. C. Yoo, C. Kim, and K. S. Kim, "Optimized THP-1 differentiation is required for the detection of responses to weak stimuli," Inflammation Research **56**, 45 (2007).

[142] M. Kaya and B. Ahishali, *Assessment of Permeability in Barrier Type of Endothelium in Brain Using Tracers: Evans Blue, Sodium Fluorescein, and Horseradish Peroxidase*, 369–382, Humana Press, Totowa, NJ (2011).

[143] K. L. Audus and R. T. Borchardt, "Characterization of an In Vitro Blood–Brain Barrier Model System for Studying Drug Transport and Metabolism," Pharmaceutical Research **3**, 81 (1986).

[144] T. Schlorf, M. Meincke, E. Kossel, C.-C. Glüer, O. Jansen, and R. Mentlein, "Biological Properties of Iron Oxide Nanoparticles for Cellular and Molecular Magnetic Resonance Imaging," International Journal of Molecular Sciences **12**, 12 (2011).

[145] N. Otsu, "A Threshold Selection Method from Gray-Level Histograms," IEEE Transactions on Systems, Man and Cybernetics **9**, 62 (1979).

[146] E. McNeil, C. T. Capaldo, and I. G. Macara, "Zonula Occludens-1 Function in the Assembly of Tight Junctions in Madin-Darby Canine Kidney Epithelial Cells," Molecular Biology of the Cell **17**, 1922 (2006).

[147] W. C. Poller, N. Löwa, F. Wiekhorst, M. Taupitz, S. Wagner, K. Möller, G. Baumann, *et al.*, "Magnetic Particle Spectroscopy Reveals Dynamic Changes in the Magnetic Behavior of Very Small Superparamagnetic Iron Oxide Nanoparticles During Cellular Uptake and Enables Determination of Cell-Labeling Efficacy," Journal of Biomedical Nanotechnology **12**, 337 (2016).

[148] C. Scharlach, H. Kratz, F. Wiekhorst, C. Warmuth, J. Schnorr, G. Genter, M. Ebert, *et al.*, "Synthesis of acid-stabilized iron oxide nanoparticles and comparison for targeting atherosclerotic plaques: Evaluation by MRI, quantitative MPS, and TEM alternative to ambiguous Prussian blue iron staining," Nanomedicine: Nanotechnology, Biology and Medicine **11**, 1085 (2015).

[149] C. Harms, A. L. Datwyler, F. Wiekhorst, L. Trahms, R. Lindquist, E. Schellenberger, S. Mueller, *et al.*, "Certain types of iron oxide nanoparticles are not suited to passively target inflammatory cells that infiltrate the brain in response to stroke," Journal of Cerebral Blood Flow & Metabolism **33**, 1 (2013).

[150] N. Löwa, F. Wiekhorst, S. Metzkow, A. Ludwig, and L. Trahms, "Magnetic Particle Spectroscopy for the Quantification of Magnetic Nanoparticles in Living Cells," Biomedical Engineering / Biomedizinische Technik (2013).

[151] C. Gräfe, I. Slabu, F. Wiekhorst, C. Bergemann, F. von Eggeling, A. Hochhaus, *et al.*, "Magnetic particle spectroscopy allows precise quantification of nanoparticles after passage through human brain microvascular endothelial cells," Physics in Medicine and Biology **61**, 3986 (2016).

[152] A. D. McNaught and A. Wilkinson, *Compendium of Chemical Terminology*, Blackwell Science, 2nd edition (1997).

[153] C. W. Dunnett, "A Multiple Comparison Procedure for Comparing Several Treatments with a Control," Journal of the American Statistical Association **50**, 1096 (1955).

[154] C. W. Dunnett, "New Tables for Multiple Comparisons with a Control," **20**, 482 (1964).

[155] J. W. Tukey, "Comparing Individual Means in the Analysis of Variance," **5**, 99 (1949).

[156] Z. Sidak, "Rectangular Confidence Regions for the Means of Multivariate Normal Distributions," Journal of the American Statistical Association **62**, 626 (1967).

[157] C. Gräfe, A. Weidner, M. v.d. Lühe, C. Bergemann, F. H. Schacher, J. H. Clement, and S. Dutz, "Intentional formation of a protein corona on nanoparticles: Serum concentration affects protein corona mass, surface charge, and nanoparticle–cell interaction," The International Journal of Biochemistry & Cell Biology **75**, 196 (2016).

[158] M. Dusinska, S. Boland, M. Saunders, L. Juillerat-Jeanneret, L. Tran, G. Pojana, A. Marcomini, *et al.*, "Towards an alternative testing strategy for nanomaterials used in nanomedicine: Lessons from NanoTEST," Nanotoxicology **9**, 118 (2015).

[159] F. Bähring, F. Schlenk, J. Wotschadlo, N. Buske, T. Liebert, C. Bergmann, T. Heinze, A. Hochhaus, *et al.*, "Suitability of Viability Assays for Testing Biological Effects of Coated Superparamagnetic Nanoparticles," IEEE Transactions on Magnetics **49**, 383 (2013).

[160] H. B. Altman, "The Three R's of Individualization: Reeducation, Responsibility, and Relevance*," Foreign Language Annals **6**, 206 (1972).

[161] S. K. Doke and S. C. Dhawale, "Alternatives to animal testing: A review," Saudi Pharmaceutical Journal **23**, 223 (2015).

[162] A. Kroll, C. Dierker, C. Rommel, D. Hahn, W. Wohlleben, C. Schulze-Isfort, C. Göbbert, *et al.*, "Cytotoxicity screening of 23 engineered nanomaterials using a test matrix of ten cell lines and three different assays," Particle and Fibre Toxicology **8**, 9 (2011).

[163] M. Mahmoudi, A. Simchi, M. Imani, A. S. Milani, and P. Stroeve, "An in vitro study of bare and poly(ethylene glycol)-co-fumarate-coated superparamagnetic iron oxide nanoparticles: a new toxicity identification procedure," Nanotechnology **20**, 225104 (2009).

[164] R. P. Friedrich, C. Janko, M. Poettler, P. Tripal, J. Zaloga, I. Cicha, S. Dürr, *et al.*, "Flow cytometry for intracellular SPION quantification: specificity and sensitivity in comparison with spectroscopic methods," International Journal of Nanomedicine **10**, 4185 (2015).

[165] Y. Ibuki and T. Toyooka, *Nanoparticle Uptake Measured by Flow Cytometry*, 157–166, Humana Press, Totowa, NJ (2012).

[166] R. M. Zucker and K. M. Daniel, *Detection of TiO2 Nanoparticles in Cells by Flow Cytometry*, 497–509, Humana Press, Totowa, NJ (2012).

[167] A. Saraste and K. Pulkki, "Morphologic and biochemical hallmarks of apoptosis," Cardiovascular Research **45**, 528 (2000).

[168] A. Abulrob, H. Sprong, P. V. B. En Henegouwen, and D. Stanimirovic, "The blood–brain barrier transmigrating single domain antibody: mechanisms of transport and antigenic epitopes in human brain endothelial cells," Journal of Neurochemistry **95**, 1201 (2005).

[169] M. G. Qaddoumi, H. J. Gukasyan, J. Davda, V. Labhasetwar, K.-J. Kim, and V. H. L. Lee, "Clathrin and caveolin-1 expression in primary pigmented rabbit conjunctival epithelial cells: role in PLGA nanoparticle endocytosis," Molecular Vision **9**, 559 (2003).

[170] G. Sahay, V. Gautam, R. Luxenhofer, and A. V. Kabanov, "The Utilization of Pathogen-Like Cellular Trafficking by Single Chain Block Copolymer," Biomaterials **31**, 1757 (2010).

[171] O. P. Perumal, R. Inapagolla, S. Kannan, and R. M. Kannan, "The effect of surface functionality on cellular trafficking of dendrimers," Biomaterials **29**, 3469 (2008).

[172] H. Thangavel, *Nanomedicine: Principles and Perspectives*, volume 1, chapter 2 - Nanobiology in Medicine, Springer New York Heidelberg Dordrecht London (2014).

[173] S. E. Stewart, S. C. Kondos, A. Y. Matthews, M. E. D'Angelo, M. A. Dunstone, J. C. Whisstock, *et al.*, "The Perforin Pore Facilitates the Delivery of Cationic Cargos," The Journal of Biological Chemistry **289**, 9172 (2014).

[174] M. Geiser, B. Rothen-Rutishauser, N. Kapp, S. Schürch, W. Kreyling, H. Schulz, M. Semmler, *et al.*, "Ultrafine Particles Cross Cellular Membranes by Nonphagocytic Mechanisms in Lungs and in Cultured Cells," Environmental Health Perspectives **113**, 1555 (2005).

[175] Y. Zhao, X. Sun, G. Zhang, B. G. Trewyn, I. I. Slowing, and V. S. Y. Lin, "Interaction of Mesoporous Silica Nanoparticles with Human Red Blood Cell Membranes: Size and Surface Effects," ACS Nano **5**, 1366 (2011).

[176] V. H. Nguyen and B.-J. Lee, "Protein corona: a new approach for nanomedicine design," International Journal of Nanomedicine **12**, 3137 (2017).

[177] A. Salvati, A. S. Pitek, M. P. Monopoli, K. Prapainop, F. B. Bombelli, D. R. Hristov, P. M. Kelly, *et al.*, "Transferrin-functionalized nanoparticles lose their targeting capabilities when a biomolecule corona adsorbs on the surface," Nature Nanotechnology **8**, 137 (2013).

[178] V. Mirshafiee, M. Mahmoudi, K. Lou, J. Cheng, and M. L. Kraft, "Protein Corona Significantly Reduces Active Targeting Yield," Chemical Communications **49**, 2557 (2013).

[179] F. Wang, L. Yu, M. P. Monopoli, P. Sandin, E. Mahon, A. Salvati, and K. A. Dawson, "The biomolecular corona is retained during nanoparticle uptake and protects the cells from the damage induced by cationic nanoparticles until degraded in the lysosomes," Nanomedicine: Nanotechnology, Biology and Medicine **9**, 1159 (2013).

[180] Molecular Probes Inc., "SYTOX Red Dead Cell Stain (MP 34859)," `https://www.thermofisher.com/order/catalog/product/S34859` (April 2006).

[181] O. Boussif, F. Lezoualc'h, M. A. Zanta, M. D. Mergny, D. Scherman, B. Demeneix, and J. P. Behr, "A versatile vector for gene and oligonucleotide transfer into cells in culture and in vivo: polyethylenimine." Proceedings of the National Academy of Sciences of the United States of America **92**, 7297 (1995).

[182] G. Caracciolo, L. Callipo, S. C. D. Sanctis, C. Cavaliere, D. Pozzi, and A. Laganà, "Surface adsorption of protein corona controls the cell internalization mechanism of DC-Chol–DOPE/DNA lipoplexes in serum," Biochimica et Biophysica Acta **1798**, 536 (2010).

[183] S. Dohgu, F. Takata, A. Yamauchi, S. Nakagawa, T. Egawa, M. Naito, T. Tsuruo, *et al.*, "Brain pericytes contribute to the induction and up-regulation of blood–brain barrier functions through transforming growth factor-β production," Brain Research **1038**, 208 (2005).

[184] K. Sobue, N. Yamamoto, K. Yoneda, M. E. Hodgson, K. Yamashiro, N. Tsuruoka, T. Tsuda, *et al.*, "Induction of blood–brain barrier properties in immortalized bovine brain endothelial cells by astrocytic factors," Neuroscience Research **35**, 155 (1999).

[185] The UniProt Consortium, "UniProt: the universal protein knowledgebase," `http://www.uniprot.org/help/publications` (April 2017).

[186] B. Huang, P. R. Krafft, Q. Ma, W. B. Rolland, B. Caner, T. Lekic, A. Manaenko, *et al.*, "Fibroblast growth factors preserve blood-brain barrier integrity through RhoA inhibition after intracerebral hemorrhage in mice," Neurobiology of Disease **46**, 204 (2012).

[187] J.-L. Huret, M. Ahmad, M. Arsaban, A. Bernheim, J. Cigna, F. Desangles, J.-C. Guignard, *et al.*, "Atlas of Genetics and Cytogenetics in Oncology and Haematology in 2013," Nucleic Acids Research **41**, 920 (2013).

[188] Atlas of Gnetics and Cytogenetics in Oncology and Haematology, "FGF2 (fibroblast growth factor 2 (basic))," `http://atlasgeneticsoncology.org/Genes/FGF2ID511ch4q27.html` (May 2010).

[189] S. Schrot, C. Weidenfeller, T. E. Schäffer, H. Robenek, and H.-J. Galla, "Influence of Hydrocortisone on the Mechanical Properties of the Cerebral Endothelium In Vitro," Biophysical Journal **89**, 3904 (2005).

[190] L. B. Thomsen, T. Linemann, K. M. Pondman, J. Lichota, K. S. Kim, R. J. Pieters, *et al.*, "Uptake and Transport of Superparamagnetic Iron Oxide Nanoparticles through Human Brain Capillary Endothelial Cells," ACS Chemical Neuroscience **4**, 1352 (2013).

[191] N. J. Abbott, D. E. M. Dolman, S. R. Yusof, and A. Reichel, *In Vitro Models of CNS Barriers*, 163–197, Springer New York, New York, NY (2014).

[192] A. Grover, A. Hirani, Y. Pathak, and V. Sutariya, "Brain-Targeted Delivery of Docetaxel by Glutathione-Coated Nanoparticles for Brain Cancer," AAPS PharmSciTech **15**, 1562 (2014).

[193] J. M. Tarbell, "Shear stress and the endothelial transport barrier," Cardiovascular Research **87**, 320 (2010).

[194] L. Cucullo, M. Hossain, V. Puvenna, N. Marchi, and D. Janigro, "The role of shear stress in Blood-Brain Barrier endothelial physiology," BMC Neuroscience **12**, 40 (2011).

[195] K. Stanness and D. J. E. Guatteo, "A dynamic model of the blood-brain barrier "in vitro"," Neurotoxicilogy **17**, 481 (1996).

[196] M. E. Katt, Z. S. Xu, S. Gerecht, and P. C. Searson, "Human Brain Microvascular Endothelial Cells Derived from the BC1 iPS Cell Line Exhibit a Blood-Brain Barrier Phenotype," PLoS ONE **11**, e0152105 (2016).

[197] S. D. Kong, J. Lee, S. Ramachandran, B. P. Eliceiri, V. I. Shubayev, R. Lal, and S. Jin, "Magnetic targeting of nanoparticles across the intact blood–brain barrier," Journal of controlled release : official journal of the Controlled Release Society **164**, 49 (2012).

[198] D. Kho, C. MacDonald, R. Johnson, C. P. Unsworth, S. J. O'Carroll, E. du Mez, *et al.*, "Application of xCELLigence RTCA Biosensor Technology for Revealing the Profile and Window of Drug Responsiveness in Real Time," Biosensors **5**, 199 (2015).

[199] J. B. Schlesinger, V. van Harmelen, C. E. Alberti-Huber, and H. Hauner, "Albumin inhibits adipogenesis and stimulates cytokine release from human adipocytes," American Journal of Physiology - Cell Physiology **291**, 27 (2006).

[200] C. Janko, J. Zaloga, M. Pöttler, S. Dürr, D. Eberbeck, R. Tietze, *et al.*, "Strategies to optimize the biocompatibility of iron oxide nanoparticles –"SPIONs safe by design"," Journal of Magnetism and Magnetic Materials **431**, 281 (2017).

[201] M. Hofmann-Amtenbrink, D. W. Grainger, and H. Hofmann, "Nanoparticles in medicine: Current challenges facing inorganic nanoparticle toxicity assessments and standardizations," Nanomedicine: Nanotechnology, Biology and Medicine **11**, 1689 (2015).

[202] M. N. Ragnaill, M. Brown, D. Ye, M. Bramini, S. Callanan, I. Lynch, and K. A. Dawson, "Internal benchmarking of a human blood–brain barrier cell model for screening of nanoparticle uptake and transcytosis," European Journal of Pharmaceutics and Biopharmaceutics **77**, 360 (2011).

[203] A. Salvati, C. Åberg, T. dos Santos, J. Varela, P. Pinto, I. Lynch, and K. A. Dawson, "Experimental and theoretical comparison of intracellular import of polymeric nanoparticles and small molecules: toward models of uptake kinetics," Nanomedicine: Nanotechnology, Biology and Medicine **7**, 818 (2011).

[204] H. R. Kim, S. Gil, K. Andrieux, V. Nicolas, M. Appel, H. Chacun, D. Desmaële, *et al.*, "Low-density lipoprotein receptor-mediated endocytosis of PEGylated nanoparticles in rat brain endothelial cells," Cellular and Molecular Life Sciences **64**, 356 (2007).

[205] O. Harush-Frenkel, E. Rozentur, S. Benita, and Y. Altschuler, "Surface Charge of Nanoparticles Determines Their Endocytic and Transcytotic Pathway in Polarized MDCK Cells," Biomacromolecules **9**, 435 (2008).

---

[206] T. Lin, P. Zhao, Y. Jiang, Y. Tang, H. Jin, Z. Pan, H. He, *et al.*, "Blood–Brain-Barrier-Penetrating Albumin Nanoparticles for Biomimetic Drug Delivery via Albumin-Binding Protein Pathways for Antiglioma Therapy," ACS Nano **10**, 9999 (2016).

[207] J. Gunn, R. K. Paranji, and M. Zhang, "A Simple and Highly Sensitive Method for Magnetic Nanoparticle Quantitation Using ^{1}H-NMR Spectroscopy," Biophysical Journal **97**, 2640.

[208] A. C. Anselmo and S. Mitragotri, "Cell-Mediated Delivery of Nanoparticles: Taking Advantage of Circulatory Cells to Target Nanoparticles," Journal of Controlled Release **0**, 531 (2014).

[209] C. A. Janeway, P. Travers, M. Walport, and M. Shlomchik, *Immunologie*, volume 5th, Spektrum Akademischer Verlag GmbH Heidelberg (2002).

[210] H.-I. Tong, W. Kang, Y. Shi, G. Zhou, and Y. Lu, "Physiological function and inflamed-brain migration of mouse monocyte-derived macrophages following cellular uptake of superparamagnetic iron oxide nanoparticles—Implication of macrophage-based drug delivery into the central nervous system," International Journal of Pharmaceutics **505**, 271 (2016).

[211] O. Lunov, V. Zablotskii, T. Syrovets, C. Röcker, K. Tron, G. U. Nienhaus, and T. Simmet, "Modeling receptor-mediated endocytosis of polymer-functionalized iron oxide nanoparticles by human macrophages," Biomaterials **32**, 547 (2011).

[212] E.-J. Yang, S. Kim, J. S. Kim, and I.-H. Choi, "Inflammasome formation and IL-1β release by human blood monocytes in response to silver nanoparticles," Biomaterials **33**, 6858 (2012).

[213] D. M. Gonçalves, S. Chiasson, and D. Girard, "Activation of human neutrophils by titanium dioxide (TiO2) nanoparticles," Toxicology in Vitro **24**, 1002 (2010).

[214] I. Siglienti, M. Bendszus, C. Kleinschnitz, and G. Stoll, "Cytokine profile of iron-laden macrophages: Implications for cellular magnetic resonance imaging," Journal of Neuroimmunology **173**, 166 (2006).

[215] D. Alizadeh, L. Zhang, J. Hwang, T. Schluep, and B. Badie, "Tumor-Associated Macrophages Are Predominant Carriers of Cyclodextrin-Based Nanoparticles into Gliomas," Nanomedicine : Nanotechnology, Biology, and Medicine **6**, 382 (2010).

[216] D. Chu, J. Gao, and Z. Wang, "Neutrophil-Mediated Delivery of Therapeutic Nanoparticles across Blood Vessel Barrier for Treatment of Inflammation and Infection," ACS nano **9**, 11800 (2015).

[217] C. Baufeld, E. O'Loughlin, N. Calcagno, C. Madore, and O. Butovsky, "Differential contribution of microglia and monocytes in neurodegenerative diseases," Journal of Neural Transmission (2017).

[218] M. K. Spriggs, P. J. Lioubin, J. Slack, S. K. Dower, U. Jonas, D. Cosman, *et al.*, "Induction of an interleukin-1 receptor (IL-1R) on monocytic cells. Evidence that the receptor is not encoded by a T cell-type IL-1R mRNA." Journal of Biological Chemistry **265**, 22499 (1990).

[219] A. T. Argaw, Y. Zhang, B. J. Snyder, M.-L. Zhao, N. Kopp, S. C. Lee, C. S. Raine, *et al.*, "IL-1β Regulates Blood-Brain Barrier Permeability via Reactivation of the Hypoxia-Angiogenesis Program," The Journal of Immunology **177**, 5574 (2006).

[220] Y. Wang, S. Jin, Y. Sonobe, Y. Cheng, H. Horiuchi, B. Parajuli, J. Kawanokuchi, *et al.*, "Interleukin-1β Induces Blood–Brain Barrier Disruption by Downregulating Sonic Hedgehog in Astrocytes," PLoS ONE **9**, 110024 (2014).

[221] S. S. Shaftel, W. S. T. Griffin, and M. K. O'Banion, "The role of interleukin-1 in neuroinflammation and Alzheimer disease: an evolving perspective," Journal of Neuroinflammation **5**, 7 (2008).

[222] Y. Huang, B. Zhang, S. Xie, B. Yang, Q. Xu, and J. Tan, "Superparamagnetic Iron Oxide Nanoparticles Modified with Tween 80 Pass through the Intact Blood–Brain Barrier in Rats under Magnetic Field," ACS Applied Materials & Interfaces **8**, 11336 (2016).

[223] S. N. Tabatabaei, H. Girouard, A.-S. Carret, and S. Martel, "Remote control of the permeability of the blood–brain barrier by magnetic heating of nanoparticles: A proof of concept for brain drug delivery," Journal of Controlled Release **206**, 49 (2015).

[224] M. Raasch, K. Rennert, T. Jahn, C. Gärtner, G. Schönfelder, O. Huber, *et al.*, "An integrative microfluidically supported in vitro model of an endothelial barrier combined with cortical spheroids simulates effects of neuroinflammation in neocortex development," Biomicrofluidics **10**, 044102 (2016).

[225] E. K. Müller, C. Gräfe, F. Wiekhorst, C. Bergemann, A. Weidner, S. Dutz, and J. H. Clement, "Magnetic nanoparticles interact and pass an in vitro co-culture blood-placenta barrier model," Nanomaterials, *submitted* (2017).

[226] A. L. Barnes, R. A. Wassel, F. Mondalek, K. Chen, K. J. Dormer, and R. D. Kopke, "Magnetic characterization of superparamagnetic nanoparticles pulled through model membranes," Biomagnetic Research and Technology **5**, 1 (2007).

[227] M. Z. Pedram, A. Shamloo, A. Alasty, and E. Ghafar-Zadeh, "Optimal Magnetic Field for Crossing Super-Para-Magnetic Nanoparticles through the Brain Blood Barrier: A Computational Approach," Biosensors **6**, 25 (2016).

[228] B. Shapiro, K. Dormer, and I. B. Rutel, "A Two-Magnet System to Push Therapeutic Nanoparticles," AIP Conference Proceedings **1311**, 77 (2010).

Acknowledgment

Zunächst danke ich Prof. Dr. Andreas Hochhaus für die Möglichkeit meine Dissertation in seiner Klinik anfertigen zu dürfen und für seine Übernahme der Gutachterfunktion. Ebenso gilt mein Dank Prof. Dr. Ferdinand von Eggeling für seine Bereitschaft ein weiterer Gutachter zu sein.

Für die wissenschaftliche Betreuung im Laboralltag mit stets motivierenden Worten, einem immer offenen Ohr für jegliche Probleme und das entgegengebrachte Vertrauen möchte ich mich bei Dr. Joachim Clement bedanken.

Ferner danke ich allen Projektpartnern des DFG-Schwerpunktprogramms 1681, insbesondere Prof. Dr. Silvio Dutz, Andreas Weidner, Dr. Robert Müller, Dr. Ioana Slabu, Dr. Frank Wiekhorst und Dr. Ralf Friedrich, für die intensive, stets angenehme und konstruktive Zusammenarbeit, die maßgeblich zum Entstehen dieser Arbeit beigetragen haben.

PD Dr. Julian Großkreuz danke ich für die Bereitstellung von Astrozyten-konditioniertem Medium, sowie Dr. Marcus Stapf für die detaillierte Einführung in die Atomabsorptionsspektroskopie. Für die fundierte Expertise im Hinblick auf Immunzelldifferenzierung danke ich Dr. Christa Kunert ebenso wie auch PD Dr. Dr. Michael Kiehntopf für Routinefärbungen in seinem Labor.

Für die immer angenehme Atmosphäre und die allseitige Unterstützung im Laboralltag schätze ich das gesamte Team des onkologischen Forschungslabors ebenso wie die gesellige kleine Runde beim Mittagessen.

Meinen Freunden und vor allem meiner Familie danke ich für die allseitige Unterstützung in jeder Lebenslage und dafür, dass sie immer an mich glauben und nötigen Rückhalt geben.

Mein ganz besonderer Dank gilt letztlich meinem wunderbaren Ehemann Markus. Er ist der wichtigste Pfeiler in meinem Leben und ohne seine stets positive Art und Weise, seine aufmunternden Worte und seine unendliche Geduld bei Problemen jeglicher Art hätte ich dies wohl nicht geschafft.

Ehrenwörtliche Erklärung

Hiermit erkläre ich, dass mir die Promotionsordnung der Medizinischen Fakultät der Friedrich- Schiller-Universität bekannt ist,

ich die Dissertation selbst angefertigt habe und alle von mir benutzten Hilfsmittel, persönlichen Mitteilungen und Quellen in meiner Arbeit angegeben sind,

mich folgende Personen bei der Auswahl und Auswertung des Materials sowie bei der Herstellung des Manuskripts unterstützt haben: Prof. Dr. Andreas Hochhaus, Dr. Joachim Clement, Dr. Ioana Slabu und Dr. Frank Wiekhorst,

die Hilfe eines Promotionsberaters nicht in Anspruch genommen wurde und dass Dritte weder unmittelbar noch mittelbar geldwerte Leistungen von mir für Arbeiten erhalten haben, die im Zusammenhang mit dem Inhalt der vorgelegten Dissertation stehen,

dass ich die Dissertation noch nicht als Prüfungsarbeit für eine staatliche oder andere wissenschaftliche Prüfung eingereicht habe und

dass ich die gleiche, eine in wesentlichen Teilen ähnliche oder eine andere Abhandlung nicht bei einer anderen Hochschule als Dissertation eingereicht habe.

Jena, den 04.12.2017 Christine Gräfe

Wissenschaftliche Publikationen

[1] C. Gräfe, I. Slabu, F. Wiekhorst, C. Bergemann, F. von Eggeling, A. Hochhaus, L. Trahms and J. H. Clement, "Magnetic particle spectroscopy allows precise quantification of nanoparticles after passage through human brain microvascular endothelial cells," Physics in Medicine & Biology **61**, 3986 (2016).

[2] C. Gräfe, A. Weidner, M. von der Lühe, C. Bergemann, F. H. Schacher, J. H. Clement and S. Dutz; "Intentional formation of a protein corona on nanoparticles: Serum concentration affects protein corona mass, surface charge, and nanoparticle-cell interaction," International Journal of Biochemistry & Cell Biology **75**, 196 (2015).

[3] C. Gräfe*, M. von der Lühe*, A. Weidner*, P. Globig, J. H. Clement, S. Dutz and F. H. Schacher, "Tuning the protein corona with polydehydroalanine based polyelectrolyte coatings," *in preparation* (2017).

[4] E. K. Müller*, C. Gräfe*, F. Wiekhorst, C. Bergemann, A. Weidner, S. Dutz and J. H. Clement, "Magnetic nanoparticles interact and pass an in vitro co-culture blood-placenta barrier model," Nanomaterials, *submitted* (2017).

[5] A. Theumer*, C. Gräfe*, F. Bähring, C. Bergemenn, A. Hochhaus and J. H. Clement, "Superparamagnetic iron oxide nanoparticles exert different cytotoxic effects on cells grown in monolayer cell culture versus as multicellular spheroids," Journal of Magnetism and Magnetic Materials **380**, 27 (2013).

[6] A. Weidner, C. Gräfe, M. von der Lühe, H. Remmer, J. H. Clement, D. Eberbeck, F. Ludwig, R. Müller, F. H. Schacher and S. Dutz, "Preparation of Core-Shell Hybrid Materials by Producing a Protein Corona Around Magnetic Nanoparticles," Nanoscale Research Letters **10**, 992 (2015).

[7] M. Billing, C. Gräfe, A. Saal, P. Biehl, J. H. Clement, S. Dutz, S. Weidner and F. H. Schacher, "Zwitterionic Iron Oxide (γ-Fe2O3) Nanoparticles Based on P(2VP-grad-AA) Copolymers," Macromolecular Rapid Communications **38**, 1600637 (2017).

[8] S. Dutz, S. Wojahn, C. Gräfe, A. Weidner and J. H. Clement,"Influence of sterilization and preservation procedures on the integrity of protein coated magnetic nanoparticles," Nanomaterials, *under revision* (2017).

[9] U. Allenstein, E. Wisozki, C. Gräfe, J. H. Clement, Y. Liu, J. Schroers and S. G. Mayer, "Binary Fe-Pd submicron structures fabricated through glancing angle deposition (GLAD) for bioapplications," Materials & Design **131**, 366 (2017).

[10] M. von der Lühe, U. Günther, A. Weidner, C. Gräfe, J. H. Clement, S. Dutz, F. H. Schacher, " SPION@Polydehydroalanine Hybrid Particles," RSC Advances **5**, 31920 (2015).

[11] M. Zhou, T. Liebert, R. Müller, A. Dellith, C. Gräfe, J. H. Clement and Thomas Heinze, "Magnetic Biocomposites for Remote Melting," Biomacromolecules **16**, 2308 (2015).

[12] M. Fischer, J. P. Müller, B. Spies-Weisshart, C. Gräfe, O. Kurzai, K. Hünniger, A. Hochhaus, S. Scholl and U. Schnetzke, "Isoform localization of Dectin-1 regulates the signaling quality of anti-fungal immunity," European Journal of Immunology **47**, 848 (2017).

[13] I. Antonow-Schlorke, A. Helgert, C. Gey, T. Coksaygan, H. Schubert, P. W. Nathanielsz, O. W. Witte and M. Schwab, "Adverse effects of antenatal glucocorticoids on cerebral myelination in sheep," Obstetrics & Gynecology **113**, 142 (2009).

Jena, den 04.12.2017 Christine Gräfe

---

[*] equally contributed

Wissenschaftliche Vorträge

[1] C. Gräfe, E. Müller, P. Globig, N. Schwarze, M. Liebl, F. Wiekhorst, A. Weidner, S. Dutz, R. Müller, E. Schreiber, R. P. Friedrich, C. Alexiou, A. Hochhaus, and J. H. Clement, "Cell culture-based in vitro barrier models for in- vestigating the dynamics of magnetic field driven passage of superparamagnetic nanoparticles," 5th Colloquium of DFG Priority Program 1681, Benediktbeuern (2017).

[2] C. Gräfe, E. K. Müller, I. Slabu, A. Weidner, F. Wiekhorst, A. Hochhaus, S. Dutz, and J. H. Clement, "Cell culture-based in vitro models for investigating the SPION passage through cellular barriers," 16th Jahrestagung der Biomedizinischen Technik und Dreiländertagung der Medizinischen Physik, Dresden (2017).

[3] C. Gräfe, I. Slabu, A. Weidner, E. Schreiber, R. P. Friedrich, F. Wiekhorst, C. Alexiou, S. Dutz, A. Hochhaus, and J. H. Clement, "The passage of SPIONs through an in vitro blood-brain barrier is dependent on the SPIONs? surface charge," 16th Ferrofluid Workshop, Dresden (2017).

[4] C. Gräfe, E. Müller, N. Schwarze, D. Eberbeck, I. Slabu, F. Wiekhorst, A. Weidner, S. Dutz, A. Hochhaus, F. von Eggeling, and J. H. Clement, "The dynamics of magnetic field driven interaction of superparamagnetic nanoparticles with biological barriers," 4th Colloquium of DFG Priority Program 1681, Benediktbeuern (2016).

[5] C. Gräfe, I. Slabu, R. Müller, A. Hochhaus, F. von Eggeling, F. Wiekhorst, and J. H. Clement, "Passage of SuperParamagnetic Iron Oxide Nanoparticles (SPIONs) trough Cell Layers," 11th International Conference on the Scientific and Clinical Applications of Magnetic Carriers, Vancouver, Kanada (2016).

[6] C. Gräfe, I. Slabu, F. Wiekhorst, R. Müller, A. Hochhaus, F. von Eggeling, L. Trahms, and J. H. Clement, "Passage of SPIONs through Cellular Layers," Crossing Biological Barriers - Advances in Nanocarrier Design for Targeted Drug Delivery Dresden, Germany, (2015).

[7] C. Gräfe, I. Slabu, F. Wiekhorst, A. Weidner, S. Dutz, R. Müller, A. Hochhaus, F. von Eggeling, and J. H. Clement, "SPION Passage through Cellular Barriers," 3^{th} Colloquium of DFG Priority Program 1681, Benediktbeuern (2015).

[8] C. Gräfe, A. Weidner, I. Slabu, F. Wiekhorst, S. Dutz, A. Hochhaus, and J. H. Clement, "Monitoring the Passage of SPIONs trough Cell Layers," Ilmenau Symposium on Medical Application of Magnetic Nanoparticles and Ferrofluids (ISMAP), Ilmenau, Germany (2015).

[9] C. Gräfe, F. Wiekhorst, R. Müller, A. Hochhaus, F. von Eggeling, and J. H. Clement, "Passage of SPIONs through cell layers," 3^{th} Colloquium of DFG Priority Program 1681, Benediktbeuern (2014).

[10] C. Gey, F. Bähring, C. Bergemann, F. Schlenk, D. Fischer, A. Hochhaus, and J. H. Clement, "The Influence of Superparamagnetic Nanoparticles on Cell Viability and Intracellular Signaling," 13^{th} German Ferrofluid Workshop, Benediktbeuern (2013).

Jena, den 04.12.2017 Christine Gräfe